UNIVERSITÀ
DEGLI STUDI
DI PADOVA

Head Office: Università degli Studi di Padova

Department of Management and Engineering

Ph.D. COURSE IN Mechatronics and Product Innovation Engineering
CURRICULUM: Mechanics of Materials
SERIES XXX

DEVELOPMENT OF PROCEDURES AND ANALYTICAL-NUMERICAL MODELS FOR INCREMENTAL FORMING PROCESSES OF METALLIC MATERIALS

Coordinator: Prof. Roberto Caracciolo
Supervisor: Prof. Guido A. Berti

Ph.D. student : Luca Quagliato

Abstract

For more than 150 years, metal forming and forging processes have been the core of the heavy industries manufacturing, both for yearly production as well as for a number of workers, employees, and engineers involved in this sector. Although forgings have been manufactured by smiths for many millennia, only in the last 60 years the importance of understanding the material behavior and its interaction with the process parameters and the manufacturing conditions have started to be deeply investigated by scholars. During the metal forging process, the material may be subjected to small or large deformations which affect both its shape as well as the mechanical properties of the final product. For this reason, in order to pursue the ever-growing trend of enhancing the performances of both products and processes, the research focus should be oriented on understanding the influence of the manufacturing approach, namely in terms of process conditions and parameters, on the characteristic of the final product.

This bottom-to-top approach allows a deeper understanding of the interactions between material and process, opening the way to a more efficient production strategy, not only based on experience but which also relies on mechanical and physical basis.

To this aim, analytical models taking into account the fundamental of both mechanics and heat transfer during the process, conveniently linked to the process parameters, are a powerful and convenient way to analyze the impact of design strategies and parameters choices on important process output during the process, such as geometry evolution, temperature and forces.

The research work presented in this thesis is related to the development of analytical models for the ring rolling, a metal forging process utilized for the manufacturing of small, medium, large and super-large seamless rings, utilized in various applications for, but not only, aerospace, naval and eolic industries. The developed analytical models deal with the following key-tasks in the design phase of the ring rolling process, namely: i) calculation of the feasible ranges for the most important process parameters, ii) estimation of the evolution of the geometry of the ring throughout the process, iii) calculation of the 3D strain tensor in the

ring during the process, vi) lumped steady-state temperature model for estimation of the temperature drop of the ring due convection, conduction and radiation heat transfer during the process, v) calculation of the contact geometry between tools and rings in the two deformation gaps, namely the mandrel-main roll and the axial rolls deformation gap and vi) estimation of the process forces, for both the deformation gaps, by utilizing a slip-line based force model.

The results of the developed models have been compared, where available, with previous literature ones, showing the improvement in terms of accuracy of the results, especially in terms of calculation for ranges in which to choose the process parameters, for the estimation of the geometry evolution of the ring and for the calculation of the process forces.

The results of the developed models have been also compared with laboratory experiments performed on a test ring rolling machine and light alloys, such as the Pb75-Sn25 soft alloy, and with numerical simulations, implemented in the commercial software Simufact.Forming.

The accuracy of the developed models have been calculated, where possible, comparing the results of the analytical estimations with both experimental and numerical results and were not possible, such as in case of the strain tensor estimation, only with the results of the numerical simulations.

The main results of the combined utilization of the developed numerical models are related to the estimation of the evolution of the geometry of the ring throughout the process, which can be estimated, in terms of the outer diameter of the ring, with an accuracy higher or equal to 97%. In addition to that, by utilizing together all the developed models, the flow stress of the material can be analytically estimated based on a chosen flow stress model, leading to an accuracy higher or equal to 93%.

In the present thesis work, the mathematical background, required for the full understanding of the developed algorithm, the full mathematical derivations of the analytical models, the results of both laboratory experiments and numerical simulations as well as, where applicable, the comparison with previous literature models are presented, allowing a full understanding of both the fundamentals and the implementation of the developed approaches.

The proposed collection of algorithm allows a deep understanding of the influence of process parameters, boundary conditions and dimensions on the main influencing manufacturing output, such as geometrical expansion, temperature drop, and forces. In the design phase of the ring rolling process, as well as of all the manufacturing processes, several different combinations of process parameters must be tested in order to determine, among them, the initial preform from which to start the production, the machine to utilize for the production as well as the process parameters to utilize. By means of the developed algorithms, several different combinations of process parameters can be tested in a relatively short amount of time, thanks to the closed-form typology of the equations of the proposed models. Afterward, on the few geometry-process parameters combinations those have shown to lead to a successful manufacturing of the ring, fulfilling the

process constraints, mainly related to the capability of the available ring rolling mill in terms of maximum forming force, numerical simulation can be run, allowing a full understanding of the designed process.

The proposed approach allows sparing precious time during the design stage, allowing to concentrate the attention only of few design options and, for this reason, it may be of interest of both scholars and industrial engineers dealing with the set-up and control of the radial-axial ring rolling process of flat rings.

Acknowledgements

I wish to address my first thoughts to my mother, the person who, more than everyone else, has always supported and counseled me during my whole life. Thanks to her, almost 10 years ago I undertook the journey which led me to this moment, and thanks to her unconditional and constant "mental boosting" I accomplished results and overcame difficulties those I would not have been able to face alone.

Another special thanks goes to my Supervisor, Prof. Guido Berti, the person from whom I learned most during my student life and who, from the very beginning, understood very well that my thirst for living abroad could be exploited as an opportunity for enriching my background, making personal life and working experiences and create new interconnections between universities.

I want to address a special thank also to my current supervisor and my future Post-doc advisor, Prof. Naksoo Kim of the Sogang University. Rarely in my life, I saw so much trust given to an almost unknown person like that he gave to me since I have first contacted him in late 2015. I owe Prof. Kim many of the success in my academic life of the last 12 months and I did, are doing and will do my best to pay back his trust.

I want also to thank my lifelong friend Mattia, who helped me in the creation of the schematic diagrams contained in this thesis. Without him, the quality of the drawing of most of my papers would have been dramatically lower.

Finally, I want to thank all my friends, from all over the world, who I met during these last 4 years of going there and back from Europe to Asia, as an exchange student, to attend conferences and for personal traveling. I tried and I'm still trying to learn a life-lesson from every one of you, keeping an opened mind in every situation, aiming to become not only a good researcher but also a better person.

I want to conclude with a quote from a friend: "Research is far more than sitting in front of a computer to summarize some experiment or simulation results in a text file, it is the intrinsic nature of humans to seek explanation to something they do not know yet, it is the ultimate job experience."

감사의 글

먼저 저의 인생에서 무조건적인 지원과 응원, 그리고 진심 어린 조언들을 아낌없이 주신 어머님께 가장 큰 감사의 마음을 드립니다. 지금의 저를 이 자리에 있게 하는 기나긴 여정에 10 여년 전 첫발을 내딛을 수 있었던 건 다분히 어머니 덕분입니다. 그리고 그 여정에서 어머니의 끊임없는 사랑과 격려는 제가 학문적으로 성취하고 모든 종류의 힘든 일을 극복하는 데 너무나도 큰 힘이 되었습니다. 저 혼자였다면 불가능했을 일들이 어머니가 있었기에 가능했습니다.

저의 학창생활 동안 가장 많은 배움을 주시고, 유학생활에 대한 저의 갈망을 누구보다도 잘 이해해주신 Guido Berti 교수님께 큰 감사의 인사를 전합니다. 교수님께서는 외국에서의 경험들이 저의 학문적인 경력, 실무적인 이력, 그리고 개인적인 삶의 질을 높이고, 대학 간의 새로운 결연을 맺게 하는 아주 좋은 기회라며 언제나 응원해 주셨습니다.

현재 저의 지도교수님이자, 박사 후에도 저의 조언자가 되어 주실 서강대학교의 김낙수 교수님께 진심으로 감사드립니다. 저와 처음 연락이 닿기 시작한 2015 년 말부터 제 삶에서 지금까지 감히 상상하기 힘든, 또 받아보지 못한 무한한 신뢰를 저에게 보여주셨습니다. 지난 12 개월동안 저의 많은 학업적 성취를 가능케 한 교수님께 큰 신세를 지고 있습니다. 교수님으로부터 받은 그 신뢰에 보답하기 위해 노력하고 있고, 또 노력할 것입니다.

나의 평생지기로서, 이 논문 안에 포함된 구성도를 만드는 데 큰 도움을 준 마띠아에게도 감사의 말을 전합니다. 그의 도움으로 논문 내의 구성도의 질이 월등히 높아졌습니다.

마지막으로, 교환학생으로서 지난 4 년간 유럽과 아시아를 오가며 세계 여러 나라의 학회를 참석하거나, 여행을 하는 과정에서 만난 모든 친구들에게 감사의 인사를 전합니다. 그 과정에서 만난 친구들 모두로부터 삶의 중요한 의미들을 배울 수 있었고, 지금도 여전히 배우고 있는 중입니다. 좋은 연구원일 뿐만 아니라 인격적으로 더 풍요로운 사람이 되기 위해, 편견이나 장벽 없이 열린 마음으로 세상을 대해야 한다는 소중한 가름침을 얻을 수 있었습니다.

친구의 말을 인용하면서 감사의 말을 마무리 짓고자 합니다: “연구를 하는 것은 단지 컴퓨터 앞에 앉아서 실험이나 시뮬레이션 결과를 파일로 저장하는 것 이상의 어떤 것이다. 그것은 인류가 아직까지 파악하지 못하는 미지의 세계를 설명하고자 하는 인간의 본원적인 욕구를 실현할 수 있는 위대한 과정인 것이다.”

Ringraziamenti

Come prima cosa, desidero esprimere tutta la mia gratitudine a mia madre, la persona che più di ogni altro mi ha sempre supportato e consigliato durante tutta la mia vita. E' grazie a mia madre se, ormai quasi 10 anni fa, ho intrapreso il percorso che mi ha condotto fino a qui ed è sempre grazie al suo incondizionato e constante supporto morale che sono riuscito a raggiungere risultati e superare difficoltà che non sarei mai riuscito ad affrontare da solo.

Un altro ringraziamento speciale va al mio Supervisore, il Prof. Guido Berti, la persona da cui mi sento di dire di aver imparato di più durante la mia vita da studente e che, fin dal principio, ha capito come la mia voglia di vivere all'estero potesse essere incanalata per creare opportunità di miglioramento per il mio background professionale, fare esperienze sia personali che lavorative e creare nuove relazioni accademiche tra università.

Voglio inoltre ringraziare in modo speciale il mio attuale supervisore e futuro Postdoc advisor, il Prof. Naksoo Kim della Sogang University. Raramente nella mia vita ho visto così tanta fiducia riposta in una persona quasi completamente sconosciuta come quella riposta in me dal Prof. Kim dalla prima volta che lo incontrai nell'inverno del 2015. Devo al Prof. Kim la maggior parte dei miei successi in campo accademico e professionale degli ultimi 12 mesi ho cercato di fare, sto facendo e farò in futuro del mio meglio per ripagare questa fiducia.

Voglio inoltre ringraziare il mio amico di lunghissima data Mattia che mi ha aiutato nella realizzazione dei diagrammi contenuti nella tesi. Senza di lui, la qualità dei disegni nella maggior parte delle mie pubblicazioni sarebbe stata tremendamente più bassa.

Infine, voglio ringraziare tutti i miei amici e tutte le persone che ho incontrato durante questi quasi 4 anni di viaggi tra Europa e Asia, sia durante le mie esperienze come studente, durante le partecipazioni a conferenze o durante viaggi. Ho sempre cercato di imparare qualcosa da ogni situazioni in cui mi sono

trovato e da ogni persona con cui ho interagito, sempre cercando di avere una mente aperta verso nuove possibilità, in modo tale da poter diventare non solo un buon ricercatore ma anche una persona migliore.

Vorrei concludere con una citazione di una frase detta da un amico: “Fare ricerca non è solo stare seduto ad una scrivania per riassumere in file di testo i risultati di qualche esperimento o simulazione. In verità, la ricerca rappresenta l’intrinseca tendenza dell’uomo a trovare spiegazioni che ancora non esistono ed è sicuramente il lavoro più eccitante che esista.”

Contents

Abstract iii

Acknowledgements vi

감사의 글 viii

Ringraziamenti x

Chapter 1: Introduction 1

Chapter 2: Literature survey 9

2.1 Process setting and control 10

2.1.1 Calculation of the ring blank dimensions 10

2.1.2 Main roll rotational speed range calculation 12

2.1.3 Mandrel feeding speed range calculation 12

2.1.4 Upper axial roll feeding speed calculation 16

2.1.5 Additional process controls 18

2.2 Estimation of the geometry of the ring 19

2.3 Ring temperature estimation 19

2.4 Force models 20

2.5 Numerical models for the RARR process 28

Chapter 3: Analytical models for the radial-axial ring rolling process 33

3.1 Calculation of the ring blank 35

3.2 Motion laws calculation algorithms 36

3.3 Geometry evolution of the ring 41

3.4 3D strain tensor estimation and geometry update 45

3.5 Lumped heat transfer model 53

3.5.1 Contact geometry and heat exchange models for the mandrel-main roll gap 54

3.5.2 Contact geometry and heat exchange models for the axial rolls gap 57

3.5.3 Mixed convective-radiant heat exchange model 60

3.5.4 Combined utilization of the heat exchange models 61

3.6 Analytical estimation of strain rate and material flow stress 62

3.7 Generalized slip line-based force model 64

3.7.1 Introduction to the method 64

3.7.2 Slip line method theoretical background 65

3.7.3 Slip line field construction algorithm 67
3.7.4 Calculation of the solution for the slip line field 75
Chapter 4: Numerical analysis implementation 79
4.1 Material model 81
4.2 Ring rolling mill and process boundary conditions 82
4.3 Validation study cases 83
4.4 Mesh sensitivity analysis 86
Chapter 5: Laboratory experiments 89
Chapter 6: Results and discussion 93
6.1 Process setting and ring geometry algorithms performances 93
6.2 3D strain tensor estimation and geometry update results 101
6.3 Temperature estimation model validation and accuracy 105
6.4 Limitations of the previous slip line based force model 110
6.5 Generalized slip line based force model accuracy 112
Chapter 7: Conclusions 117
Reference 121

Chapter 1: Introduction

Radial-axial ring rolling is an advanced manufacturing process that allows manufacturing small, medium, large and super-large rings, utilized in several different heavy industries compartments, such as the wind power, the aerospace, the naval, etc. (Zhou 2011). Products manufactured by means of radial-axial ring rolling process present a smooth surface can be forged to a near-net-shape and, if the process is carried out at high temperature, a favorable microstructure grain size and flow can be achieved (Guo 2011). In the radial-axial ring rolling process, Fig. 1, the initial ring preform is deformed both along the radial direction, due to the action of the mandrel towards the main roll, as well as along the vertical direction, due to the pressure applied by the upper axial roll towards the lower one. The continuous movement of both mandrel and upper axial roll makes the ring to expand in diameter and reducing in height, allowing to reach the final desired shape. An example of the initial ring, at the beginning of the ring rolling process, and the final ring, at the end of it, is shown in Fig. 2a and Fig. 2b, respectively.

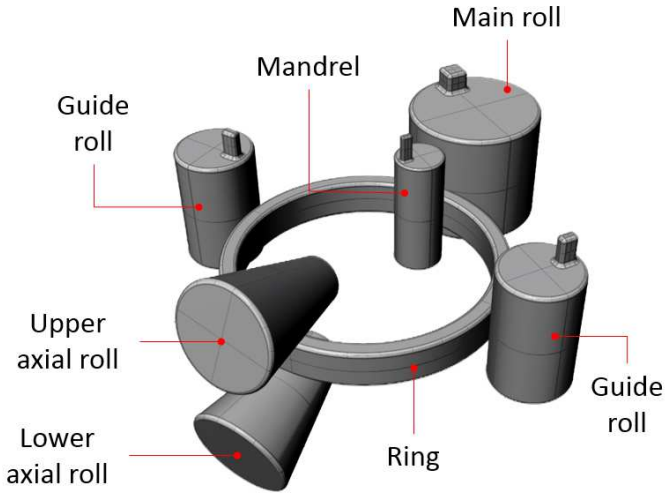

Fig. 1 – The radial-axial ring rolling process.

(a)
Beginning of the process

(a)
End of the process

Fig. 2 – Ring blank at the beginning of the ring rolling process (a) and final ring at the end of it (b).

Source: Kaltek "Full automatic KALTEK ring rolling machine" (Youtube).

In this preliminary section of the thesis, an overview of the research work conducted on the ring rolling process, in terms of analytical models, numerical simulation and experiments are presented. Concerning the developed analytical models, a summary of their purpose, of their relevant input & outputs and of their combined utilization is hereafter presented, leaving the detailed explanation to the relevant sections along in the thesis. To this aim, in Fig. 3, an overlook of all the developed analytical models is shown and the relevant sequence in which the blocks are positioned reflects the real sequence of the calculations.

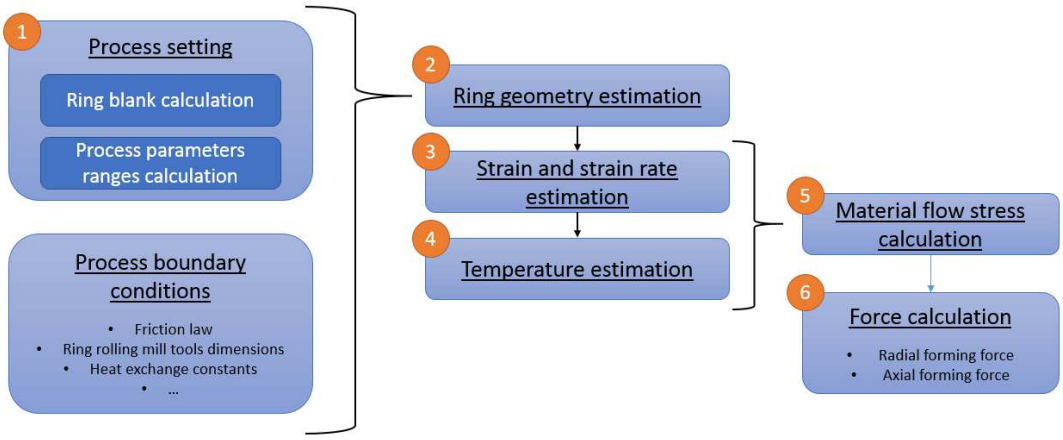

Fig. 3 – Analytical models frame overlook.

In the design stage of the ring rolling process, the focus must be oriented on the determination of the dimensions of the ring blank as well as on the process parameters to utilize to control the tools of the ring rolling mill, namely mandrel, main roll and axial roll. Before starting any calculation concerning the thermo-mechanical behavior of the ring throughout the process, both the ring blank dimensions as well as the ranges in which to choose the above-mentioned process parameters must be defined. These tasks are carried out by the two developed algorithms shown in section 1 of Fig. 3 and their main features are

hereafter presented. Considering the volume conservation principle, a typical characteristic of the plastic deformations, the dimensions of the ring blank are calculated taking into account that the distribution of the material in the cross-section in the ring blank and in the final ring should keep a constant proportion, as pointed out in Keeton (1988).

At the beginning of the calculation, the inner diameter of the ring blank is chosen by the user according to the size of the mandrel, in order to avoid both mechanical interference during the rolling, as well as to avoid too much waste of material during the piercing operation, required to obtain the initial inner hole of the ring blank. The full sequence of the operations/processes related to the ring rolling process is reported in Fig. 4.

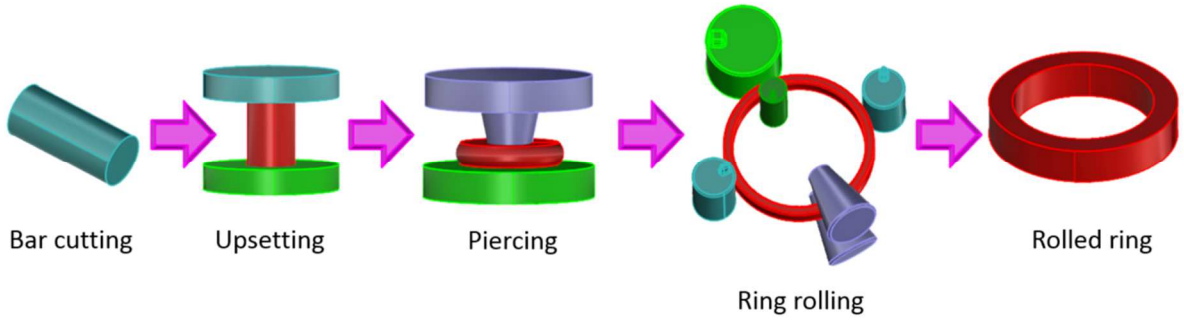

Fig. 4 – Full operations sequence of the ring rolling process.

Accordingly, the algorithm estimates the thickness of the ring blank and the remaining dimensions, namely the outer diameter and height, are immediately calculated. Once the ring blank sizes are determined, the following step in the developed combination of algorithms is the calculation of the ranges in which to choose the motions rules of the tools during the process. This phase is a key step for a successful production, since wrong tool settings may lead to excessive distortion or undesired deformations during the process, resulting in scrap parts or damages for the ring rolling mill. In the process parameters ranges calculation algorithm, all the process and machine boundary conditions are inputted, i.e. the ring rolling mill dimensions in terms of rolls sizes, friction and lubrication conditions, etc. Once the input is fully completed, the algorithm automatically calculates the ranges from which to choose the motion rules for the most important tools, namely the main roll rotational speed, the mandrel feeding speed and the upper axial roll feeding speed. Once the initial and final mandrel feeding speeds are chosen, one for the beginning and one for the end of the process, they are connected by a linear decreasing law and the relevant upper axial roll feeding speeds, an initial and a final one, are accordingly calculated. If all these four velocities are included in the calculated ranges, these set is considered as admissible and allows a uniform and controlled expansion of the ring throughout the process. In order to provide a more clear understanding of the directions of motion

for the above-mentioned tools, Fig. 5 shows an example of possible rotation/translation directions, even though they can be also reversed.

After the initial process setting algorithms section, all the following analytical models concern with the control of the process in terms of important outputs calculation, with the aim of evaluating the impact of the initial process setting choices on the ring, throughout the process.

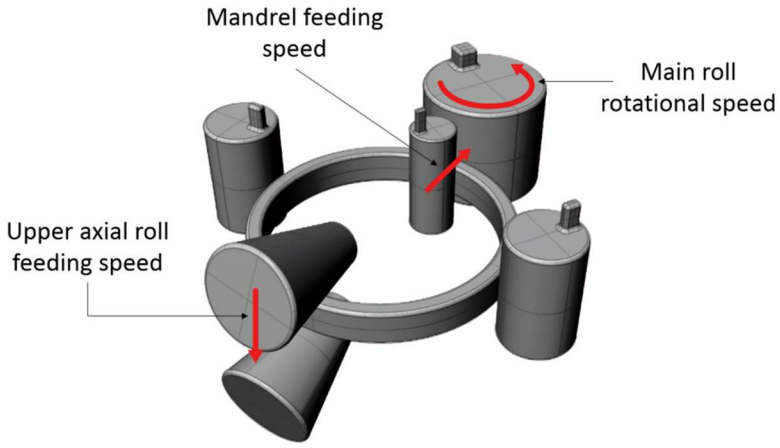

Fig. 5 – Motion directions of the main tools in the ring rolling machine.

As it will be pointed out in detail in the chapter of the thesis relevant to the detailed explanation of the features of the developed analytical models, the base for the calculation, in all the developed algorithms, is represented by the so-called *ring slice*. In order to improve the quality of the calculation, the initial ring blank is virtually subdivided into a certain amount of slices and the geometrical, strain and force data are calculated, during the process, for each slice in which the ring has been initially subdivided. The concept of virtual subdivision into slice is shown in Fig. 6.

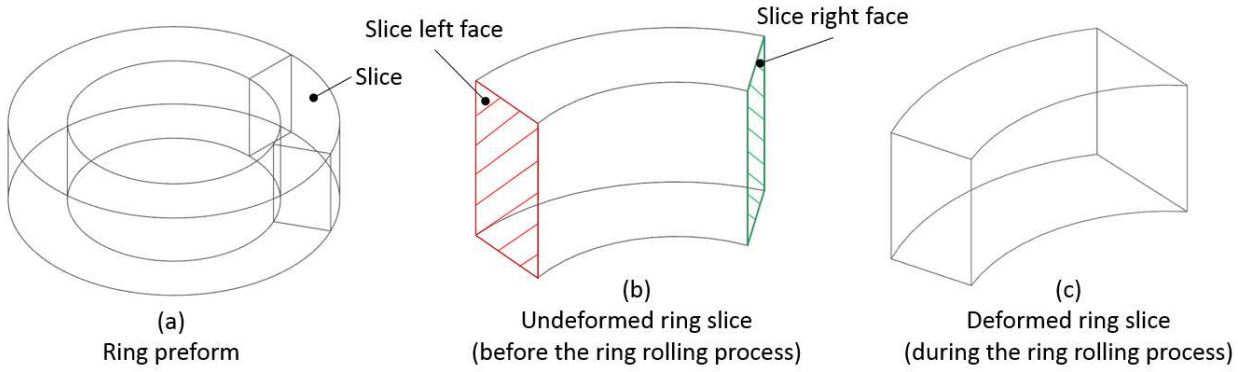

Fig. 6 – Virtual subdivision of the ring into slices.

Concerning the geometry estimation algorithm, section 2 in Fig. 3, its purpose is to calculate the variation of the geometry of each slice of the ring throughout the process as a consequence of the radial

deformation, caused by the mandrel and the main roll in the relevant gap, and by the axial rolls, in the other deformation gap located 180° from the previously-mentioned one. By considering the geometrical evolution of two slides located in opposite locations in the ring, the growth of diameters, height and thickness can be calculated throughout the process. The calculation of the evolution of the geometrical parameters of the ring, for each slice and for each round of the process, is the basis for all the subsequent analytical models, those are all based on the results this first one. The results of the developed algorithm for the estimation of the geometry expansion of the ring throughout the process has been compared with both experimental and numerical results, observing a maximum deviation below 3%, proving the reliability of the developed methodology.

Following the estimation of the geometry of the ring, the subsequent analytical model, section 3 in Fig. 3, deals with the estimation of the 3D strain field in the ring during the process. During the process, the ring is deformed both along the radial and axial directions resulting in a major strain along those directions, as well as along the circumferential direction, this last one responsible for the expansion of the ring diameters.

However, the ring experiences a third deformation in the non-constrained third-direction, namely the vertical direction in the mandrel-main roll deformation gap and the radial direction in the axial rolls deformation gap. For this reason, assuming a state of plane strain in the calculation of the strain tensor results in impreciseness, especially if the strain values are meant to be utilized for the estimation of the flow stress of the material. By considering the first invariant of the tensors, the third strain component is estimated, allowing to complete the principle strain tensor and to define the evolution of the 3D strain field in each slide of the ring throughout the process. Afterwards, based on the strain estimation, the geometry of the ring resulting from the deformation along the third direction is updated, allowing determining the so-called “spread effect”, a undesired phenomenon occurring in the ring rolling process.

The utilization of the strain estimation algorithm allows obtaining two important results: i) the influence of the process parameters on the undesired spread effect can be estimated, allowing to identify the combination of process parameters those allow its reduction; ii) the estimation of the strain is the first step for the analytical estimation of the flow stress of the material and it is required for the estimation of the strain rate. Neglecting the initial non-steady rolling state of the process, the strains along the three principal directions can be estimated with a deviation lower than 10%, in comparison with the relevant numerical simulation. Due to the nature of the strain, no experimental verifications could be carried out for the validation of this specific analytical model.

Concerning the estimation of the temperature drop in the ring due to convective, conductive and radiant heat transfer, a lumped heat transfer model has been developed, section 4 in Fig. 3. Differently from all the other models, the temperature estimation algorithm aims to calculate one common temperature for the ring for each round of the process. The rationale behind the choice of calculating a common temperature for the

whole ring for each round of the process is given by the fact that several different issues can vary the local temperature during the process, especially on the surface of the ring, i.e. due to the presence of scales on its surface. For this reason, the utilization of a more complicated and local temperature estimation analytical solution would probably result in a small enhance the accuracy in comparison to the huge increase in the complexity of the model setting and calculation. The developed lumped temperature estimation model calculates an average temperature for the whole ring in the considered round, averaging the contributions of inner and outer surfaces in the mandrel-main roll deformation gap and of the top and bottom surfaces in the axial roll deformation gap.

In the ring rolling process, the inner surface of the ring is less exposed to the working environment than the outer, which results in a lower temperature drop, in comparison to the outer surface. The same conditions are applicable for the bottom surface of the ring, which is normally in contact with the supporting plane hence less exposed to the working environment. However, at the end of the rolling time, the temperature difference between inner, or bottom, and outer, or bottom, surfaces of the ring is less than 40°C hence considering a common temperature does not result in an unrealistic approximation of the temperature, especially if the process is conducted at high temperature, which means a ring starting temperature of 1200°C (i.e. for steel rings). In addition to that, due to the complexity of carrying out experiments at high temperature, no hot ring rolling experiments could be conducted for the full validation of the temperature estimation model thus the validation has been performed by comparing its estimations with those of numerical simulations. In order to enhance the reliability of the validation, the developed numerical model has been priory validated by comparing its results with literature experiments and the detailed results comparison is presented in the relevant section of the thesis. The comparison between analytical and numerical calculations carried out on 30 different study cases of rings with a final outer diameter ranging from 650mm and 2400mm allowed concluding that the developed algorithm can estimate the average ring temperature with a deviation lower than 5% in comparison to the relevant FEM simulation.

Aiming to analytically estimate the flow stress of the material, for each round of the process, a formulation for the estimation of the strain rate has been developed. Based on the strain components estimated in section 2 Fig. 3, the equivalent plastic strain is estimated after each deformation gap and divided by the contact time between the considered slice and the tools. The contact time is estimated according to the slice length and the rotational speed of the considered tool, either the main roll or the axial rolls. In order to account for the influence of strain, strain rate and temperature on the variation of the material flow stress, the Hansell-Spittel (Hansel 1978, Opela 2015) flow stress formulation has been considered both in the analytical calculations as well as in the relevant numerical simulations.

The analytical estimation of the flow stress of the material of the ring for each round of the process, section 5 in Fig. 3, opens the way to the final stage of the calculation, namely the estimation of the process

forces, namely section 6. To this aim, a slip line based force model has been developed assuming that the plastically deformed section of the ring all deforms according to the same pattern hence by constructing a 2D slip line field. Considering two opposite tools, a condition that is true for both the mandrel-main roll deformation gap as well as for the axial rolls gap, and by considering the middle-cross section of both slice and tools, similar contact pattern can be identified, Fig. 7. In both deformation gaps, a curvilinear contact arc between ring and tools can be identified opening the way to the utilization of a *generalized force model*, either for the calculation of the radial forming force or for the axial one.

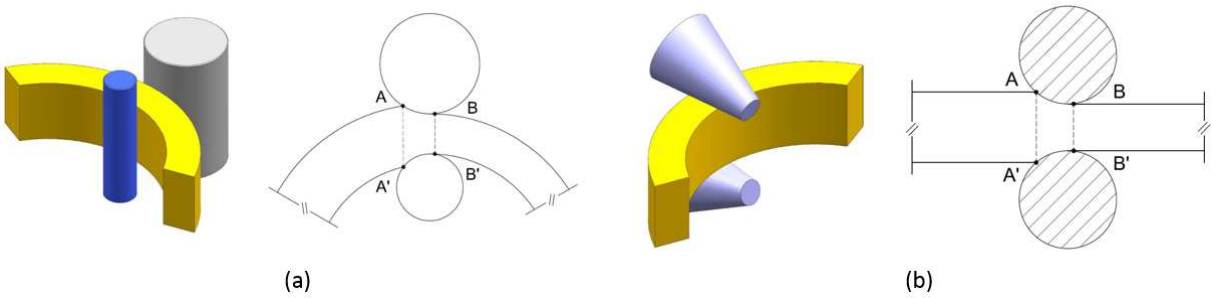

Fig. 7 – Ring deformation pattern in the (a) mandrel-main roll and (b) axial rolls deformation gap.

By seeking the pressure boundary conditions on the extreme points of both contact arcs between ring and tools those make the two slip line fields to join at one point in the cross-section of the considered slice, Fig. 8, the so-called *pressure factor "γ"* can be calculated and utilized for the estimation of the process force.

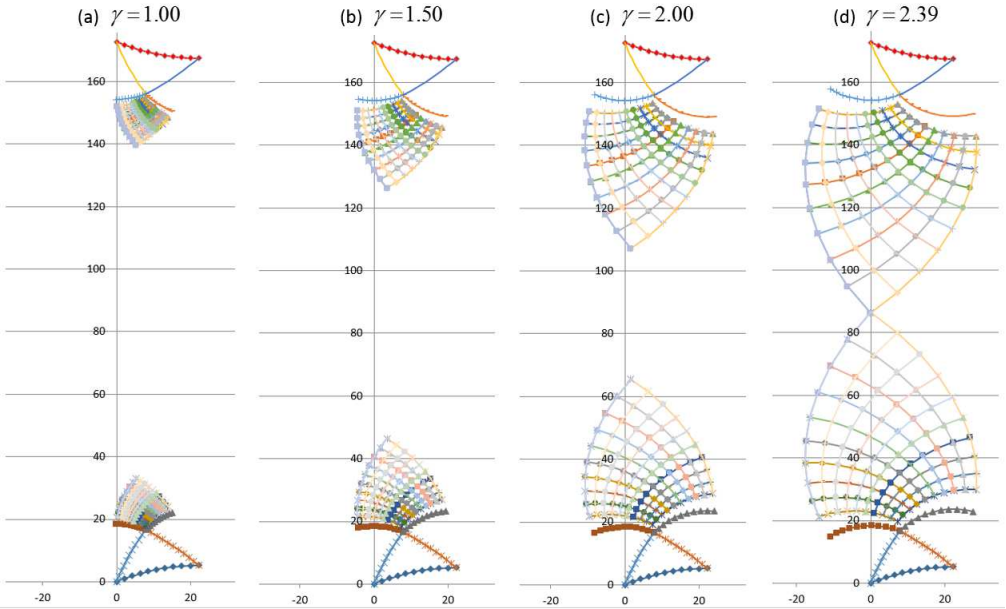

Fig. 8 – Incremental variation of the pressure factor and relevant expansion of the plastic field in the cross-section of the ring.

Since the deformation pattern, the flow stress, and the geometrical data differ in the two deformation gaps, for each round of the process two different pressure factors, one relevant for the mandrel-main roll deformation gap and one for the axial rolls gap, are calculated. Accordingly, for each round of the process, both the radial and the axial forming force are calculated. The detailed explanation of the recursive algorithm for the calculation of the slip line field as well as the iterative calculation of the pressure factor is reported in section 3.7.3 of the thesis.

The estimations carried out by utilizing proposed force estimation algorithm have been compared with both numerical and experimental data on rings made of soft Pb75-Sn25 alloy and under cold forming conditions. The maximum deviation observed, in comparison to the relevant experiment, is calculated in 5.2% for the radial forming force and 8.0% for the axial forming force, allowing validating the developed algorithm. In addition to that, the positive results of the comparisons between experimental and analytical results allows proving the potentiality of the combined utilization of all the developed analytical models in controlling the influence of the process parameters and boundary conditions on the key-output of the process, making the proposed methodology to be of interest to both academy and industry.

The detailed explanation of the developed analytical models is proposed in paragraph 3 of the thesis whereas, in the following paragraph, a literature survey of the models and algorithms available in the literature and relevant for the above-mentioned topics is presented. Where literature models were available, especially concerning the estimation of the ring geometry evolution throughout the process, a comparison with the developed ones is proposed in order to highlight the improvement in the results accuracy obtainable by utilizing the proposed ones.

Chapter 2: Literature survey

Although the radial-axial ring rolling is a widespread and well-known manufacturing process, its set-up and control largely rely on process engineers' and workshop experts' experiences. This fact makes the process design, as well as the initial process test stage, to be high-time consuming and expensive phases.

For this reason, in the literature, several authors focused on various aspects of the ring rolling process, carrying out experiments, developing analytical algorithms and implementing numerical models, both with commercial software or special packages especially developed for the radial-axial ring rolling (RARR) process, in order to pursue a more systematic approach to the ring rolling set-up and control.

Aiming to present a clear summary of the huge research work conducted by investigators concerning the RARR process, the literature survey chapter of the present thesis work is subdivided into sections concerning the available analytical models, relevant for the following main topics:

2.1 Process setting and control
2.2 Estimation of the geometry of the ring
2.3 Ring temperature estimation
2.4 Force models

In addition to that, an additional section, namely section 2.5, covers the part of the literature related to the numerical simulations of the ring rolling process, carried out utilizing either commercial software or special-developed packages. Being the topic of this thesis work related to the development of analytical models, literature contributions, less attention is given to researchers dealing only with numerical simulations of the ring rolling process. In addition to that, since most of the researchers presented results concerning one, or more, of the above-mentioned topics, part of the relevant references will be considered in one or more of the considered sub-sections of the literature survey chapter.

2.1 Process setting and control

Radial-axial ring rolling is a complex metal forging process that involves incremental deformations of a ring preform in order to obtain the final desired ring shape. The initial ring preform is deformed in both its thickness and its height in order to allow the expansion of both inner and outer diameter. To this aim, the size of the initial ring preform, as well as the process parameters for the mandrel, the main roll, and the axial rolls play an import role in the successful manufacturing of the ring.

The focus of this section of the thesis is to present a review of the algorithms available in the literature for the calculation of the size of the ring blank as well as for the calculation of the ranges in which to choose the motion rules of the main tools of the ring rolling machine, namely the mandrel feeding speed, the rotational speed of the main roll and the feeding speed of the upper axial roll. The schematic representation of the movement directions of the above-mentioned tools is shown in Fig. 5.

2.1.1 Calculation of the ring blank dimensions

Concerning the ring blank, the dimensions to be determined are ring inner radius, r_0, ring outer radius, R_0, ring thickness, s_0, and ring height, h_0. As generally accepted, the calculation of the ring blank dimensions is based on an empirical rule defined by Keeton (1988), Eq. (1), which defined the constancy of the difference between the squared height and the squared thickness of the ring or, in other words, that a hyperbolic relationship should be assured between height and thickness. If the relation of Eq. (1) is fulfilled, the ring experiences a uniform expansion thanks to a uniform plastic flow in its section.

$$h^2 - s^2 = const \tag{1}$$

One of the main reference work where the Keeton's (1988) Eq. (1) is not directly utilized for the calculation of the geometrical parameter for the ring blank is Qian et al. (2013) where the volume constancy principle, typical of plastic deformation, is utilized as a reference for the calculation of the ring blank size starting from the dimensions of the final ring. The final dimensions of the ring are defined as: r_F for the ring final inner radius, R_F for the ring final outer radius, s_F for the ring final thickness and h_F for the ring final height. Based on the above-mentioned volume conservation principle, assuming no material volume loss during the process, the relationship between initial and final volume of the ring is defined as in Eq. (2).

$$\pi\left(R_0^{\,2} - r_0^{\,2}\right)h_0 = \pi\left(R_F^{\,2} - r_F^{\,2}\right)h_F \tag{2}$$

By defining the area ratio, between the initial and final cross-section of the ring, Eq. (3), and the ratio between height reduction and thickness reduction, Eq. (4), the equations for the estimation of the height, the outer radius and the inner radius of the ring blank, according to Qian et al. (2013), are defined as in Eq.

(5-7), obtained by substituting (3) and (4) into (2). Accordingly, the thickness of the ring preform can be calculated as $s_0 = R_0 - r_0$.

$$\lambda = \frac{A_0}{A_F} = \frac{h_0 s_0}{h_F s_F} \tag{3}$$

$$\eta = \frac{\Delta h}{\Delta s} = \frac{s_0 - s_F}{h_0 - h_F} \tag{4}$$

$$h_0 = \frac{\left(\eta h_F - s_F\right) + \left[\eta^2 h_F{}^2 + 2\eta h_F s_F \left(2\lambda - 1\right) + h_F{}^2\right]^{1/2}}{2\eta} \tag{5}$$

$$R_0 = \frac{R_F{}^2 - r_F{}^2}{2\lambda s_F} + \frac{\lambda h_F s_F}{2h_0} \tag{6}$$

$$r_0 = \frac{R_F{}^2 - r_F{}^2}{2\lambda s_F} - \frac{\lambda h_F s_F}{2h_0} \tag{7}$$

Even though the algorithm proposed by Qian at al. (2013) does not explicitly take into account the Keeton Eq. (1), the definition of the thickness and height reduction must account for the reduction of process defects, such as the fishtail. The fishtail defect is a forming defect that affects the top and bottom surfaces of the ring and characterized by a higher height of the portion of the ring in contact with the tools, in comparison to the area in the center of the ring, Fig. 9.

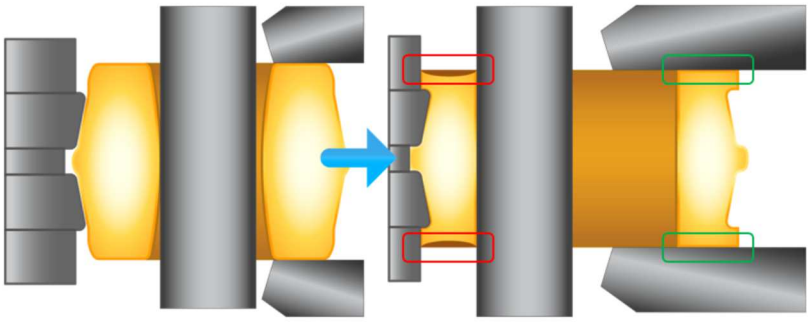

Fig. 9 – Fishtail effect in ring rolling.

By adopting the Keeton's rule, Eq. (1), thanks to a uniform plastic flow in the cross-section of the ring, defects such as the fishtail can be avoided. For this reason, as it will be shown in section 3.1 of the thesis where the developed algorithm for the calculation of the ring blank size will be presented, the explicit inclusion of the Keeton's equation in the calculation of the ring blank preform, allows directly calculating the ring blank size which avoids the arise of forming defects during the ring rolling process.

2.1.2 Main roll rotational speed range calculation

During the ring rolling process, the main roll transfers torque to the ring, allowing it to rotate and to progress in its incremental expansion. Although the choice of the main roll rotational speed is an important parameter for the successful forging of the ring, its calculation is mainly related to dynamic limits of the ring rolling mill and to the dynamic instability which arises in the ring for growing rotational speeds. For this reason, in the literature, practical rules based on experiments have been defined in order to limit the instability of the ring during the process, defining lower and upper ranges for the calculation of the rotational speed of the main roll. The tangential speed of the ring results in the product between the radius of the main roll and the rotational speed of the roll under the hypothesis that no slippage occurs between ring and main roll and therefore the relevant rotational speed of the main roll, as defined by Zhou (2010) and Zhou (2011), should satisfy Eq. (8).

$$\frac{0.4}{R_S} \leq n_S \leq \frac{1.6}{R_S} \tag{8}$$

In Eq. (8), the two numerical coefficients are defined according to literature experiments whereas R_S is the radius of the main roll and n_S the rotational speed of the main roll, expressed in rounds per second.

2.1.3 Mandrel feeding speed range calculation

In order to achieve the circumferential expansion of the ring, its thickness is progressively reduced by the radial movement of the mandrel towards the main roll, Fig. 5. For this reason, the choice of the mandrel feeding speed is most likely to be the most important process parameter affecting the expansion of the ring hence several investigators developed analytical models to properly calculate the ranges in which to determine it, as well its influence on the geometrical expansion of the ring.

The first contribution concerning the determination of the ranges in which to choose the mandrel feeding speed is due to Lin (1997), where the conditions those assure full plastic deformation throughout the whole thickness of the ring and avoid seizing of the ring are derived. As it will be clarified more in detail in chapter 3, the calculation of the ranges in which to choose the process parameters is derived according to the slip line theory, a powerful mathematical approach that allows calculating the preferential direction of plastic flow of the material during a deformation. One of the most relevant contributions concerning the slip line theory applied to plastic deformation processes is due to Hill (1950), where the slip line solutions for the calculation of the material flow in the plastically deformed region of the material, for several manufacturing processes, are presented. In Hua (1997), the solution proposed by Hill (1950) for the case of a flat punch indenting on a flat surface is taken into account thanks to the similarity with the contact zone between ring and tools in the ring rolling process. Considering Hill's solution for a flat indenter acting on a flat surface,

the relevant slip line field, which represents the directions of plastic flow of the material, can be constructed as shown in Fig. 10a (Hill 1950). The AB line represents the contact length between the flat punch and the workpiece whereas the point F is the end of the plastic field in the thickness of the workpiece, respectively.

According to Hill's slip line solution, the pressure in the plastically deformed region of the material can be calculated depending on the ratio between the contact arc length *2a* and the thickness of the slab *s* resulting in the solution chart shown in Fig. 10b. The pressure necessary to initiate the indentation starts from *2k*, yield shear stress of the material in plane strain conditions, and it reaches its maximum of *2.56·2k*, a value of pressure over which the material is spread aside the indenting area and the plastic deformation does not spread throughout the thickness anymore but it is localized only on the surface of the material.

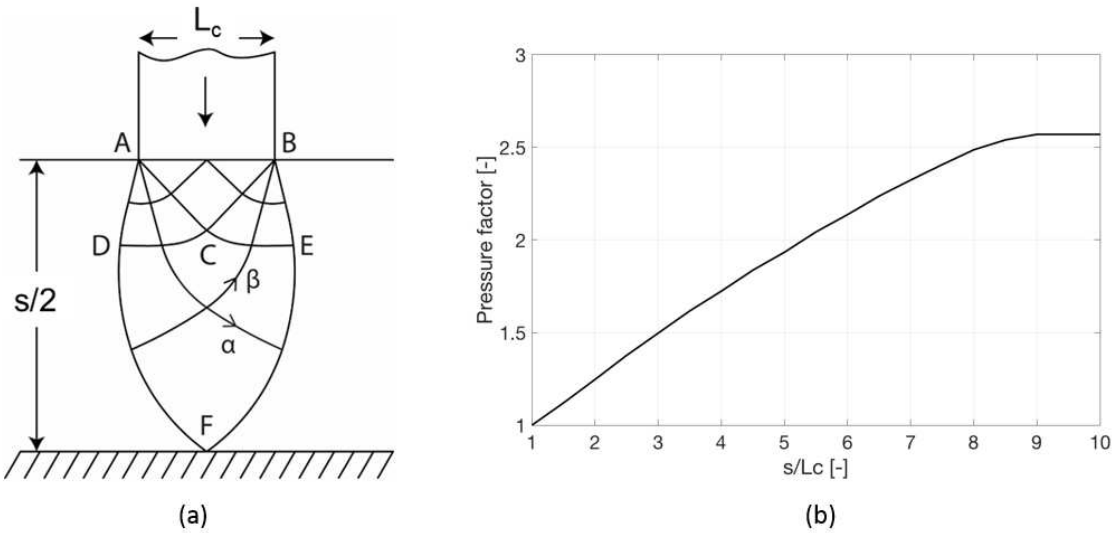

Fig. 10 – (a) Slip line field of a flat indenter acting on a flat surface and (b) relationship between the pressure to start the indentation and s/L ratio (Hill 1950).

Namely, for *s/h* ratios over 8.74, the punch pressure results on a local plastic deformation of only the surface of the material and no plastic deformation can be achieved throughout the thickness of the workpiece. By utilizing the general theory of the slip line applied to plastic deformation, as defined by Hill (1950), in Hua (1997), the minimum and maximum drafts allowed for a specific combination of mandrel radius, main roll radius, ring inner diameter and ring outer diameter can be calculated according to the following procedure, neglecting the curvature of both ring and tools. By considering the schematic representation of the contact between ring and tools in the mandrel-main roll deformation gap as shown in Fig. 11, the average thickness of the ring is defined as $s_m=(s_0+s_F)/2$ and, according to the above-mentioned boundary *s/h* ratio, the correlation with the projection of the contact arc *L* is defined in Eq. (9).

$$\frac{L}{s_m}=\frac{1}{8.74} \tag{9}$$

The projection of the contact arc is defined, by Hua (1997), according to Eq. (10) where Δs represents the thickness draft, R the outer radius and r the inner radius of the ring.

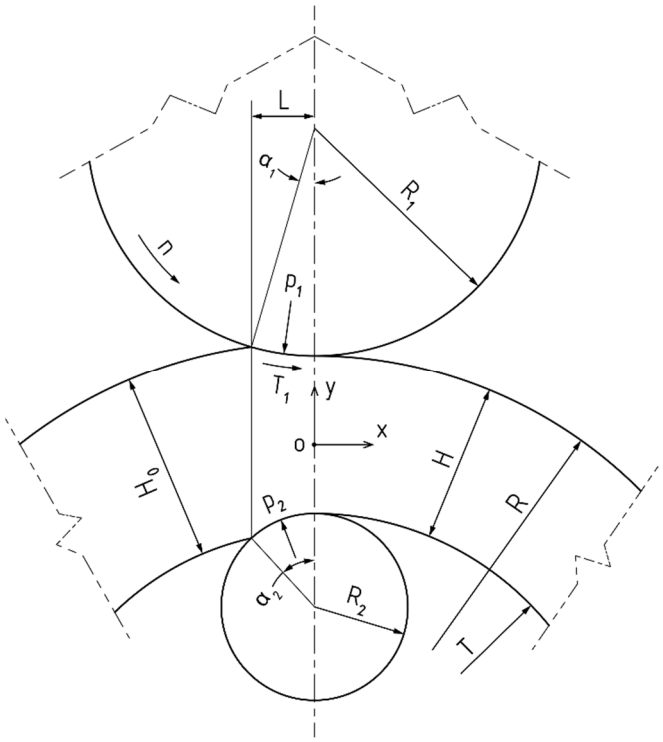

Fig. 11 – Ring-tools and tools in the mandrel-main roll deformation gap (Hua 1997).

$$L = \sqrt{\frac{2\Delta s}{\frac{1}{R_S} + \frac{1}{R_M} + \frac{1}{R} - \frac{1}{r}}} \tag{10}$$

Substituting Eq. (10) into Eq. (9) and considering that $s_m = (s_0 + s_F)/2 = R - r$ it results in Eq. (11), which defines the minimum thickness draft that is necessary in order to assure plastic deformation throughout the whole thickness of the ring and is defined as *penetration condition*.

$$\Delta s_{\min} = 6.55 \cdot 10^{-3} R_S \left(\frac{R}{R_S} - \frac{r}{R_M} \right)^2 \left(1 + \frac{R_S}{R_M} + \frac{R_S}{R} - \frac{R_S}{r} \right) \tag{11}$$

On the other hand, in order to define the maximum allowable thickness draft, over which the ring stuck into the deformation gap due to too high friction forces, the force equilibrium in the deformation gap is considered. In order to achieve continuous rotation and thickness reduction, the ring must be drawn into the deformation gap hence the drawing force must be greater than the backward pushing force, along the x-direction, Fig. 11, resulting in Eq. (12). At the same time, the force equilibrium along the y-direction must be satisfied as well, resulting in Eq. (13). The two angles, α_S and α_M are the contact angles between the ring and main roll and between ring and mandrel, respectively.

$$\sum F_x = T_{Sx} + P_{Sx} + P_{Mx} = T_S \cos\frac{\alpha_S}{2} - P_S \sin\frac{\alpha_S}{2} - P_M \sin\frac{\alpha_M}{2} \geq 0 \quad (12)$$

$$\sum F_y = T_{Sy} + P_{Sy} + P_{My} = -T_S \sin\frac{\alpha_S}{2} - P_S \cos\frac{\alpha_S}{2} - P_M \cos\frac{\alpha_M}{2} = 0 \quad (13)$$

Considering the friction according to the Coulomb's law, hence $T_S = \mu P_M$, the correlation between the friction angle and the two contact angles between ring and tools is defined as $\beta \geq (\alpha_M + \alpha_S)/2$ and represents the *biting-in condition*. Assuming that the projection of the contact arc between ring and tools is small in comparison to either the inner or the outer radius of the ring, the two contact angles can be approximated as in following Eq. (14).

$$\alpha_S = L/R_S \quad ; \quad \alpha_M = L/R_M \quad (14)$$

Considering together Eq. (14) and the definition of the friction angle β the maximum thickness draft equation is defined as (15).

$$\Delta s_{\max} = \frac{2\beta^2 R_S}{\left(1 + \frac{R_S}{R_M}\right)^2}\left(1 + \frac{R_S}{R_M} + \frac{R_S}{R} - \frac{R_S}{r}\right) \quad (15)$$

The set of Eq. (11) and (15) defines the minimum and maximum thickness drafts which can be applied to the ring in order to accomplish plastic deformation throughout the whole thickness while avoiding seizing of the ring between the tools. According to these ranges, Hua (1997) also defined the relevant minimum and maximum ranges for the mandrel feeding speed, as follows.

Assuming a constant mandrel feeding speed, it can be defined according to the thickness draft Δs as $v_M = \Delta s / \Delta t$ where Δt is the time for one round of the ring. Neglecting eventual slippage between rolls and ring, this time can be estimated as the external length of the external circumference of the ring divided by peripheral speed of the ring (which is equal to the peripheral speed of the main roll, under perfect friction wheels hypothesis), allowing to write (16), where the thickness draft is linked to the feeding speed of the mandrel v_M, to the rotational speed of the main roll n, to the outer radius of the ring R and to the radius of the main roll R_S.

$$\Delta s = \frac{v_M}{n}\frac{R}{R_S} \quad (16)$$

By substituting Eqs. (11) and (15) into Eq. (16), minimum and maximum mandrel feeding speed are calculated, as shown in Eqs. (17) and (18), respectively.

$$v_{M,\min} = 6.55 \cdot 10^{-3} n \frac{R_S^{\,2}}{R} \left(\frac{R}{R_S} - \frac{r}{R_M} \right)^2 \left(1 + \frac{R_S}{R_M} + \frac{R_S}{R} - \frac{R_S}{r} \right) \tag{17}$$

$$v_{M,\max} = \frac{2\beta^2 n R_S^{\,2}}{\left(1 + \frac{R_S}{R_M} \right)^2} \left(1 + \frac{R_S}{R_M} + \frac{R_S}{R} - \frac{R_S}{r} \right) \tag{18}$$

According to the formulations defined in Hua (1997), the range in which to choose the mandrel feeding speed is univocally defined by a minimum and a maximum value and, once the velocity is chosen inside this range it is kept constant throughout the whole rolling time. However, as it will be shown in chapter 6, the model proposed by Hua (1997), utilized also by Zhou (2011), Gou (2011), Wang (2010) and Yan (2007), is too conservative and fail to converge to a solution if some specific combinations of ring and tools geometries arise. However, by adopting a different strategy for the set-up of the mandrel feeding speed, namely by setting different ranges for the calculation of the mandrel feeding speed at the beginning and at the end of the process, as proposed in the developed model, this limitation can be overcome.

2.1.4 Upper axial roll feeding speed calculation

Concerning the downward feeding speed of the upper axial roll, Fig. 5, two different main approaches are utilized in the literature. As previously stated, Eq. (1) is normally utilized in order to assure a uniform expansion of the ring throughout the process and, for this reason, once the feeding-per-revolution on the mandrel side is chosen, in terms of range or ranges, it automatically allows to calculate the ranges for the upper axial roll feeding speed. By utilizing this approach, mandrel feeding speed and upper axial roll feeding speed are linked together, the second one depending on the first one.

If this first approach is taken into account, as proposed in the work of Zhou (2010), the amount of thickness and height draft per round of the process can be linked together with the relevant feeding speeds, resulting in Eq. (19) where v_A is the feeding speed of the upper axial roll.

$$\frac{s_0 - s}{v_M} = \frac{h_0 - h}{v_A} \tag{19}$$

The calculation of the axial roll feeding speed according to this rationale has the advantage of assuring a constant expansion of the ring throughout the process since the plastic flow is uniform in the cross section thanks to the fulfillment of Eq. (1), but also presents a limitation, as hereafter explained. In principle, thickness and height of the ring differ themselves and, normally the height of the ring preform is greater than its initial thickness. For this reason, the initial calculation of the maximum and minimum thickness drafts, as operated by previous Eq. (11) and (15), might be partially inconsistent for the height draft, due to the geometrical differences that may arise in a generic ring. Due to this inconsistency, caused by the

different dimensions of thickness and height of the ring, the plastic deformation along the height of the ring might not reach the ring center, limiting its expansion. However, in the radial-axial ring rolling process, most of the ring expansion is achieved by thickness reduction thus, the influence of the height reduction is normally negligible, in comparison to the other one.

Differently from the approach of linking together radial and axial feeding speeds of the mandrel and the upper axial roll, a second approach consists in calculating the feeding speed of the axial roll by applying the same rationale and procedure utilized for the calculation of that of the mandrel. By following this approach, the upper axial roll feeding speed is calculated in order to achieve full plastic deformation throughout the height of the ring and, in this way, guarantees the circumferential expansion of the ring. This approach has been utilized by Zhou (2011) and, since the derivations are same as those presented in the previous paragraph concerning the mandrel feeding speed, are not repeated and only the final equations are hereafter reported.

$$v_{A,\min} = \frac{n_S R_S \left[\Delta h_{\min}\right]_{\max}}{2\pi R} \tag{20}$$

$$v_{A,\max} = \frac{n_S R_S \left[\Delta h_{\max}\right]_{\min}}{2\pi R} \tag{21}$$

In Eqs. (20) and (21), the values of $\left[\Delta h_{\min}\right]_{\max}$ and $\left[\Delta h_{\max}\right]_{\min}$ are defined as in following Eqs. (22) and (23) and represents the maximum among the minimum thickness drafts along the process and the minimum among the maximum thickness drafts along the process, respectively, and are defined as in Eqs. (22) and (23). In Eqs. (22) and (23), S_0 represents the initial distance between the ring and the vertex of the axial roll, measures on its inner radius.

$$\left[\Delta h_{\min}\right]_{\max} = \frac{0.0131 \cdot h_0^{\,2}}{S_0 \tan\left(r/2\right)} \tag{22}$$

$$\left[\Delta h_{\max}\right]_{\min} = 4\beta_A^{\,2} S_0 \tan\left(r/2\right) \tag{23}$$

This approach, by means of considering the narrower of the possible ranges, from the maximum of the minimum velocities to the minimum of the maximum ones, will be proved to have limitations if some specific configurations of the ring are considered. In those cases, there will be no chance of calculating an axial roll feeding speed which falls within the prescribed ranges.

To overcome this limitation, an improvement of the literature models for the calculation of the axial feeding speed has been proposed its full derivations and boundary conditions are presented in the following chapter of the thesis.

2.1.5 Additional process controls

In addition to the three main process controls presented in the previous three paragraphs of the thesis, additional information concerning the backward movement of the axial rolls, on the rotational speed of the axial rolls and on the influence of the centering rolls on the ring rolling process should be given.

Concerning the backward movement of the axial rolls, it must be set in order to follow the expansion of the ring and it is calculated according to the growth rate of the inner, or outer, radius of the ring. In Zhou (2011) the growing speed of outer radius has been defined as following Eq. (24).

$$R(t) = \frac{s_0 h_0 (R_0 + r_0)}{2(h_0 - v_A t_1)(s_0 - v_R t_1)} + \frac{s_0 - v_R \cdot t_1}{2} \tag{24}$$

By derivation of Eq. (23) with respect to the time t, the growing speed of the outer diameter is estimated and the backward moving speed of both axial rolls is meant to be set equal to this value. Although this approach neglects the eventual slippage which may occur between ring and tools, its utilization offers a first reasonable indication for the set-up of the backward motion of the axial rolls.

As pointed out in the work of Zhou (2012), the backward movement of the axial rolls can set-up in two additional ways, additionally to that of following the expansion of the diameters of the ring. One is to avoid any backward movement of the axial rolls and let the ring to slide on their surfaces; this approach is normally utilized for small rings and can lead to instabilities, due to the rise of relative velocities between the ring and the axial rolls. The last one is to keep the virtual vertex of the axial rolls always in the center of the ring throughout the whole expansion; this approach does not have the limitation of the previous one but requires a precise control of the expansion of the ring during the process, which is normally hard to achieve.

Following a similar rationale, also the rotational speed of the axial rolls can be set by taking into account the peripheral speed of the ring, which increases with the growth of the diameters of the ring. In the work of Zhou (2011), neglecting slippage between ring and tools, the rotational speed of the axial rolls is defined as in Eq. (25) where n_S is the rotational speed of the main roll.

$$n_A = \frac{n_S R_M}{S_0 \sin(r/2)} \tag{25}$$

Finally, concerning the centering rolls, Fig. 5, their main role is to stabilize the ring during the process, avoiding accessing movement towards one side or the other. Although in most of the ring rolling processes the centering rolls are directly controlled by the ring rolling mill operator in case of unexpected deviations of the ring movements, their set-up can be analytically taken into account by means of the force they may be required to apply to the ring in order to stabilize it.

2.2 Estimation of the geometry of the ring

Concerning the controls of the ring rolling process, in terms of interpretation and understanding of the effect of the choice of the process parameters on the ring during the process, one of the key aspects is related to the geometrical evolution of the ring throughout the process.

The main literature contribution concerning this topic is due to Zhou (2011), where the equations for the analytical estimation of the geometrical expansion of inner radius, outer radius, and thickness of the ring are derived according to the mandrel and the upper axial roll feeding speed, for increasing time intervals. The three equations relevant for the estimation of radii and thickness are reported in Eqs. (26-28).

$$R(t) = \frac{s_0 h_0 (R_0 + r_0)}{2(h_0 - v_A t_1)(s_0 - v_R t_1)} + \frac{s_0 - v_R \cdot t_1}{2} \tag{26}$$

$$s(t) = \frac{2\pi R(t) v_M}{n_S R_S} \tag{27}$$

$$r(t) = \frac{s_0 h_0 (R_0 + r_0)}{2(h_0 - v_A t_1)(s_0 - v_R t_1)} + \frac{s_0 - v_R \cdot t_1}{2} \tag{28}$$

All the three parameters, $R(t)$, $s(t)$ and $r(t)$ are named as time-dependent ones but, in fact, the calculation is operated considering one average value for the ring radii and thickness for the considered round of the process, assuming the ring to keep an average annular shape. This strong assumption completely ignores the incremental nature of the ring rolling process where different sections of the ring are subjected to different thickness reduction during the process, according to their position in the ring.

As it will be shown in results comparison chapter of the thesis, the application of this model for the calculation of the evolution of the ring geometry throughout the process leads to inaccuracies and cannot account for the final phase of the process, namely the calibration one. However, the developed model for the estimation of the ring geometry, which will be presented in the following chapter of the thesis, can overcome these issues, as it will be proved in the results chapter of the thesis.

2.3 Ring temperature estimation

Concerning the analytical estimation of the ring temperature evolution during the process, no specific literature contributions seem to be available since most of the work focuses on its numerical estimation. It must be noticed that the only clear contribution on how the temperature drops of the ring, throughout the process, as a consequence of conductive, convective and radiant heat exchange is due to Al-Mohaileb, who collected the relevant heat transfer equations, afterward utilized in the numerical model. Since no literature

models were present in the literature, no comparison with previous models is carried out in the results section of the thesis.

2.4 Force models

Being the process forces one of the most relevant topics concerning the ring rolling process, especially from the industry point of view, several researchers focused their attention on studying its variation according to the variation of both ring geometry and process parameters. Although several force contributions can be identified in the ring rolling process, the two those have shown to be the most relevant one are the radial forming force, caused by the push of the mandrel towards the main roll, and the axial forming force, consequence of the downward movement of the upper axial roll towards to lower one. Due to the fact that normally the ring is mostly deformed on its thickness, the radial forming force estimation has always attracted more attention by the researchers. For this reason, the majority of the models available in the literature deal with the estimation of the radial forming force and only a few contributions are available in terms of models for the calculation of the axial forming force.

Concerning the typologies of the models utilized for the force prediction in the ring rolling mill, authors initially utilized a simplified slip line theory, considering the projection of the contact arc between ring and tools and not its actual curvilinear profile. By doing so, Hawkyard (1973) and Mamalis (1976) proposed radial force models for the estimation of the pressure applied by the mandrel to the ring, during the process, based on the amount of thickness draft and on the projection of the contact arc between ring and tools. The theoretical background is based on the slip line solution proposed by Hill (1950) for a case of a flat indenter acting on a workpiece with a flat surface and is hereafter summarized.

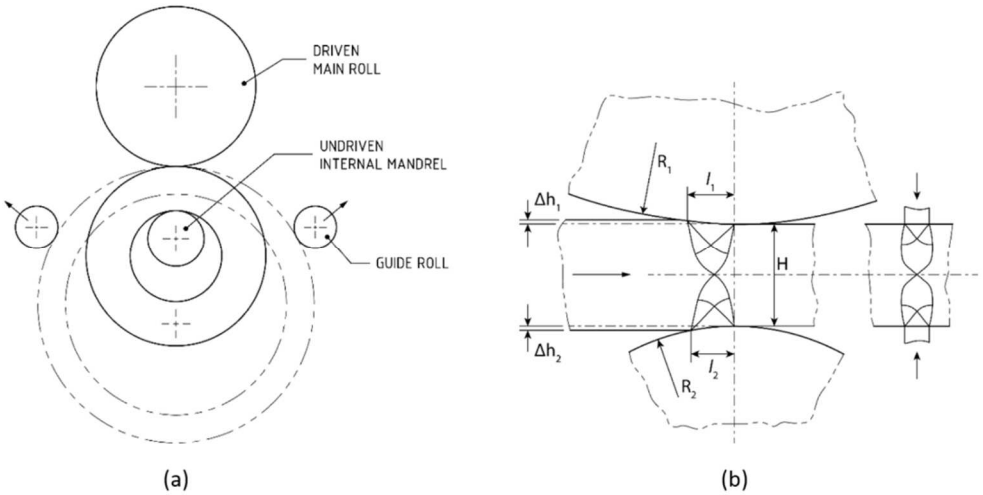

Fig. 12 – (a) Ring rolling process configuration with initial and final ring and (b) detail of the mandrel-main roll deformation gap, with the contact conditions between ring and tools; Hawkyard (1973).

Considering the generic ring rolling process, Fig. 12a, and focusing the attention on the mandrel-main roll deformation gap, Fig. 12b, thanks to the huge curvature of both ring and tools, according to Hawkyard (1973), the contact geometry can be approximated by a straight line, whose length is calculated according to Eq. (29), where Δs is the amount of thickness draft in the considered instant of the process.

$$L_C = \sqrt{\Delta s^2 \left(\frac{2R_S R_M}{R_S + R_M} \right)} \tag{29}$$

Eq. (29) also introduces the approximation that the contact geometry is common for both rolls, either is calculated on the mandrel side or on the main roll side, even though these two rolls have, in principle, different diameters.

As pointed out in previous section 2.1.1, the slip line theory is a powerful methodology which allows calculating the stress state in the plastically deformed region of the material and can be utilized to determine the so-called pressure factor, one of the parameters required for the estimation of the radial forming force in the Hawkyard (1976) force model. Since it is not the purpose of this section to provide a detailed explanation of the mathematical background of the slip line theory and of the procedure by which the slip line field is built, only the key concept concerning the considered force model shall be given. The mathematical background, the procedure for the calculation of the boundary conditions and the algorithm for the construction of the slip line field will be provided in the force model section of the following chapter of the thesis, where the developed slip line-based force model will be presented.

By considering the original Hill's solution for flat indenters, previously shown in Fig. 10a, the pressure factor, names as γ, can be calculated based on the ratio between the thickness of the ring after the deformation and the projection of the contact arc between ring and tools, calculated according to Eq. (29).

One of the main characteristics of the force models based on the slip line theory is given by the fact that they consider a perfectly plastic material model, ignoring any hardening during the deformation and, for this reason, the proper estimation of the material flow stress, according to strain, strain rate, and temperature, is of critical importance.

In conclusion, the force model proposed by Hawkyard (1973), also utilized in Mamalis (1976) is reported in following Eq. (30), where the subscript "i" highlights the fact that the forming force can be computed for each instant of the process if the relevant geometrical and material parameters are known. In addition to that, $s_{F,i}$ stands for the thickness of the ring at the exit of the deformation gap in the considered instant of the process.

$$F_{rad} = 2k_i \gamma_i s_{F,i} L_{C,i} \tag{30}$$

As it will be proved in the result chapter 6, the assumptions of the model in terms of considering the contact geometry between ring and tools as a straight line is not always fulfilled and this fact may lead to

an underestimation of the radial forming force. To reduce this issue, a new slip line based force model, which accounts for the curvilinear contact geometry between ring and tools, has been developed and will be presented in detail in the following chapter of the thesis.

More recently, Parvizi (2010) and Parvizi (2014) proposed two different approached for the estimation of the radial forming force in the ring rolling process. In the first work, a SLAB-based model is derived considering the force equilibrium in the deformation gap under a constant shear friction. The contact between ring and tools is subdivided into two and the relevant pressure contributions are calculates. This is necessary due to the fact that the friction force direction acts towards the exit of the deformation gap until the neutral point and against this direction after it, Fig. 13. Moreover, the position of the neutral point is not known apriori thus the contact arc between ring and tools must be subdivided into two zones, whose lengths are to be calculated as a solution to the equations system.

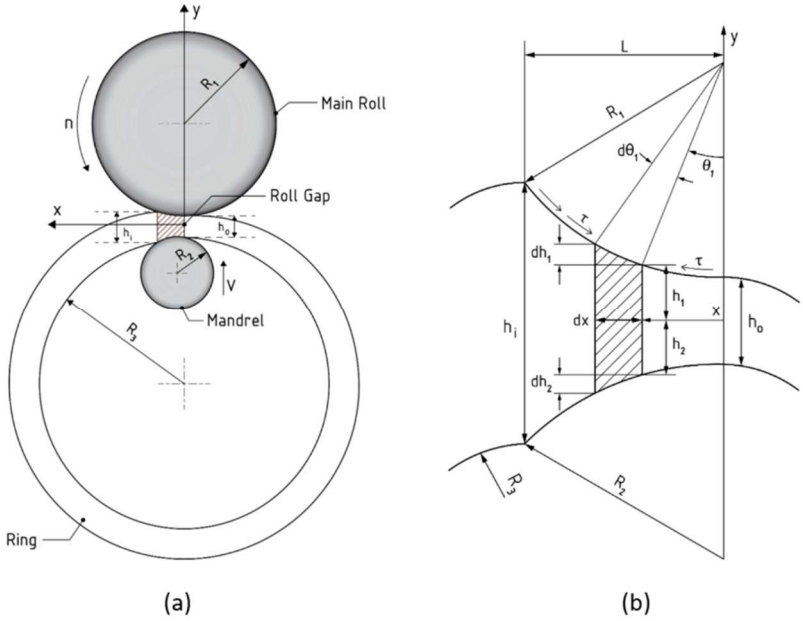

Fig. 13 – (a) Contact between ring and tools in the mandrel deformation gap and (b) detail of forces acting on a generic section of the portion of the ring undergoing the deformation; Parvizi (2011).

Accordingly, the total roll pressure can be defined as the summation of the above-mentioned two effects, as shown in Eq. (31) where x_n is the position of the neutral point along the x-direction, m is the constant friction factor and k the yield shear stress of the material, considered as a constant.

$$F_{rad} = \int_0^{x_n} \left(P_{1,I} - mk\frac{x}{R_S} \right) dx + \int_{x_n}^{L} \left(P_{1,II} + mk\frac{x}{R_S} \right) dx \tag{31}$$

Neglecting the intermediate passages of the integration, the resulting force model equation is reported in Eq. (32) whereas the equation parameters are summarized in Eqs. (33-37).

$$F_{rad} = \left(A_1 - \frac{mk}{R_S} \right) \left(x_n{}^2 - \frac{L_C}{2} \right) + A_2 \left[L_C \left(\ln \left(\frac{L_C}{R_{eq}} + s_0 \right) - 2 \right) \right] + 2\sqrt{s_0 R_{eq}} \arctan \left(\frac{L_C}{\sqrt{s_0 R_{eq}}} \right) +$$
$$+ A_3 \left[\frac{1}{2} \sqrt{s_0 R_{eq}} \ln \left(1 + \frac{L_C{}^2}{s_0 R_{eq}} \right) - L_C \arctan \left(\frac{L_C}{\sqrt{s_0 R_{eq}}} \right) + 2x_n \arctan \left(\frac{x_n}{\sqrt{s_0 R_{eq}}} \right) - \sqrt{s_0 R_{eq}} \ln \left(\frac{x_n{}^2}{s_0 R_{eq}} \right) \right] + \quad (32)$$
$$+ C_{1,I} x_n + C_{1,II} \left(L_C - x_n \right)$$

$$C_{1,I} = k \left(1 + \sqrt{1 - m^2} \right) \left(1 - \ln \left(s_0 \right) \right) \quad \text{for} \quad 0 \le x \le x_n \quad (33)$$

$$C_{1,II} = A_1 L_C + A_2 \left[1 - \ln \left(\frac{L_C{}^2}{R_{eq}} + s_0 \right) \right] + A_3 \arctan \left(\frac{L_C}{\sqrt{s_0 R_{eq}}} \right) - \frac{1}{2} mk L_C \left(\frac{1}{R_S} + \frac{1}{R_{eq}} \right) \quad (34)$$

for $x_n \le x \le L_C$

$$A_1 = \pm mk \left(\frac{1}{R_S} + \frac{1}{R_{eq}} \right) \left(\frac{3}{2} - \frac{R_{eq}}{R_M} \right) \quad (35)$$

$$A_2 = k \left(1 + \sqrt{1 - m^2} \right) \quad (36)$$

$$A_3 = \pm mk \left[\left(\frac{1}{R_S} + \frac{1}{R_{eq}} \right) \left(-1 + \frac{R_{eq}}{R_M} \right) + \frac{1}{s_0} \right] \sqrt{s_0 R_{eq}} \quad (37)$$

In Eq. (32), the projection of the contact arc between ring and tools, as shown in Fig. (13), is calculated as in Eq. (38), utilizing the formulation proposed by Yang (1987).

$$L_C = \left[R_S{}^2 - \left\{ \frac{\left(R_S + R_M + s_0 - s_F \right)^2 + R_S{}^2 + R_M{}^2}{2 \left(R_S + R_M + s_0 - s_F \right)} \right\}^2 \right]^{1/2} \quad (38)$$

Differently compared with the utilization of s_0 and s_F performed in previous section 2.1.1, their meaning in equations (32-38) is the thickness of the ring before and after the deformation gap whereas $R_{eq} = \left(2R_S R_M \right) / \left(R_S + R_M \right)$.

As the model by Hawkyard (1973) presented before, also that developed by Parvizi (2011) assumes a straight line for the geometrical contact between ring and tools and, in addition to that, the position of the neutral point must be assumed in the calculation since its position is not known apriori. For these reasons, its utilization is complex and affected by high inaccuracies. In addition to that, as also highlighted in the paper, and reported in Fig. 14, the model tends to either overestimate or underestimate the radial force, depending on different thickness reduction ratios, an undesirable inconvenience if the model is meant to be utilized on industrial cases, where the thickness reduction ratio can vary even during the process, according to the deformation strategy.

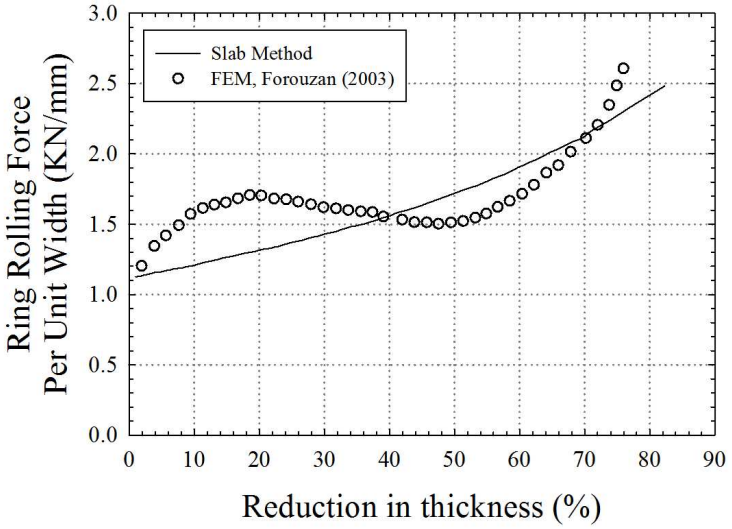

Fig. 14 – Prediction of the radial forming force operated by means of the SLAB analytical model of Parvizi (2011), in comparison to previous literature FEM results by Forouzan (2003).

Concluding the overview of the analytical models developed for the estimation of the radial forming force in the ring rolling process, Parvizi (2014) developed an upper-bound method for the power and force required during the ring rolling process, assuming admissible velocity and strain rate fields from a parametric definition of the plastic flow in the deformed region of the material.

The upper bound method is based on the virtual work principle theorem and, in case of ring rolling process the developed equation assumes the form of (39), where the three terms on the right of the equations represent the internal plastic deformation power, the frictional power at the material-rolls interface and the shear power at the plastic boundary, respectively, as also previously suggested by Ryoo (1986).

$$J^* = \frac{2}{\sqrt{3}}\sigma_y \int_V \sqrt{\frac{1}{2}\dot{\varepsilon}_{jj}\dot{\varepsilon}_{jj}}dV + mk\int_{S_f}|\Delta V_s|ds + k\int_{S_e}|\Delta V_s|ds \tag{39}$$

Thus, the force model is defined as in Eq. (40) and, once again, the radial force calculation is based on the knowledge of the neutral point location along the x-direction, which is an unknown variable.

$$F_{rad} = \left[J^* - m\frac{\sigma_y}{\sqrt{3}}\left(L_C - 2x_n\right)R_S n \right] / v_M \tag{40}$$

In Eq. (40), L_C is calculated by means of (38) and is based only on the admissible velocity field in the ring section during the deformation. Due to the fact that no information of the stress field, but only on the velocity field, are considered for the calculation of the radial force, the results should be always greater than the real value, calculated by means of numerical simulation of from experiments. However, in the result section of Parvizi (2014), when the model is compared with experiments and numerical simulations carried out by the authors, it tends to overestimate the FEM results, which is reasonable but to underestimate the experimental results. Even though the developed model is able to follow the trend of the radial force

during the ring expansion, as shown in Fig. 15, there is a high variation between minimum and maximum accuracy, especially if a third and fourth round of the rotation are considered.

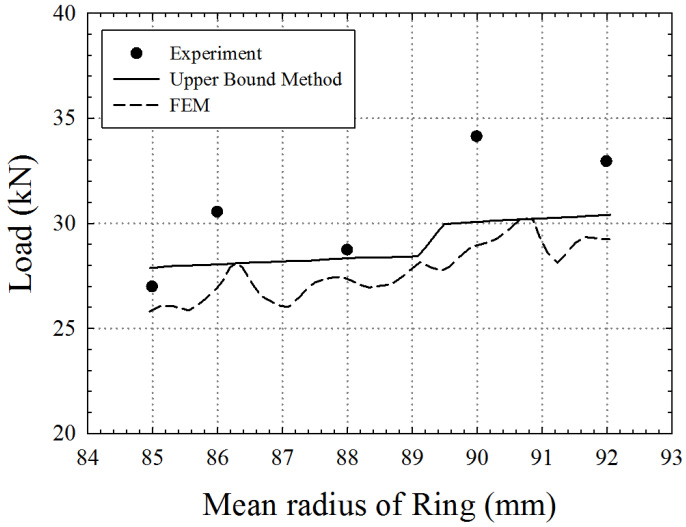

Fig. 15 – Prediction of the radial forming force operated by means of the upper-bound analytical model of Parvizi (2014), in comparison to numerical simulation and laboratory experiment.

In addition to that, as it will be shown in the result chapter 6 of the thesis, the radial force in ring rolling process steadily increases till it reaches the maximum value and, when the rolling time is over and the calibration time starts, it steadily decreases until the end of the process. However, the result present in Parvizi (2014), Fig. 15, shows a radial forming force which slightly increases until the end of the process, starting from a value around 28kN and ending with a value around 29kN, which is normally not the case in the ring rolling process.

In addition to the issues related to the inconsistency of the results concerning the underestimation of the process force, the model is also quite complex in its utilization since it requires the calculation of the strain rate and of the material flow stress, for each round of the rotation, and no information about how to calculate these values are given in the paper. Therefore, if the calculation of these values is meant to be obtained by means of numerical simulations, the computational time for the whole algorithm will considerably increase and, especially, the value of the radial forming force, as well as of other important process variables, can be derived directly from the numerical results.

As concerns analytical models for the estimation of the axial forming force, relevant for the downward movement of the upper axial roll towards the lower one, responsible for the height reduction in the ring, only a few contributions are available in the literature.

By applying a sort of pressure integration on different positions of the contact area between ring and tolls, Wang (2014) developed an analytical model for the estimation of the axial force in the RARR process. Since the contact area between the upper, or lower, axial roll and the ring is not a simple shape, Fig. 16a, it

must be subdivided into three different regions and, in order to compute the relevant contribution to the axial force, it must be integrated with respect to the y-direction, as shown in Fig. 16b.

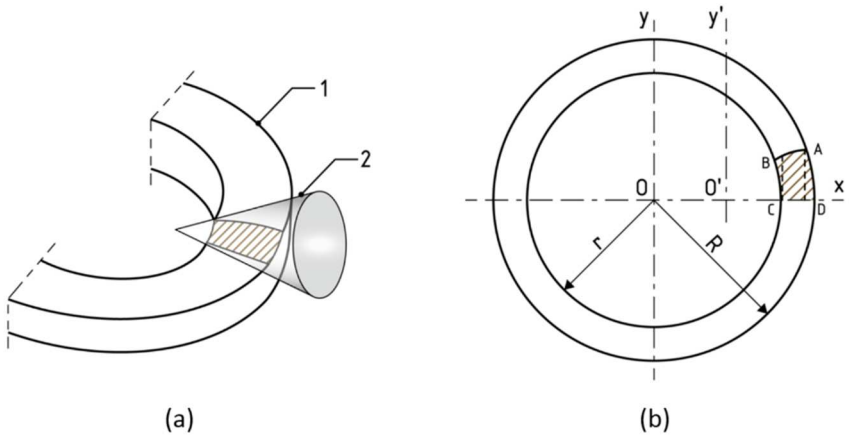

Fig. 16 – (a) Isometric and (b) top view of the contact area between the ring and the upper axial roll; (Wang 2014).

Considering the three different regions on the top surface of the ring, Fig. 16b, three different pressure contributions are identified, integrated and summed together in order to compute an initial estimation of the axial force, as summarized in Eq. (41), in integral form, and Eq. (42), in a finite form.

$$F_{ax} = \int_{x_B}^{r} dx \int_{\sqrt{r^2-x^2}}^{2RQ\sqrt{1+\frac{x-b}{RQ}}} dy + \int_{r}^{x_A} dx \int_{0}^{2RQ\sqrt{1+\frac{x-b}{RQ}}} dy + \int_{x_A}^{R} dx \int_{0}^{\sqrt{R^2-x^2}} dy \tag{41}$$

$$F_{ax} = \frac{\pi}{4}\left(R^2 - r^2\right) + \frac{4R^2Q^2}{3}\left[\sqrt{\left(1+\frac{x_A-b}{RQ}\right)^3} - \sqrt{\left(1+\frac{x_B-b}{RQ}\right)^3}\right] - \frac{x_A}{2}\sqrt{R^2-{x_A}^2} + \frac{x_B}{2}\sqrt{r^2-{x_B}^2} + \frac{r^2}{2}\arcsin\frac{x_B}{r} - \frac{R^2}{2}\arcsin\frac{x_A}{r} \tag{42}$$

The parameters in Eq. (41) and (42) are defined as following Eqs. (43)-(46), where γ is the vertex angle of the axial rolls, b is the distance between the virtual vertex of the axial roll and the inner radius of the ring and y represents the equation of the curve AB, Fig. 16b.

$$Q = \frac{z\cos\gamma - (x-b)\sin\gamma}{2\cos\gamma R} \tag{43}$$

$$y = 2RQ\sqrt{1+\frac{x-b}{RQ}} \tag{44}$$

$$x_A = \sqrt{4RQb + R^2} - 2RQ \tag{45}$$

$$x_B = \sqrt{4RQb + r^2} - 2RQ \tag{46}$$

In order to calibrate the force model, an empirical correction factor named $\bar{n}_\sigma$ is introduced in the final force model equation (47), calculated according to Eq. (48). The meaning of the empirical correction factor is not detailed in the paper as well as no comparison with neither numerical nor experimental results is reported. For these reasons, the accuracy of the proposed model is not known hence the results of the axial force estimation made with Wang (2014) model have been compared with those obtained by utilizing the developed slip line based force model, presented in the following chapter of the thesis. The cross-comparison between literature and developed models is presented in chapter 5 of the thesis.

$$F_{ax}{}' = F_{ax}\bar{n}_\sigma\sigma_s \tag{47}$$

$$\bar{n}_\sigma = 1 + \frac{R}{2s_{avg}}\left[0.72Q^2 + \left(0.59 + 0.078\frac{r}{R}\right)Q + 0.458\frac{r}{R} + 0.099\right] \tag{48}$$

In Eq. (47) σ_s represents the yield strength of the material, considered assuming a perfect plastic material behavior whereas s_{avg} the average thickness of the considered portion of the ring being deformed.

The other literature contribution dealing with the analytical estimation of the axial forming force is due to Kalyani (2015) and is based on the contact geometry considerations formalized in Alexis (2004). The force model is mainly based on the estimation of the projection of the contact made by considering the model which is normally utilized for the sheet rolling process, Eq. (49), where Δs is the thickness draft, β is the vertex angle of the axial roll and m the distance between the virtual vertex of the axial roll and the center of the ring.

$$L_C = \sqrt{\Delta s \cdot \tan\beta \cdot m} \tag{49}$$

The force model, Eq. (50), is then defined as the product between the projection of the contact arc (49), the thickness of the ring and the yield stress of the material, considered as perfect plastic.

$$F_{ax} = L_C \cdot s \cdot \sigma_s \tag{50}$$

The model has been validated by comparing the results with those of a study case in two different instants of the process, observing 16.9% and 11.4% deviation at 60 s and 180 s of the process, respectively.

2.5 Numerical models for the RARR process

In the last 20 years, several researchers have focused on developing numerical models for the study of the ring rolling process, both by utilizing commercial and specific software. Aiming to summarize the huge work available in the literature, this section of the thesis presents a summary of the main developed models and programs along with the key-results of the relevant works.

In probably one of the first complete works about numerical modelling for the ring rolling process, Utsunomiya (2002) utilized a two-dimensional implicit elastic-plastic finite element method to study the evolution of the stress in the ring throughout the process, highlighting how the sections of the ring outside the deformation gap are not stress-free but subjected to circumferential stress due to the continuity with the rest of the ring. Especially, the outer surface is subjected to compression stresses while the inner one to tensile. Considering hot ring rolling process, Song (2002) defined the first thermo-mechanical coupled FEM analysis of the ring rolling process, highlighting the repetitive thermal cycles on the mandrel and the main roll, which reflects those on the inner and the outer surface of the ring. In addition to that, by analyzing the deformation of the element in the cross-section of the ring, also the plastic flow of the material has been analyzed, allowing to hypothesize the influence of the shear stress components on inner and outer surfaces of the ring on its deformation pattern.

Another important contribution is due to Davey (2003), who utilized the arbitrary Augmented-Lagrangian-Eulerian (ALE) for the integration of the solution in ring rolling simulations, with the aim of reducing the computational time. Both accuracy and time to complete the simulation have been compared with standard approaches, allowing to conclude that when an ALE-based algorithm is fed to a Successive Preconditioned Conjugate Gradient Method (SPCGM) solver, the computational time can be largely reduced.

By utilizing a self-developed program, Yea (2003) utilized the SHAPE-RR® code for the calculation of spread, pressure distribution and roll force in the ring rolling process. The developed program is based on a rigid-plastic finite element method, aiming to reduce the computational time. The comparison between experimental and numerical results, both for flat and T-shaped rings, shows good agreement proving the reliability of the developed contact calculation algorithm as well as of the choice of utilizing a rigid-plastic material model, instead of a more complicated elastic-plastic one. The same program, SHAPE-RR®, has been also utilized by Kim (2012) to identify the combination of process parameters those allow to minimize the load during the ring rolling process. The limitation of the load required to the actuators is of key importance for the industry and it is mainly related to the mandrel and to the upper axial roll, those operate the thickness and height reduction. The developed FEM program and the relevant numerical simulation has been validated by comparison with experimental results, observing a good agreement. The proposed methodology, implemented in the developed FEM software, allows identifying the motion rules for mandrel

and upper axial roll those minimize the forming force while assuring a uniform and stable expansion of the ring throughout the process.

Due to its high-computational time, dynamic explicit numerical simulations have not been largely utilized in the beginning of the XXI century. However, in the work of Wang (2006), the commercial software ABAQUS/Explicit has been utilized for the estimation of geometrical and temperature evolution of the ring during the ring rolling process by means of elastic-plastic dynamic-explicit numerical approach. One of the main features of the dynamic-explicit developed model is the possibility of simulating the so-called fishtail effect, a typical defect related to the ring rolling process (see also Fig. 9 in section 2.1.1).

Since the spread effect in the vertical direction of the ring may also result in fishtail effect, a defect which should be avoided in order to reduce the post-operations after the ring rolling process, Guo (2006) utilized dynamic-explicit numerical simulation in the ABAQUS/Explicit environment to study the influence of the size of mandrel and main roll on the forming quality of rings. The effect of varying the roll size on the spreading effect, on the roll force and on the roll moment is studied, allowing to identify the combination which can reduce defects and, at the same time, limit the process force and moment.

In a summary work, Wang defined the basic rules for the virtual ring rolling process definition, a methodology for an integrated design of the ring rolling process by means of numerical approaches. The simulations are carried out utilizing the commercial software LS-DYNA whereas the complex control of the tools is operated by ANSYS parametric design language algorithm. The method is applied to two different complex rings whose final shapes, obtained by the numerical computations, are compared with the CAD project files, showing the close similarity. Based on the comparison with standard FEM technics, virtual ring rolling offers a reduction in the computational time while keeping a good agreement with experimental results.

Concerning the utilization of a different commercial software, Kim (2007) developed a numerical model in MSC.SuperForm to analyze the feasible forming condition for an asymmetric grooved ring, comparing the results with experimental data. Thanks to the progressive plot of the geometry of the cross-section of the ring for increasing simulation times, the increase of the geometrical defects, such as the fishtail effect, can be clearly highlighted and proper countermeasures can be identified.

In addition to that, based on the results of previous analytical works, for the setting of the motion rules of the ring rolling mill tools, Yang (2008) studied the variation of the temperature in the ring at specific locations around and inside the cross-section of the ring. The numerical simulations have been carried out by utilizing the commercial software ABAQUS/Explicit and an explicit solver. By means of numerical simulations, the effect of the material distribution in the cross-section of the ring blank is studied, defining useful guidelines for the ring blank size definition. However, since the rules are not explicitly defined and

only the inference between the variable is estimated, the results can be utilized only as a reference and not as precise guidelines.

In similarity with the work of Song (2002), Sun (2008) developed a coupled thermo-mechanical numerical simulation in ABAQUS/Explicit of the rotational speed of the main roll, of the feeding speed of the mandrel, of the initial temperature of the ring and of the friction factor on the strain and temperature evolution in the ring throughout the process. The results allow identifying the correlation between important input variables and process output, which should be accounted in order to achieve a successful production. A similar analysis in the work of Anjami (2010) who, by utilizing DEFORM-3D, studied the influence of the roll sizes on forming stability, stress distribution, side spread, and power. The results showed how the FEM approach is a useful way to predict both the strain and temperature distribution in the ring during the process, opening the way to the forecast of the microstructure and, accordingly, to the relevant mechanical properties of the ring after the production. Following a similar rationale, Gong (2012) developed a numerical simulation to study the variation of the equivalent plastic strain in the ring caused by different sizes of the rolls, namely mandrel and main roll, and of their relevant motion rules, namely, the mandrel feeding speed and the rotational speed of the main roll.

In a fully-numerical work, Qian (2013) analyzed the upsetting and piercing phases those precede the ring rolling process in order to estimate both strain and temperature thus to account for the evolution of the microstructure in the ring. One of the most important considerations, which highlights the complexity of the RARR is that the initial billet is already in a non-uniform strain and temperature state at the beginning of the ring rolling process. Same considering the whole production operations, from the upsetting to the end of the ring rolling process, Giorleo (2013) analyzed the energy consumption and proposed a numerical approach to minimize it. The reduction of the energy consumption, mainly obtained by reducing the height of the ring blank, leads to three important positive outputs, identified in upsetting energy reduction, in more precise dimensions of the ring blank and less material waste.

Concerning the utilization of processing maps for the set-up of the ring rolling process, two different contributions of Kil (2014, 2015) explore the possibility of linking the operational temperature and the strain-per-round to the dimensions of the initial ring blank, organizing the results in terms of processing maps. The proposed processing maps methodology is meant to be utilized as a guide for the design of the ring rolling process.

In the ring rolling process numerical simulations the aspect of remeshing is of key-importance but, in the literature, only a few contributions explicitly disclose the information concerning the remeshing strategies utilized in their models. In a recent work, Kim (2013) proposed a dual mesh approach for the reduction of the overall computational time by applying different refinement meshes to the deformation zone and to the remaining zones of the ring. The proposed methodology has been validated on different

process/ring combinations, showing the reliability in reducing the computational time while preserving the quality of the calculation.

In addition to the huge literature review presented in this section of the thesis, numerical models have been largely utilized for the validation of the analytical models presented in the previous sub-chapters, namely Zhou (2011), Guo (2011), Qian (2013), Zhou (2010), etc. The necessity of a large utilization of numerical simulation is given by the fact that the ring rolling is a complex and expensive manufacturing process thus the large utilization of either industrial or laboratory experiments is normally not possible.

In the following chapter of the thesis, the developed analytical models are presented in detail, highlighting their mathematical background, their features and how their combined utilization allows a full understanding of the ring rolling process, both from the kinematic and from the dynamic point of view.

Chapter 3: Analytical models for the radial-axial ring rolling process

The collection of algorithms presented in this chapter of the thesis aims to give a full analytical interpretation of the interaction between process parameters, boundary conditions, kinematic and dynamic process outputs. As stated in the introduction, the aim is to provide a useful tool which allows to quickly and precisely estimate the influence of design and manufacturing choices on important process outputs, such as the geometrical expansion of the ring, its temperature drop and the evolution of the process forces throughout the process.

As anticipated in chapter 1, the developed models are organized in the logic sequence also followed in the literature survey chapter, starting from the setting of the ring rolling process until the estimation of the process forces, considered as the last step of the calculation. These models have been developed and are utilized following this sequence because the results of a considered model are necessary as the input of the following one. Fig. 17 summarizes the basic interaction, in terms of main inputs & outputs, between each algorithm and formalizes the sequence of their utilization. The same sequence presented in Fig. 17 will be utilized for the progressive presentation of the algorithm throughout this chapter of the thesis.

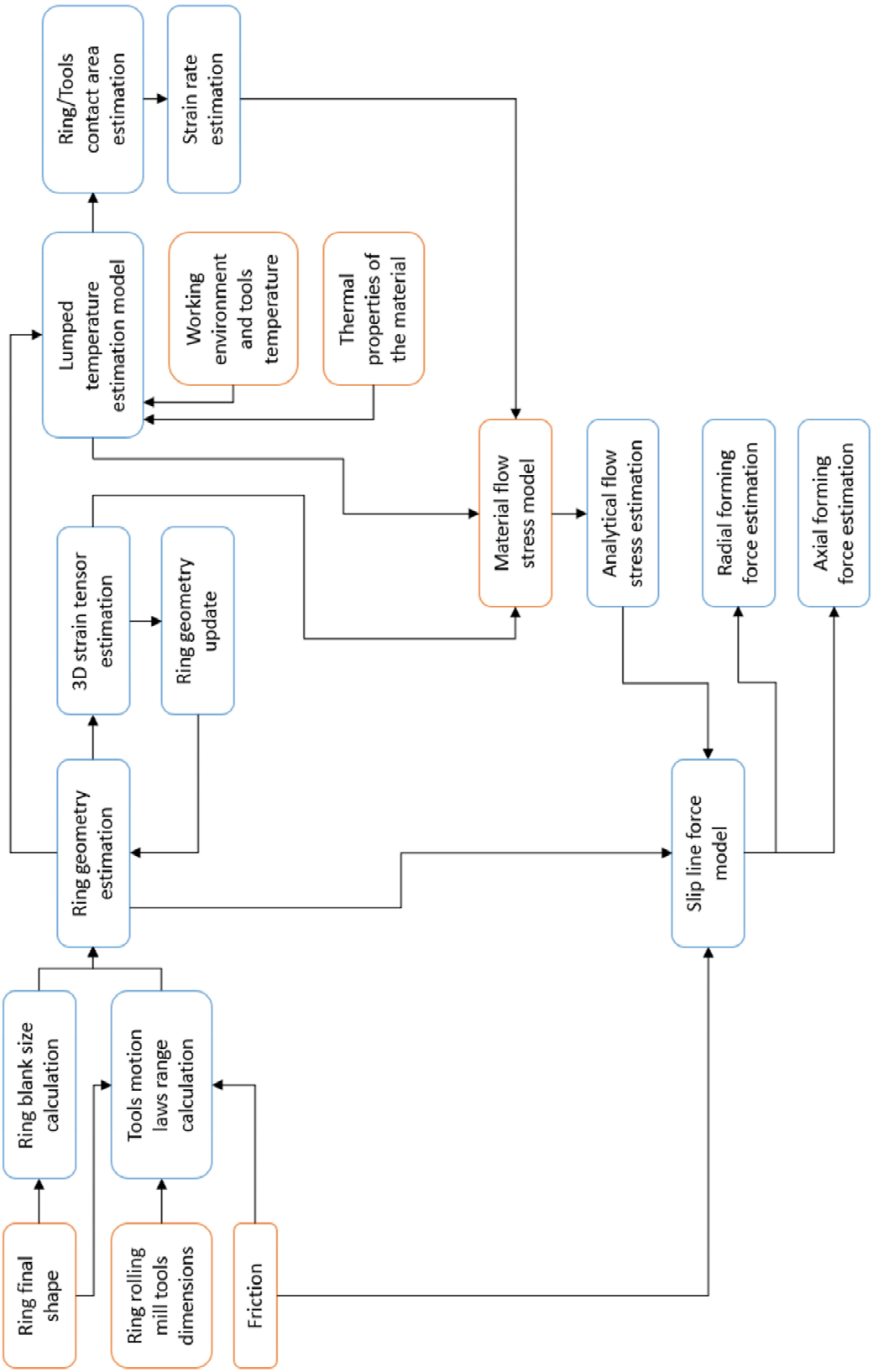

Fig. 17 – Analytical models interaction flowchart.

3.1 Calculation of the ring blank

The first step for the set-up of the ring rolling process is represented by the calculation of the ring blank sizes, which represents the initial dimensions of the ring which will be deformed during the process in order to obtain the final desired shape.

The calculation of the ring blank is based on two important aspects: the first one is represented by the volume conservation principle, typical of the plastic-predominant deformations, the second one by the Keeton's rule, presented in previous Eq. (1), section 2.1.1. The application of the Keeton's rule (1) to the initial and final dimensions of the ring, in terms of its thickness and height, results in Eq. (51).

$$h_0^{\,2} - s_0^{\,2} = h_F^{\,2} - s_F^{\,2} \tag{51}$$

Starting from (51), the following derivations lead to the final form of Eq. (55), which should be numerically solved in order to calculate the initial thickness of the ring blank.

$$\frac{h_0}{h_F} = \sqrt{1 - \left(\frac{s_f}{h_F}\right)^2 + \left(\frac{s_0}{h_F}\right)^2} \tag{52}$$

$$\pi\left(D_0^{\,2} - d_0^{\,2}\right)h_0 = \pi\left(D_F^{\,2} - d_F^{\,2}\right)h_F \tag{53}$$

$$\frac{\left(D_F + d_F\right)}{2\left(d_0 + s_0\right)} = \frac{s_0}{s_F}\sqrt{1 - \left(\frac{s_F}{h_F}\right)^2 + \left(\frac{s_0}{h_F}\right)^2} \tag{54}$$

Rearranging Eq. (54) in order to express everything in terms of the initial thickness of the ring, namely s_0, the polynomial equation (55) is obtained. The equation coefficients for (55) are summarized in (56).

$$4 \cdot s_0^{\,6} + m \cdot s_0^{\,5} + n \cdot s_0^{\,4} + p \cdot s_0^{\,3} + q \cdot s_0^{\,2} + r = 0 \tag{55}$$

$$\begin{aligned} m &= 8 \cdot d_0 \\ n &= 4\left(d_0^{\,2} + h_F^{\,2} - s_F^{\,2}\right) \\ p &= 8 \cdot d_0\left(h_F^{\,2} - s_F^{\,2}\right) \\ q &= 4 \cdot d_0^{\,2}\left(h_F^{\,2} - s_F^{\,2}\right) \\ r &= -\left(D_F + d_F\right)^2 s_F^{\,2} \cdot h_F^{\,2} \end{aligned} \tag{56}$$

According to (56), once the inner diameter of the ring blank is chosen, the thickness can be estimated and, accordingly, the remaining dimensions can be calculated as well. The inner diameter of the ring blank is normally chosen in order to limit the scrap material during the piercing operation, see Fig. 4 in chapter 1 hence, in the practice, the initial diameter of the ring, d_0, is chosen according to Eq. (57) which allows avoiding collisions between the ring and the mandrel in the initial phases of the process as well as to limit the material waste during the piercing operation.

$$1.2 \cdot D_M \leq d_0 \leq 1.4 \cdot D_M \tag{57}$$

Eq. (56) is solved by utilizing a combination of two different methods: at first, the secant method is utilized to determine the initial guess for the solution and, afterward, the Newton-Rapson algorithm is employed for the determination of the solution in terms of the thickness of the ring blank, s_0 .

Accordingly, the remaining dimensions of the ring can be determined according to Eqs. (58) and (59), in terms of outer diameter and height of the ring blank.

$$D_0 = d_0 + 2 \cdot s_0 \tag{58}$$

$$h_0 = \sqrt{{h_F}^2 - {s_F}^2 + {s_0}^2} \tag{59}$$

In comparison to the algorithm by Qian et al. (2013) presents in section 2.1.1, the proposed one takes into account both volume conservation principle and Keeton's equation (1) from the beginning of the calculation, allowing a more clear and straightforward calculation of the dimension of the ring blank.

As it will be shown in the result section, the utilization of the proposed algorithm for the determination of the ring blank dimensions allows obtaining final rings with the dimensions very close to the desired ones, limiting the fishtail effect. The algorithm for the estimation of the ring blank dimensions is included in Berti and Quagliato (2015).

3.2 Motion laws calculation algorithms

In the radial-axial ring rolling process, the key process parameters those have a high-influence on the successful production of the ring are represented by the feeding speed of mandrel and upper axial rolls. In addition to those, also the rotational and backward speed of the axial rolls have shown to influence the quality of the ring since they both can affect the stability of the process. For these reasons, in this section, these four process parameters are discussed and analytical models for their set-up are proposed and explained in details. In addition to that, concerning the main roll rotational speed, the following consideration has been drawn. In the radial-axial ring rolling process, the main roll rotational speed is normally chosen in order to limit the inertia phenomena in the ring during the process, and it is normally adjusted during the process time, no additional investigations on this parameter have been carried out and, in the calculation, the rule proposed by Zhou (2011) has been utilized (see also Eq. (8) in section 2.1.2).

Concerning the mandrel feeding speed, both literature contributions are based on the same fundamentals and, for this reason, they both share the same limitation. By utilizing the model initially proposed by Hua (1997) and subsequently again proposed by Zhou (2011), for some ring configurations in terms of diameters

and height, no solutions ranges for the mandrel feeding speed can be determined. For this reason, a new model has been developed and the derivations are hereafter detailed.

According to the slip line theory and to the force equilibrium in the mandrel-main roll deformation gap, two different conditions related to the plastic deformation in the ring cross-section are identified. The first one, named as penetration condition, is related to the fact that in order to obtain full plastic deformation all over the thickness of the ring, a minimum thickness draft should be granted. The latter one instead states that there is an upper limit for the thickness draft over which the backward friction force, caused by the pressure of the rolls on the ring, is greater than the forward friction force which allows the ring to be drawn and to exit the deformation gap. If this limit value is outdone, the ring is blocked inside the deformation gap and the ring stops its rotation.

The initial derivation is the same as that proposed in Hua (1997) and detailed in previous section 2.1.3, and is not repeated here. However, the main difference between the literature models, Hua (1997) and Zhou (2011), and the proposed one is related to the time-dependent law of the mandrel feeding speed. In the literature, authors proposed a constant mandrel feeding speed for the whole rolling time, a choice that does not follow the natural increase of the ring diameter. According to this choice, it may happen that the ring expanses too slowly in the first part of the process and too fast in the last one, resulting in possible instability of its growth.

To overcome this limitation, different ranges for the mandrel feeding speed have been calculated for the beginning and for the end of the rolling process, linking them to the initial and to the final geometry of the ring as well as to the initial and to the final positions of the tools of the ring rolling. The proposed approach is detailed in Berti and Quagliato (2015). An example of the difference between the literature mandrel feeding speed approach, i.e. Hua (1997) and Zhou (2011), and the proposed one, Berti and Quagliato (2015), is shown in Fig. 18. The proposed approach and the relevant explanation is hereafter detailed.

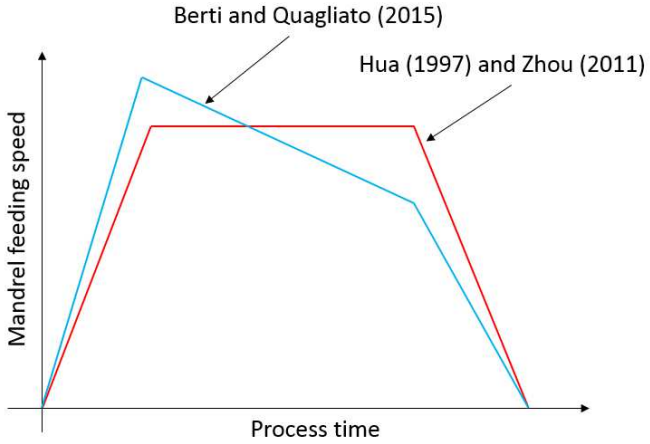

Fig. 18 – Comparison between literature and proposed mandrel feeding speed rule.

In previous Eqs. (17) and (18), generic inner and outer radii of the ring were defined in the model and, especially in Zhou (2011), the calculation of the feasible ranges for the mandrel feeding speed has been linked to the initial geometry of the ring. However, in the proposed approach, the initial mandrel feeding, relevant for the beginning of the rolling time, is chosen inside the range defined by Eq. (60), same linked to the initial geometry of the ring and to the dimensions of the tools of the ring rolling mill. In addition to that, in order to define the ranges in which to choose the final mandrel feeding speed, also the final geometry of the ring is accounted for, as shown in Eq. (61).

$$\frac{\omega_R R_R 6.55\cdot 10^{-3}\left(R_0-r_0\right)^2\left(\frac{1}{R_R}+\frac{1}{R_M}+\frac{1}{R_0}-\frac{1}{r_0}\right)}{2\pi R_0}<\left[v_M\right]_0<\frac{\omega_R R_R\frac{2\beta_R{}^2}{\left(\frac{1}{R_R}+\frac{1}{R_M}\right)^2}\left(\frac{1}{R_R}+\frac{1}{R_M}+\frac{1}{R_0}-\frac{1}{r_0}\right)}{2\pi R_0} \tag{60}$$

$$\frac{\omega_R R_R 6.55\cdot 10^{-3}\left(R_F-r_F\right)^2\left(\frac{1}{R_R}+\frac{1}{R_M}+\frac{1}{R_F}-\frac{1}{r_F}\right)}{2\pi R_F}<\left[v_M\right]_F<\frac{\omega_R R_R\frac{2\beta_R{}^2}{\left(\frac{1}{R_R}+\frac{1}{R_M}\right)^2}\left(\frac{1}{R_R}+\frac{1}{R_M}+\frac{1}{R_F}-\frac{1}{r_F}\right)}{2\pi R_F} \tag{61}$$

Especially in case of large deformations, resulting in huge geometrical differences between the initial and the final geometry of the ring, the proposed approach results in a better stability of the process and allows always calculating feasible process parameters closer to an optimal process setup.

According to Eqs. (60) and (61), also the axial roll feeding speed can be defined accounting for the mutual interactions between thickness and height draft. Same as for the case of the mandrel feeding speed, also for the upper axial roll feeding speed a minimum and maximum range are defined, Eq. (62).

$$v_{A,\min}=\frac{\omega_S R_S \Delta h_{\min}}{2\pi R} \quad ; \quad v_{A,\max}=\frac{\omega_S R_S \Delta h_{\max}}{2\pi R} \tag{62}$$

Considering the relationship between thickness and height defined by the Keeton's rule (1), the ranges in which to choose initial and final upper axial roll feeding speed are not independent but linked to mandrel feeding speed ranges, as shown in Eq. (63).

$$\left[v_A\right]_0=\left[v_M\right]_0\frac{s_0}{h_0} \quad ; \quad \left[v_A\right]_F=\left[v_M\right]_F\frac{s_F}{h_F} \tag{63}$$

Considering together Eq. (63) and previous Eqs. (60) and (61), the feasible ranges in which to choose initial and final feeding speed for the upper axial roll are calculated as in (64) and (65).

$$\frac{\omega_R R_R\frac{0.0131\cdot h_0{}^2}{\left(L_0-\frac{s_0}{2}\right)\tan\left(\frac{\theta}{2}\right)}}{2\pi R_0}<\left[v_A\right]_0<\frac{4\omega_R R_R 4\beta_A{}^2\left(L_0-\frac{s_0}{2}\right)\tan\left(\frac{\theta}{2}\right)}{2\pi R_0} \tag{64}$$

$$\frac{\omega_R R_R \dfrac{0.0131 \cdot h_F^{\,2}}{\left(L_F - \dfrac{s_F}{2}\right)\tan\left(\dfrac{\theta}{2}\right)}}{2\pi R_F} < \left[v_A\right]_F < \frac{4\omega_R R_R 4\beta_A^{\,2}\left(L_F - \dfrac{s_F}{2}\right)\tan\left(\dfrac{\theta}{2}\right)}{2\pi R_F} \tag{65}$$

In Eq. (64) and (65), L_0, L_F and θ parameters are defined as shown in Fig. 19.

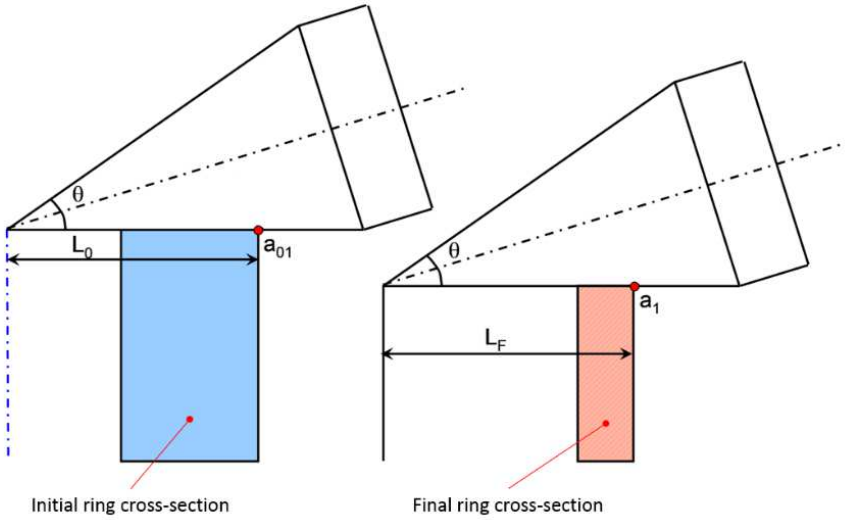

Fig. 19 – Ring-axial rolls contact points definition.

It is immediately clear that both the ranges for the upper axial roll feeding speed and the relevant choices for the speeds to use in the process are not independent of the mandrel feeding speed ranges and the relevant initial and final chosen speeds for the mandrel. This fact results in a step-by-step calculation, as follows. First of all the mandrel feeding speed ranges are calculated, one for the beginning (60) and one for the end (61) of the process. Accordingly, the upper axial rolls feeding speed ranges can be calculated by means of (64) and (65), for the beginning and the end of the process respectively.

Afterwards, the user chooses the initial and final mandrel feeding speeds inside the previously-calculated ranges (60) and (61); this choice is basically free and does not influence the quality of the resulting ring, even if can affect the residual stresses and the hardening of the material, both out of the scope of this investigation, as well as the total time for rolling process.. Finally, once the mandrel feeding speeds have been chosen inside the relevant ranges, the upper axial rolls feeding speeds are automatically calculated, as a result of the choice of the mandrel ones. Since the initial and final upper axial roll feeding speeds are not chosen but calculated on the basis of the mandrel ones, it must be verified that they both fall inside their relevant prescribed ranges. If so, the process can be set up by utilizing the set of two mandrel feeding speed and two upper axial roll feeding speed as chosen and calculated. Otherwise, if one or both the calculated upper axial roll feeding speeds do not fall within the prescribed ranges, different mandrel feeding speeds should be chosen and the verification procedure should be repeated.

Once the mandrel and upper axial roll feeding speeds ranges are defined, also the backward speed and the rotational speeds of the axial rolls can be calculated as well. These two process parameters are both related to the axial rolls but accomplish different tasks in the process. The backward movement of the axial rolls allows promoting a circular shape of the ring, following and guiding its expansion throughout the process. If this parameter is not properly set, the ring will tend to evolve in an irregular shape, either in the x-direction or in the y-direction. On the other hand, the rotational speed of the axial rolls facilitates the rotation of the ring during the process and avoids the arising of velocity gradients due to the friction between the rolls and the top and bottom surfaces of the ring. A complete review of the approaches which can be adopted in order to control the backward movement of the axial rolls is presented in Zhou (2012). As also suggested in Berti and Quagliato (2015), a reasonable approach is to directly link the backward speed of the axial rolls to the growth of the ring, in terms of its diameters. The growing speed of the ring is addressed in the following section of the thesis and is mainly related to the choice of a linear decreasing mandrel feeding speed. In general, the chosen approach for the setting of the axial rolls backward movement is to keep constant, throughout the process, the contact points between ring and rolls, adjusting the motion in order to have $L_0 = L_F$, as defined in Fig. 20.

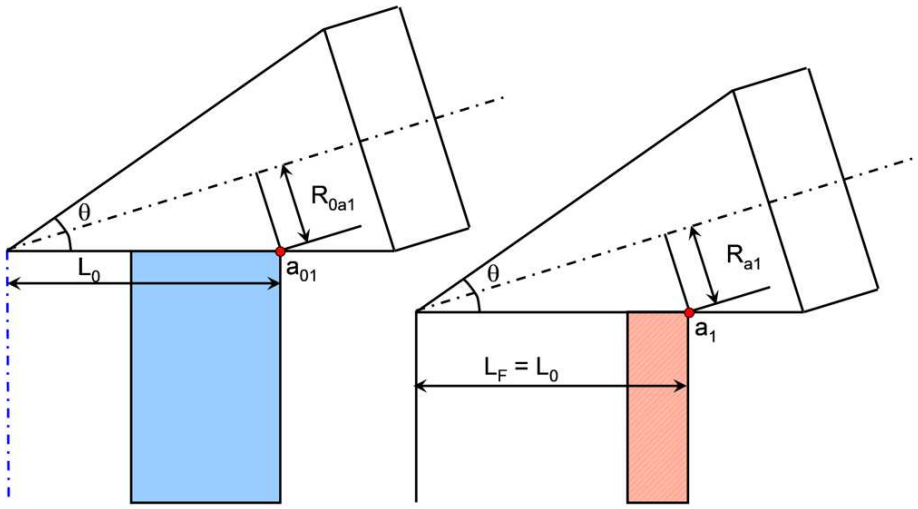

Fig. 20 – Reciprocal position of ring and axial rolls during the process.

Finally, concerning the rotational speed of the axial rolls, its setting is done according to the tangential speed ratio with the main roll rotational speed, as shown in (66) where R_{a1} is defined as the local radius of the section of the axial rolls in contact with the outer radius of the ring.

$$\omega_S R_S = \omega_A R_{a1} \tag{66}$$

$$\omega_A = \frac{\omega_S R_S}{R_{a1}} = \frac{\omega_S R_S}{L_0 \sin(\theta/2)} \tag{67}$$

Once the rotational speed of the main roll is chosen, that of the axial rolls is immediately calculated according to Eq. (67), where R_{a1} is defined as a function of L_0. If the distance between ring and vertex of the axial rolls changes during the process, thus $L_F \neq L_0$, the axial rolls rotational speed ω_A can be calculated in order to follow this variation. However, if $L_0 = L_F$ it shall result in a constant rotational speed for the axial roll throughout the process.

The full equations set presented in the section allows to set-up a generic ring rolling process with a full understanding of the fundamentals concerning the kinematics and of the mutual interactions between ring and tools dimensions. The proposed equations for the calculation of both ranges and process parameters have been utilized for the setting of both numerical simulations and laboratory experiments presented in chapter 4 and 5 of the thesis, respectively.

In the following sections of chapter 3, the developed models for the control of the influence of the chosen process parameters on the ring and on the tools are presented.

3.3 Geometry evolution of the ring

As anticipated in the introduction chapter, all the calculations concerning the developed models are based on the concept of *ring slice*, Fig. 6. The slice is a circumferential portion of the ring utilized as an elementary control element and, starting from the estimation of the geometry of the ring until the calculation of the process forces. With the exception of the lumped temperature model, section 3.5, all the remaining algorithms presented in sections 3.3, 3.4, 3.6 and 3.7 are slice-based, which means that the relevant outputs of the algorithms can be estimated for each slice in which the ring has been subdivided and for each round of the process. Considering the ring at the beginning of the ring rolling process, it can be subdivided in a certain amount of slice, each one with the same radii, thickness, and height. However, during the rolling process, each slice will be deformed according to its relevant position in the ring and according to the motion laws of the mandrel and upper axial roll. This fact is of key importance and allows accounting for the intrinsic incremental nature of the ring rolling process. In addition to that, the subdivision of the ring into slices allows a more precise and realistic estimation of the geometry of the ring during the process, as it will be highlighted in the result section, where the results of the estimation of the outer diameter of the ring obtained by utilizing the literature model proposed by Zhou (2011) are compared with those obtained by the model presented in this section of the thesis. The increase in accuracy is clearly evident especially at the end of the rolling process, since the literature model does not account for the calibration phase, as it is done for the developed one, instead.

As mentioned above, before the beginning of the process, the ring is subdivided into a certain number of n slices and, accordingly, the vertex angle of each slice is estimated as $\vartheta_{j,0} = 2\pi / n$. The subscript refers

to the generic j-slice in the 0-round of the process, thus before the beginning of the rolling. In addition to that, based on to the choice of the initial and the final mandrel feeding speeds operated according to the model presented in the previous section of the thesis, the linear decreasing mandrel feeding speed is defined as in Eq. (68) where t_M are the mandrel feeding time and t the time variable, respectively.

$$v_M(t) = [v_M]_0 + \left(\frac{[v_M]_F - [v_M]_0}{t_M} \right) t \tag{68}$$

By integrating, over time, Eq. (68), the time-dependent law for the thickness of the ring in the mandrel-main roll deformation gap can be calculated as in (69).

$$s_j(t) = s_0 - \int_0^{t_j} v_M(t)\,dt = s_0 - \left[\left(\frac{[v_M]_F - [v_M]_0}{t_{cycle-M}} \right) \frac{t_j^{\,2}}{2} + [v_M]_0\, t_j \right] \tag{69}$$

It is important to underline that the (69) defines both the relevant distance between the mandrel and main roll as well as the instantaneous thickness of the generic j-slice of the ring, passing through the mandrel-main roll deformation gap, at a specific time instant t_j. Assuming no slippage between ring and tools, the time required to deform the ring in the first round of the process, or in order words, for the first slice to rotate 360°, is defined based on the gear ratio between the main roll radius of the outer radius of the ring blank, as shown in Eq. (70).

$$t_1 = \frac{2\pi}{\omega_S} \frac{R_{j,0}}{R_S} \tag{70}$$

In the first round of the process, all the slices start with the same initial geometry thus the time required for a generic slice to enter and exit the deformation gap is same for all of the n-slice and is estimated as $t_{j,1} = t_1 / n$.

The generic slice is located at the angular position $\alpha_j = \delta \cdot j$, where $j = 1...n$, as shown in Fig. 21a, and at the end of the first round, it has been deformed according to its position in the ring. If the j-slice is located between 0° and 180° (right half of the ring, which rotates clockwise), it has passed through both the mandrel and the axial rolls gap and has been reduced in both thickness and height. For this reason, the corresponding deformed thickness of this slice results in $s_{j,1} = s(t_{j,1})$ for $0 \le j < n/2$ whereas the deformed height is calculated according to Eq. (71), derived from (1).

$$h_{j,1} = \sqrt{(h_0^{\,2} - s_0^{\,2}) - s_{j,1}^{\,2}} \tag{71}$$

If the j-slice is located between 180° and 360° (left half of the ring, which rotates clockwise), it has passed only through the mandrel gap and is reduced only in thickness, therefore $s_j = s(t_{j,1})$ for $n/2 \le j < n$

and height corresponds to the initial height of the blank, namely h_0. Considering the volume of each slice as a constant throughout the process, the increase in the linear length of the slice, as a consequence of the deformation operated in the two deformation gaps can be calculated according to Eq. (72).

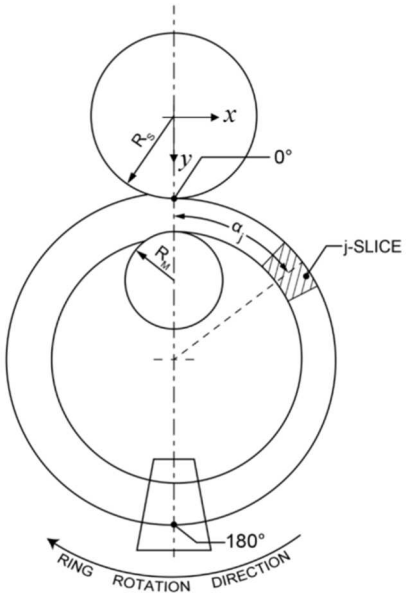

Fig. 21 – Position of the generic j-slice in the ring.

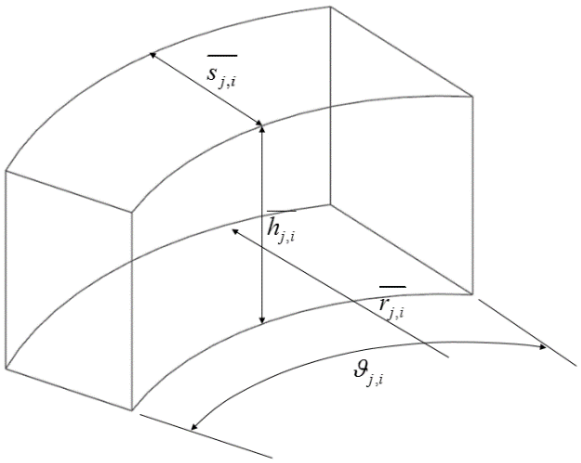

Fig. 22 – Average dimensions of the j-slice.

$$L_{f,j,1} = \frac{V_{j,0}}{\overline{s_{j,i}} \cdot \overline{h_{j,i}}} \tag{72}$$

In (72), $V_{j,0}$ represents the volume the generic j-slice whereas $\overline{s_{j,i}}$ and $\overline{h_{j,i}}$ the average thickness and average height of the generic j-slice, respectively. The need for an average thickness and height calculation is given by the fact that, in principle, left and right faces of each slice shall have different dimensions since they pass through the relevant deformation gaps at different time instants. To average the dimensions of left and right face, both thickness and height are considered as calculated in the center of the slice, as shown in Fig. 22. In order to estimate the average radius for each slice, an average radius of the whole ring in the first round of the process, namely $\overline{r_1}$, should be estimated as shown in (73).

$$\overline{r_1} = \frac{\sum_{j=1}^{n} L_{f,j,i}}{2\pi} \tag{73}$$

Since the ring rolling process pertains to the incremental forming processes, the average radius (73) is the average value of a maximum radius and a minimum radius. The first one can be estimated as $\overline{r_{1,\max}} = 2\overline{r_1} - r_0$ whereas the latter one is equal to the average radius of the ring blank, namely

$\overline{r_{1,\min}} = (R_0 + r_0)/2$. Based on the position of a generic j-slice in the ring, its average radius at the end of the first round of the process can be estimated according to (74).

$$\overline{r_{j,1}} = \frac{\left(\overline{r_{1,\max}} - \overline{r_0}\right) \sum_{k=1}^{j} L_{f,j,1}}{\sum_{k=1}^{n} L_{f,j,1}} + \overline{r_0} \tag{74}$$

In (74), the $\sum_{k=1}^{j} L_{f,j,1}$ term represents the summation of the slice linear length until the designated j-slice and allows accounting for the different deformations in the slice as a consequence if its relevant position in the ring and of the time-based deformation operated by the mandrel and the upper axial roll.

Once the average radius of each slice at the end of the first round of the process is known, by adding and subtracting half of the thickness, the outer and inner radius can be estimated. These radii are not constant but, once again, dependent on the relevant position of the slice in the ring.

So far, only the geometry of after the first round of the process has been estimated thus, in order to estimate that of the following rounds, a slightly different procedure should be adopted, as hereafter shown.

Considering the generic j-slice, from the second round on, the time required for its deformation is not constant anymore since each slice has a different length $L_{f,j,i}$. In addition to that, the vertex angles of all the slices are different each other and are related to the slices length by Eq. (75), Fig. 22, where $\overline{r_{j\text{-}1,i}}$ represents the average radius of the j-1 slice that precedes the j-slice.

$$\vartheta_{j,i} = \frac{L_{f,j,i}}{\frac{\overline{r_{j\text{-}1,i}} + \overline{r_{j,i}}}{2}} \tag{75}$$

Considering the second round of the process, the values of the outer radii of the ring for all the slices are known and, considering two consecutive slices, namely the j-1 slice and the j-slice, the external length of the generic j-slice, estimated on the outer surface of the ring, can be estimated as in (76).

$$L_{ext,j,i} = \frac{R_{j\text{-}1,i} + R_{j,i}}{2} \vartheta_{j,i} \tag{76}$$

The external length of the generic j-slice can be utilized for the calculation of its deformation time, Eq. (77). The summation of all the $t_{j,i}$ contributions over all the n-slices allows calculating the total rolling time for each i-round of the process.

$$t_{j,i} = \frac{L_{ext,j,i}}{\omega_S R_S} \tag{77}$$

Once the total deformation time for the generic i-round of the process is known, previous Eq. (72) can be utilized for the estimation of the slice length, calculated in its middle, based on the time-dependent evolution of both thickness and height of the ring, calculated according to (69) and (71), respectively.

For the generic i-round, the average and maximum radius for the whole ring are estimated as in (78) and (79), respectively. In (79), $\overline{r_{\mathrm{i-1,max}}} = \overline{r_{\mathrm{i,min}}}$.

$$\overline{r_i} = \frac{\sum_{j=1}^{n} L_{f,j,i}}{2\pi} \tag{78}$$

$$\overline{r_{\mathrm{i,max}}} = 2\overline{r_i} - \overline{r_{\mathrm{i-1,max}}} \tag{79}$$

Accordingly, the average radius for each slice in the generic i-round of the process is estimated according to (80), which is the extension of (74) to the rounds following the first one.

$$\overline{r_{j,i}} = \frac{\left(\overline{r_{i,\max}} - \overline{r_{i,\min}}\right) \sum_{k=1}^{j} L_{f,j,1}}{\sum_{k=1}^{n} L_{f,j,1}} + \overline{r_{i-1,\max}} \tag{80}$$

In conclusion, inner and out radius of the ring for a generic round of the process are calculated as in Eqs. (81) and (82) and, along with Eqs. (69) and (71), allow a fully analytical prediction of the ring geometrical expansion throughout the process.

$$r_{j,i} = \overline{r_{j,i}} - \frac{\overline{s_{j,i}}}{2} \tag{81}$$

$$R_{j,i} = \overline{r_{j,i}} + \frac{\overline{s_{j,i}}}{2} \tag{82}$$

The advantages of the proposed approach, in comparison to that available in the literature, will be highlighted and clarified in the result section, where the results of these two models are compared. In addition to that, all the analytical models presented in the following sections of chapter 3 are all based on the geometry estimation algorithm just presented, which is considered the core of the proposed approach.

The geometry estimation algorithm is included in Berti and Quagliato (2015).

3.4 3D strain tensor estimation and geometry update

Based on the slice-based estimation of the geometry of the ring throughout the process, the natural consequence is the estimation of the relevant strains in the ring during the process. The importance of the estimation of the strain is twofold since it allows a better understanding of the plastic flow of the material in slice volume during the process as well as is one of the key information for the estimation of the flow stress of the material, subsequently presented in section 3.6.

The estimation of the strain presents one key-issue, represented by the interpretation of the state of strain in the ring, namely in one of its slices, during the process. In the literature, several researchers assimilated the deformation in the ring to a state of plane strain or, in other words, when a portion of the ring is deformed in one of the two deformation gaps one deformation, and the relevant strain, is controlled by the distance

between the tools and, by means of volume constancy, the second deformation, and the relevant strain, is oriented along the circumferential direction, causing the expansion of the ring, being the strain in the third direction equal to 0 (plane strain state assumption). However, the adoption of a plane strain assumption seems to be far from the real state of the strain the portion of the ring undergoing the deformation, either in the mandrel-main roll or in the axial rolls deformation gap since the so-called spreading effect, Fig. 23.

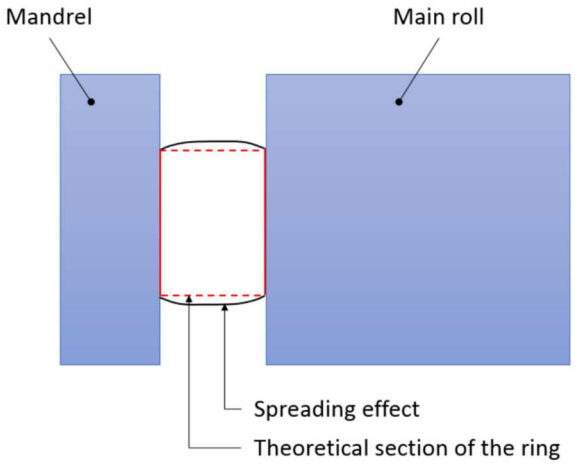

Fig. 23 – Spreading effect in the mandrel-main roll deformation gap.

The consequence of the spreading effect is to introduce a undesired material flow in the third direction, i.e. z-direction in the mandrel-main roll gap as shown in Fig. 23, partially reducing the material flow in the circumferential direction. This fact results in three different strain components along the three directions and differs from the assumption of a state of plane strain. For this reason, the developed algorithm aims to estimate the 3D principal strain tensor in each slice of the ring and for each round of the process, accounting for the radial, the axial and the circumferential strains, directly or indirectly caused by the feeding motions of the tools.

In order to properly and separately estimate the strain components in each slice of the ring after each pass in both deformation gap, the algorithm for the estimation of the geometry should be updated in order to account for the spreading effect. The spreading effect influences both the estimation of the strain components in the considered deformation gap as well as introduces a variation of the geometry of the ring in the not-controlled directions, namely the vertical direction in the mandrel-main roll gap and the radial direction in the axial rolls one.

To account for this geometry update, the geometrical parameters of each slice are not estimated anymore in its center but on both its left and right face, thus considering the incremental nature of the ring rolling process. According to the approach, each slice is now described by ten geometrical parameters, five for its left face and five for its right one. In addition to that, two slice parameters are also defined: the vertex angle of the slice $\vartheta_{j,i}$ and the average radius for the whole slice $\overline{r_{j,i}}$. All parameters are shown in Fig. 24.

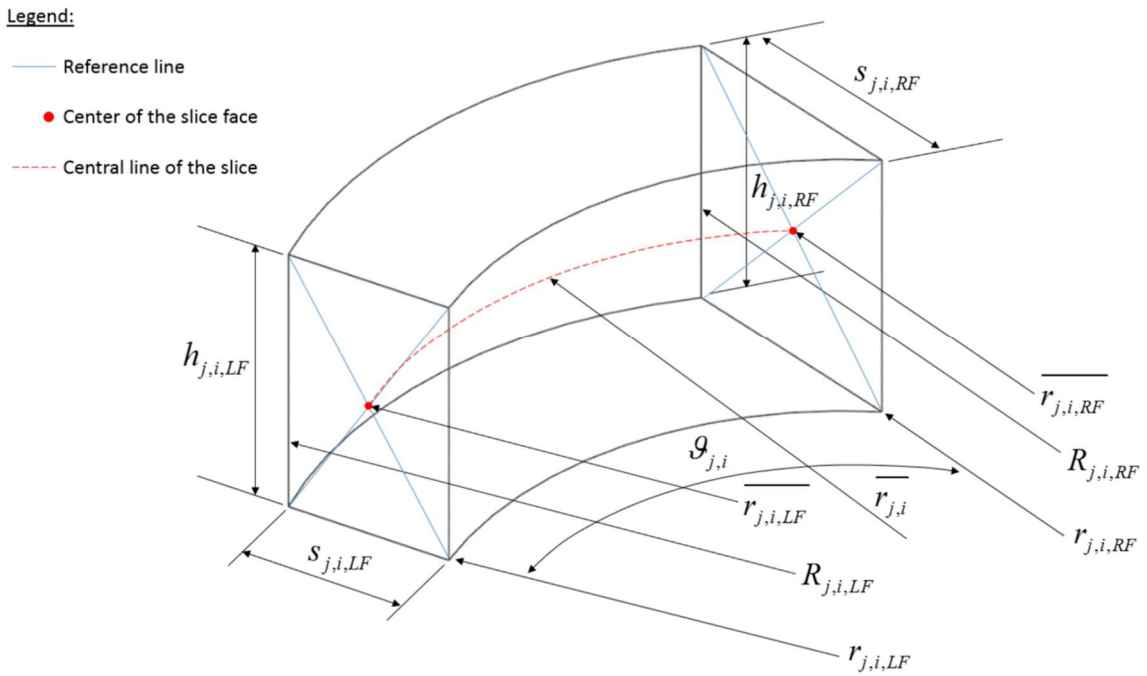

Fig. 24 – Slice parameters in the geometry update algorithm.

For a better understanding, all the parameters relevant for the left face of the slice have an "LF" subscript whereas those relevant for the right face an "RF" subscript, instead. In addition that, since the calculation is differentiated between the mandrel-main roll deformation gap and the axial rolls gap, the subscript "M" is utilized to indicate the first one whereas "A" for the second one. For instance, $r_{j,i,LF,M}$ represents the inner radius of the left face of the j-slice in the i-round after the deformation occurring in the mandrel-main roll deformation gap.

Considering the evolution of both thickness and height, as defined by Eqs. (69) and (71), the variation of the linear length of each slice can be mapped after both deformation gaps according to (83) and (84), relevant for the mandrel-main roll gap and for the axial rolls gap, respectively.

$$Lf_{j,i,M} = \frac{V_j}{\left(\frac{s_{j,i} + s_{j\text{-}1,i}}{2}\right)\left(\frac{h_{j,i\text{-}1} + h_{j\text{-}1,i\text{-}1}}{2}\right)} \tag{83}$$

$$Lf_{j,i,A} = \frac{V_j}{\left(\frac{s_{j,i} + s_{j\text{-}1,i}}{2}\right)\left(\frac{h_{j,i} + h_{j-1,i}}{2}\right)} = Lf_{j,i} \tag{84}$$

The value of the linear length of the slice after the axial rolls deformation gaps is equal to the final linear length of the j-slice in the i-round, as previously calculated by (72). Accordingly, also the variation of the slice vertex angle, after both deformation gaps, can be estimated by adopting similar formulations, but

taking into account the two different deformations occurring during the process, as shown in following Eqs. (85) and (86).

$$\vartheta_{j,i,M} = \vartheta_{i\text{-}1,j} + \frac{\left(Lf_{j,i,M} - Lf_{j,i\text{-}1,}\right)}{\left(Lf_{j,i} - Lf_{j,i\text{-}1}\right)}\left(\vartheta_{j,i} - \vartheta_{j,i\text{-}1}\right) \tag{85}$$

$$\vartheta_{j,i,A} = \vartheta_{j,i\text{-}1} + \frac{\left(Lf_{j,i,A} - Lf_{j,i\text{-}1}\right)}{\left(Lf_{j,i} - Lf_{j,i\text{-}1}\right)}\left(\vartheta_{j,i} - \vartheta_{j,i\text{-}1}\right) = \vartheta_{j,i} \tag{86}$$

Both $Lf_{j,i,X}$ and $\vartheta_{j,i,X}$ are slice parameters and, for this reason, are referred neither to the left nor to the right face of the slice. In addition to that, based on these two slice-based parameters, the average radius of each slice, after both deformation gaps, can be estimated as shown in (87) those are the central radii of the slice after mandrel-main roll deformation gap and after the axial roll deformation gap, respectively.

$$\overline{r_{j,i,M}} = \frac{Lf_{j,i,M}}{\vartheta_{j,i,M}} \quad ; \quad \overline{r_{j,i,A}} = \frac{Lf_{j,i,A}}{\vartheta_{j,i,A}} \tag{87}$$

Since the real length of the slice can be reasonably approximated by a circumference arc with an averaged vertex angle (see Eqs. (85) and (86)) and an averaged radius for the whole slice (see Eq. (87)), the same reasoning can be adopted for the estimation of the intermediate radii for the left and right faces of the slice considering a linear correlation between these radii and the values of the vertex angles previously calculated in Eqs. (85) and (86). This results in following Eqs. (88) and (89) those are the first estimation of the intermediate radii of a generic j-slice in the i-round after the deformation occurred in the mandrel-main roll deformation gap.

$$\tilde{r}_{j,i,LF,M} = \overline{r_{j,i\text{-}1}} + \frac{\left(\vartheta_{j,i,M} - \vartheta_{j,i\text{-}1}\right)}{\left(\vartheta_{j,i} - \vartheta_{j,i\text{-}1}\right)}\left(\overline{r_{j,i}} - \overline{r_{j,i\text{-}1}}\right) \tag{88}$$

$$\tilde{r}_{j,i,RF,M} = \overline{r_{j-1,i\text{-}1}} + \frac{\left(\vartheta_{j,i,M} - \vartheta_{j,i\text{-}1}\right)}{\left(\vartheta_{j,i} - \vartheta_{j,i\text{-}1}\right)}\left(\overline{r_{j\text{-}1,i}} - \overline{r_{j\text{-}1,i\text{-}1}}\right) \tag{89}$$

Although the assumption of a circular shape for the slice allowed calculating a first estimation of the intermediate radii of left and right faces, it also results in a loss of volume for the slice, which can be corrected by redistributing the material along the slice circumference, as shown in Eqs. (90) and (91).

$$r_{j,i,LF,M} = \overline{r_{j,i\text{-}1}} + \frac{\left(\vartheta_{j,i,M} - \vartheta_{j,i\text{-}1}\right)}{\left(\vartheta_{j,i} - \vartheta_{j,i\text{-}1}\right)}\left(\overline{r_{j,i}} - \overline{r_{j,i\text{-}1}}\right)\frac{\overline{r_{j,i,M}}}{\left(\frac{\tilde{r}_{j,i,LF,M} + \tilde{r}_{j,i,RF,M}}{2}\right)} \tag{90}$$

$$r_{j,i,RF,M} = \overline{r_{j-1,i-1}} + \frac{\left(\vartheta_{j,i,M} - \vartheta_{j,i-1}\right)}{\left(\vartheta_{j,i} - \vartheta_{j,i-1}\right)}\left(\overline{r_{j-1,i}} - \overline{r_{j-1,i-1}}\right)\frac{\overline{r_{j,i,M}}}{\left(\frac{\tilde{r}_{j,i,LF,M} + \tilde{r}_{j,i,RF,M}}{2}\right)} \tag{91}$$

Finally, inner and outer radii for left and right face of the generic slice can be calculated, as shown in Eqs. (92)-(95).

$$r_{j,i,LF,M} = \overline{r_{j,i,LF,M}} - \frac{s_{j,i}}{2} \tag{92}$$

$$R_{j,i,LF,M} = \overline{r_{j,i,LF,M}} + \frac{s_{j,i}}{2} \tag{93}$$

$$r_{j,i,RF,M} = \overline{r_{j,i,RF,M}} - \frac{s_{j-1,i}}{2} \tag{94}$$

$$R_{j,i,RF,M} = \overline{r_{j,i,RF,M}} - \frac{s_{j-1,i}}{2} \tag{95}$$

Along with previous Eqs. (69) and (71), this set of equations allows a fully analytical prediction of the expansion of the ring and accounts for the different dimensions of left and right face of each slice of the ring as a consequence of the incremental nature of the ring rolling process. The derivations detailed Eq. (88) to Eq. (95) can be repeated also for the axial roll deformation gap, by following the same procedure.

According to the precise estimation of the ring geometry detailed so far, also the strain evolution in the ring can be estimated. The strain estimation is a procedure which is going to be partially overlapped with the geometry estimation due to the fact that, based on the estimation of the third strain component also the geometry of the ring will be updated.

Based on the precise estimation of the circumferential growth of the ring, as it will be shown in the results section, the author has chosen to directly calculate the circumferential strain as homogenous in the slice. Hence, the circumferential strain is estimated, after each deformation gap, by adopting Eqs. (96) and (97), for the strain after the mandrel-main roll deformation gap and after the axial rolls gap, respectively. The following procedure is derived for the inner radius of a slice deformed in the mandrel-main roll deformation gap but can be easily extended to the outer radius and to the axial rolls deformation gap by substituting the relevant parameters.

$$\varepsilon_{c,j,i,M} = \ln\left[\left(\frac{r_{j,i,LF,M} + r_{j,i,RF,M}}{2}\right)\frac{\vartheta_{j,i,M}}{\left(\vartheta_{j,0} \cdot r_{j,0}\right)}\right] \tag{96}$$

$$\varepsilon_{c,j,i,A} = \ln\left[\left(\frac{r_{j,i,LF,A} + r_{j,i,RF,A}}{2}\right)\frac{\vartheta_{j,i,A}}{\left(\vartheta_{j,0} \cdot r_{j,0}\right)}\right] \tag{97}$$

For two consecutive rounds of the process and considering the circumferential strain, the incremental strains in the circumferential direction can be calculated as in (98) and (99).

$$d\varepsilon_{c,j,i,M} = \varepsilon_{c,j,i,M} - \varepsilon_{c,j,i-1,A} \tag{98}$$

$$d\varepsilon_{c,j,i,A} = \varepsilon_{c,j,i,A} - \varepsilon_{c,j,i,M} \tag{99}$$

Eq. (98) accounts for the fact that the geometry of a generic slice entering the mandrel-main roll deformation gap in the i-round is that coming from the exit of the axial rolls gap in the previous i-1 round whereas that entering the axial rolls gap in the i-round is that coming from the mandrel-main roll gap in the same i-round.

As first estimation, also the strains in the radial and axial directions can be estimated by utilizing a similar formulation of that used in (96) or (97), resulting in (100) and (101).

$$\hat{\varepsilon}_{s,j,i,M} = \ln\left[\left(\frac{s_{j,i,LF,M} + s_{j,i,RF,M}}{2}\right)\frac{1}{s_{j,0}}\right] \tag{100}$$

$$\hat{\varepsilon}_{z,j,i,A} = \ln\left[\left(\frac{h_{j,i,LF,A} + h_{j,i,RF,A}}{2}\right)\frac{1}{h_{j,i}}\right] \tag{101}$$

As mentioned before, the strains estimated by (100) and (101) are not consistent due to the fact that ignore the spreading effect but are the basis for the more precise estimation of the strain along these directions. In addition to that, since no strains due to the spreading effect are taken into account the strain along the radial direction is only caused by the motion of the mandrel in the relevant deformation gap. Eq. (100), as well as that along the vertical direction is only caused by the motion of the upper axial roll in the relevant deformation gap, Eq. (101).

Defining, once again, the round-based incremental strains for the radial and axial directions it results in (102) and (103), those are based on the estimations made by utilizing (100) and (101) for two consecutive rounds, respectively.

$$d\hat{\varepsilon}_{s,j,i,M} = \hat{\varepsilon}_{s,j,i,M} - \hat{\varepsilon}_{s,j,i-1,M} \tag{102}$$

$$d\hat{\varepsilon}_{z,j,i,A} = \hat{\varepsilon}_{z,j,i,A} - \hat{\varepsilon}_{z,j,i-1,A} \tag{103}$$

However, comparing the incremental circumferential strain (98) with the theoretical incremental strain in the radial direction calculated by (102) at the mandrel–main roll gap they result in different absolute values, as it will be shown in the result section, and an incremental strain in the third direction (vertical direction) should be introduced in order to fulfill the volume constancy principle, the first invariant of strain tensor is equal to 0, which is a direct consequence of it, resulting in Eq. (104).

$$d\varepsilon_{z,j,i,M} = -\left(d\varepsilon_{c,j,i,M} + d\hat{\varepsilon}_{s,j,i,M}\right) \tag{104}$$

In the same way, comparing the incremental circumferential strain (99) with the incremental strain in the vertical direction calculated by (103) at the axial rolls gap, they result in different absolute values, and an incremental strain in the third direction (radial direction) should be introduced according to (105).

$$d\varepsilon_{s,j,i,A} = -\left(d\varepsilon_{c,j,i,A} + d\hat{\varepsilon}_{z,j,i,A}\right) \tag{105}$$

After the j-slice has passed through the mandrel–main roll gap, where the incremental strain in the third direction (the vertical one) $d\varepsilon_{z,i,j,M}$ is calculated by (104), the slice should pass through the axial rolls gap, where the initial estimation of strain in the vertical direction $d\hat{\varepsilon}_{z,i,j,A}$ calculated by (103) should be corrected by adding $-d\varepsilon_{z,i,j,M}$. Therefore, the incremental strain in the vertical direction at the axial rolls gap is the combination of theoretical strain, calculated at the i-round in the axial rolls gap (103), and the third strain (vertical strain) calculated, at the i-round, in the mandrel–main roll gap (104), as shown in (106).

$$d\varepsilon_{z,j,i,A} = d\hat{\varepsilon}_{z,j,i,A} - d\varepsilon_{z,j,i,M} \tag{106}$$

After the j-slice has passed through the axial rolls gap, where a third strain is introduced in the radial direction, the slice should pass through the mandrel–main roll gap, where the initial estimation of strain in the radial direction calculated by (102) should be corrected adding $-d\varepsilon_{s,i-1,j,A}$. Therefore, the incremental strain in the radial direction at the mandrel main roll gap is the combination of theoretical strain (102), calculated at the i-round in the mandrel-main roll gap, and the third strain (radial strain) calculated, at the i-1 round in the axial rolls gap (105), as shown in (107).

$$d\varepsilon_{z,j,i,A} = d\hat{\varepsilon}_{z,j,i,A} - d\varepsilon_{z,j,i,M} \tag{107}$$

Therefore, for each round of the process and for both deformation gaps the principle strain tensor can be estimated. Since the considered coordinate system is oriented along the principal directions, no rotations are required, resulting in Eq. (108), for the strain matrix after the mandrel-main roll deformation gap, and in Eq. (109) for the strain matrix after the axial rolls deformation gap.

$$d\varepsilon_{j,i,M} = \begin{bmatrix} d\varepsilon_{c,j,i,M} & 0 & 0 \\ 0 & d\varepsilon_{s,j,i,M} & 0 \\ 0 & 0 & d\varepsilon_{z,j,i,M} \end{bmatrix} \tag{108}$$

$$d\varepsilon_{j,i,A} = \begin{bmatrix} d\varepsilon_{c,j,i,A} & 0 & 0 \\ 0 & d\varepsilon_{s,j,i,A} & 0 \\ 0 & 0 & d\varepsilon_{z,j,i,A} \end{bmatrix} \tag{109}$$

By summing together all the contributions along each direction, for a considered round of the process, the finite values for the circumferential, the radial and the vertical strains in the ring can be estimated as

shown in Eq. (110), (111) and (112), respectively. The summation counter for the second term, k=0.5, accounts for the fact that the deformation in the axial rolls gap starts half round after that in the mandrel-main roll gap.

$$\varepsilon_c = \varepsilon_1 = \sum_{k=0}^{i} d\varepsilon_{c,j,i,M} + \sum_{k=0.5}^{i} d\varepsilon_{c,j,i,A} \tag{110}$$

$$\varepsilon_s = \varepsilon_2 = \sum_{k=0}^{i} d\varepsilon_{s,j,i,M} + \sum_{k=0.5}^{i} d\varepsilon_{s,j,i,A} \tag{111}$$

$$\varepsilon_z = \varepsilon_3 = \sum_{k=0}^{i} d\varepsilon_{z,j,i,M} + \sum_{k=0.5}^{i} d\varepsilon_{z,j,i,A} \tag{112}$$

In conclusion, by utilizing the von Mises yield criterion in the strain form, the incremental equivalent plastic strain, Eq. (113), as well as the finite equivalent plastic strain, Eq. (114), for each slice and for each round of the process can be calculated.

$$d\varepsilon_{eq} = \sqrt{\frac{2}{3}\left(d\varepsilon_c{}^2 + d\varepsilon_s{}^2 + d\varepsilon_z{}^2\right)} \tag{113}$$

$$\varepsilon_{eq} = \int d\varepsilon_{eq} = \sum_{\mathrm{k=0}}^{\mathrm{i}} d\varepsilon_{eq} \tag{114}$$

As it will be shown in the result section, the good agreement between analytical and numerical results will allow proving that:

i) The estimated strains are oriented along the principal directions thanks to the choice of a convenient coordinate system;
ii) The state of plane strain should be refused and a 3D strain tensor is a right choice for a proper estimation of the strain field in the ring;
iii) By utilizing the proposed approach both the strain components and the equivalent plastic strain can be estimated almost in the real-time and with a limited error in comparison to the relevant FEM simulation.

Due to the nature of the strain and the complexity of the ring rolling process, no validations with experimental results seemed to be feasible as well as no literature contributions seems to deal with this topic thus the model validation has been done only by comparing analytical results and authors' FEM simulations results. The geometry update and strain estimation algorithms are included in Quagliato (2016).

3.5 Lumped heat transfer model

In the radial-axial ring rolling process, as well as in every metal forming process, the temperature is a key influencing factor which should be carefully accounted for, due to the large impact it can have especially on the material flow stress. Especially in hot metal forming processes, the temperature drop in the workpiece results in an increase of the material flow stress, a property directly related to the forces necessary to deform the material itself. For this reason, in order to operate a proper estimation of the flow stress of the material in hot ring rolling process, a lumped heat exchange model has been developed. As mentioned above in the introduction, this model is the only one to be ring-based and not slice-based and the reasons for this choice are hereafter explained.

In the hot radial-axial ring rolling process, due to the initial high temperature of the ring, surface oxidation is a normal and unavoidable issue which highly affects the surface temperature of the ring, both for the portion of the material which is undergoing the deformation as well as for the remaining part of the ring. During the process, the scales have the effect of isolating the real surface of the ring workpiece and, when they actually detach from it, a surface with a very high temperature, which can be close to the initial one of the ring, is suddenly exposed to the environment. The prevision of size, position and time a scale will arise is out of the feasible sight of an analytical model thus a local temperature model would be affected by huge error due to the fact that important issues like this one could not be properly accounted for. Differently, if an average temperature of the ring for each round of the rotation is estimated considering conductive, convective and radiant heat exchange between ring and tools, in the first case, and between the ring and the working environment, in the second and third case, the influence of unpredictable issues, like the scales, can be neglected allowing anyway a reasonable estimation of the ring temperature.

According to this rationale, the developed temperature estimation model is subdivided into three different sub-models those account for i) conductive heat exchange between ring and tools in the mandrel-main roll deformation gap, ii) conductive heat exchange between ring and tools in the axial rolls deformation gap and iii) mixed convective-radiant heat exchange model for the estimation of the heat transfer between the ring and the environment. The calculation flow is summarized in Fig. 25.

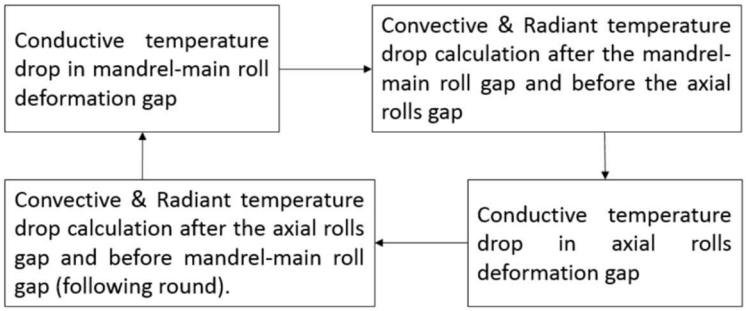

Fig. 25 – Heat transfer model calculation procedure.

In order to properly estimate the heat flow between ring and tools, especially for the calculation of the heat loss due to conduction, contact area estimation algorithms have been developed and their derivation is presented in this section of the thesis.

3.5.1 Contact geometry and heat exchange models for the mandrel-main roll gap

The contact geometry between the mandrel and the main roll with the ring and the relevant gap has been studied, in the literature, from the point of view of defining equations for the estimation of the projection of the contact arc, with the ultimate aim of calculating the process force required to deform the ring. Although the estimation of the projection of the contact arc between ring and tools allows an estimation of the relevant process force, its sole value is not enough for the calculation of the contact area between ring and tools in the mandrel-main roll deformation gap. For this reason, starting from one of the most used formulations for the estimation of the projection of the contact arc between the ring and both mandrel and main roll, a fully-analytical algorithm for the calculation of the contact area is developed. The contact area is afterward utilized, along with the contact time, to estimate the heat flow flowing from the ring to the tools as a consequence of the lower temperature of the latter ones. The formulation utilized for the estimation of the projection of the contact arc in the mandrel-main roll gap has been proposed by Hua (1997), also utilized by Qian (2009) and is reported in Eq. (115).

$$L_C = \sqrt{\frac{2\Delta s}{\frac{1}{R_S} + \frac{1}{R_M} + \frac{1}{R} - \frac{1}{r}}} \tag{115}$$

The values of R, r, $\Delta s = s_0 - s_F$, in terms $R_{j,i}$, $r_{j,i}$ and $\Delta s_{j,i}$, are known for each slice and for each round of the process, allowing to calculate the evolution of the projection of the contact arc which can be now written as $L_{C,j,i}$.

For each slice of the ring, the contact angles, measured at the center of the mandrel and of the main roll, can be estimated on the basis of the projection of the contact arc $L_{C,j,i}$ and inner or outer radius, $r_{j,i}$ and $R_{j,i}$, respectively, as reported in Eq. (116) and shown Fig. 26. The procedure will be derived for the mandrel side but it can be easily extended to the main roll side by substituting the relevant parameters.

$$\alpha_{j,i,M} = \arcsin\left(\frac{L_{c,j,i}}{r_{j,i}}\right) \tag{116}$$

For a generic j-slice of the ring, according to its circumferential size, the time t_i to rotate 360° and come back to its initial angular position can be estimated. The time t_i is not a slice-based variable anymore but it

assumes the meaning of a ring-based variable, being negligible the difference between t_i calculated by taking as references different slices.

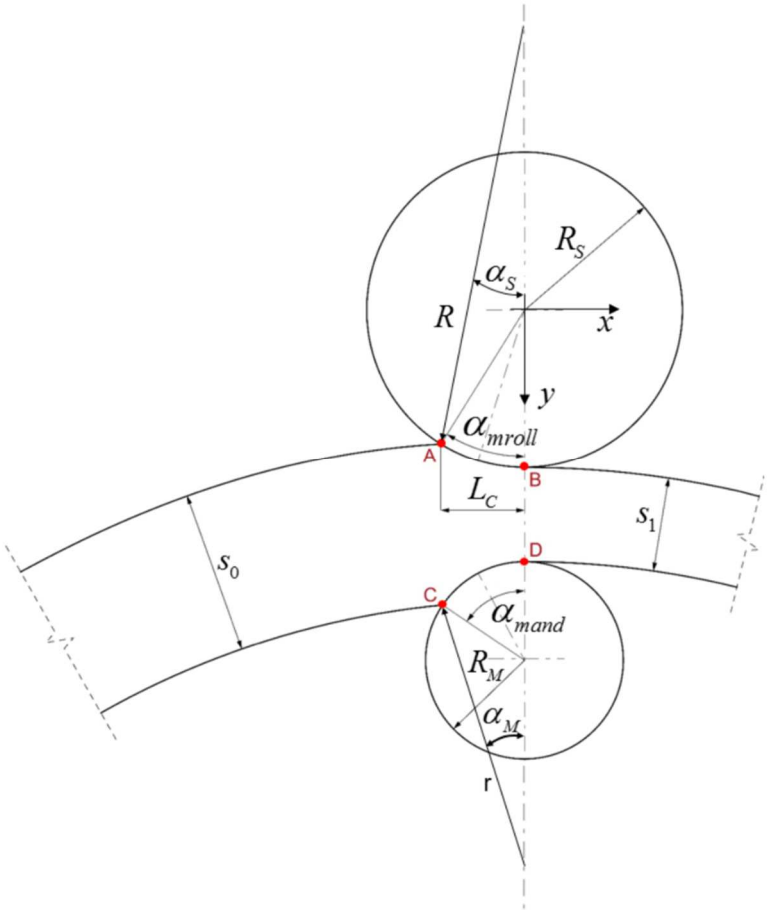

Fig. 26 – Contact geometry in the mandrel-main roll deformation gap.

Considering the gear ratio between the mandrel and the main roll, also influenced by the geometry of the ring, the contact time between the ring and the mandrel can be estimated as in (117).

$$t_{M,i} = t_i \frac{\alpha_M}{2\pi} \tag{117}$$

As it can be seen from Eq. (117), the "j" subscript is not considered anymore due to the fact that the calculation is now referred to the half round of the rotation and not to the slice anymore, as also highlighted in the block diagram of Fig. 25. Taking as reference the center of the mandrel, the relevant contact angle can be estimated, as shown in Eq. (118), referring to the radius of the mandrel and to the projection of the contact arc.

$$\alpha_{mand} = \arcsin\left(\frac{L_c}{R_M}\right) \tag{118}$$

Also in the case of Eq. (118), the values of α_{mand} can be averaged between the slices belonging to the considered half of the ring or, in order words, to the considered half round of the process.

Accordingly, the first approximation of the contact area between ring and mandrel can be estimated as shown in Eq. (119), where $\bar{h}$ represents the average height of the portion of the ring being deformed.

$$A_{mand} = \alpha_{mand} \cdot R_M \cdot \bar{h} \tag{119}$$

In order to account for the deformation happening on the inner surface of the ring, a sort of gear ratio between the inner contact area calculated on the mandrel surface and that estimated on the ring should be introduced, as detailed in (120). The numerator represents the real contact area, which accounts for the deformed geometry of the ring, whereas the denominator is the undeformed area of the ring.

$$\eta_M = \frac{A_{mand}}{A_{mand,undef}} = \frac{\alpha_{mand} \cdot R_M \cdot \bar{h}}{\alpha_M \cdot \bar{h} \cdot r} \tag{120}$$

As previously pointed out, similar derivations can be carried out for the main roll side, resulting in the calculation of the relevant parameters: α_S , α_{mroll} , A_{mroll} and η_S .

In a complete round of the ring, the total inner surface of the not deformed ring, $A_{in} = 2\pi r\bar{h}$, has been in contact with the mandrel for a time t_M whereas the total outer surface of the not deformed ring, $A_{out} = 2\pi R\bar{h}$, has been in contact with the main roll for a time t_S . Considering now the weighted product between area and time, to be used in the heat exchange equation, the contribution of both mandrel and main roll can be averaged as in (121). Eq. (121) represents the product between the average contact area and the average contact time in the mandrel-main roll deformation gap.

$$2A_{equiv,MS} \cdot t_{equiv,MS} = A_{in} \cdot t_M \cdot \eta_M + A_{out} \cdot t_S \cdot \eta_S \tag{121}$$

Inputting the result of (121) in the heat exchange equation (122) the temperature variation in the half ring can be estimated on the basis of the temperature estimated in the previous step of the calculation, T_{k-1} , the temperature of the tools T_T , considered as constant, the conduction heat transfer coefficient, HTC , the specific heat capacity of the material, C , the density of the material, ρ , and half of the volume of the ring, V .

$$T_{MS,i} = \left(T_{k-1} - T_T\right) \cdot \exp\left(\frac{2A_{equiv,MS} \cdot t_{equiv,MS} \cdot HTC}{C\rho V}\right) \tag{122}$$

As shown in Fig. 25, the calculation is carried out on the portion of the ring from the mandrel-main roll gap to the axial rolls gap thus only half of the volume of the ring is influenced by this heat exchange, in a generic i-round of the process. In conclusion, Eq. (122) allows estimating the temperature drop in the ring as a consequence of the conductive heat exchange with the mandrel and the main roll in the generic i-round.

3.5.2 Contact geometry and heat exchange models for the axial rolls gap

In principle, the contact area of a section of the ring being deformed in the axial rolls gap is not different, in shape, to one deformed in the mandrel-main roll gap, even if the size of the deformed section changes. However, in order to calculated the whole top and bottom contact area between the ring and the axial rolls, a completely different contact algorithm has been developed and is presented in this section. The need for a different algorithm, in comparison to that presented in the previous section, is given by the fact that the contact area is the result of the interaction between the conical shape of the axial rolls and the circular shape of the ring.

Firstly, in the algorithm for the estimation of the contact area in the axial rolls gap, a symmetric contribution to the height reduction is considered thus, being Δh the height reduction of a considered portion of the ring, each axial roll is assumed to operate a $\Delta h/2$, making the solution to be totally symmetric.

In addition to that, in order to simplify the calculation, the reference system is changed from the z-direction, oriented along the vertical direction of the ring, to a direction orthogonal to the central axis of the axial rolls, as shown in Fig. 27. Accordingly, Eq. (123) is derived and allows estimating the two contact radius, one on for the inner contact and one for the outer contact, Eqs. (124) and (125), respectively.

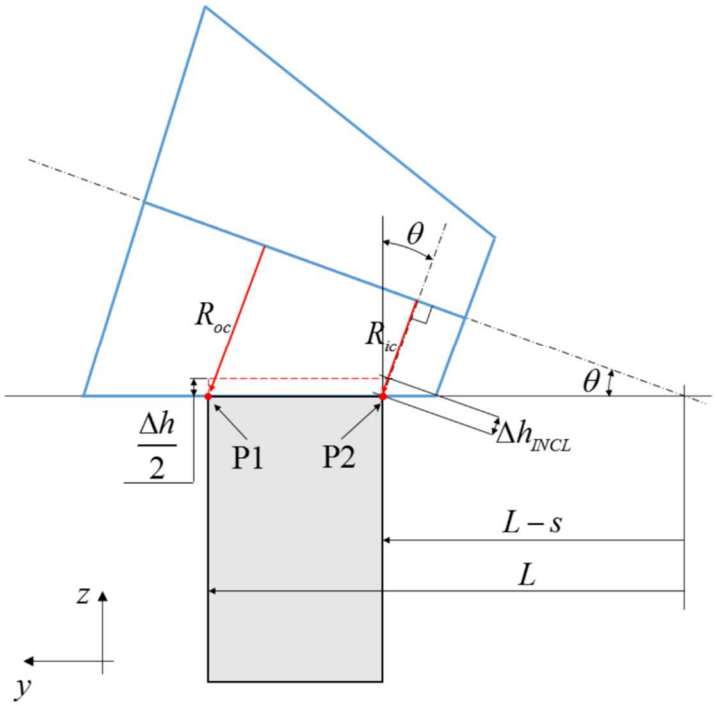

Fig. 27 – Contact geometry in the axial rolls gap, side view.

$$\Delta h_{INCL} = \frac{1}{2}\frac{\Delta h}{\cos\theta} \tag{123}$$

$$R_{ic} = \left(L - s\right)\sin\theta \tag{124}$$

$$R_{oc} = L\sin\theta \tag{125}$$

The positions of the two contact radius, R_{ic} and R_{oc}, allows defining the two contact point P1 and P2, as shown in Fig. 27, those may be constant or change during the process according to the chosen backward motion law of the axial rolls, as previously pointed out in section 3.2. If the axial rolls backward movement is set in order to follow the geometrical expansion of the ring, the initial and final distance between the virtual vertex of the axial rolls and the outer diameter is constant and equal to $L = L_0$.

Even though the contact surface between the ring and the axial rolls is, in principle, a complex shape, thanks to the small values of Δh it can be estimated on the plane orthogonal to the axis of the axial rolls and passing through P1, or P2. These cross-sections of rolls and ring operated by these two planes result in the configuration shown in Fig. 28a, relevant for the inner contact. The following procedure is derived for the inner contact surface but can be easily extended to the outer one by substituting the relevant parameters.

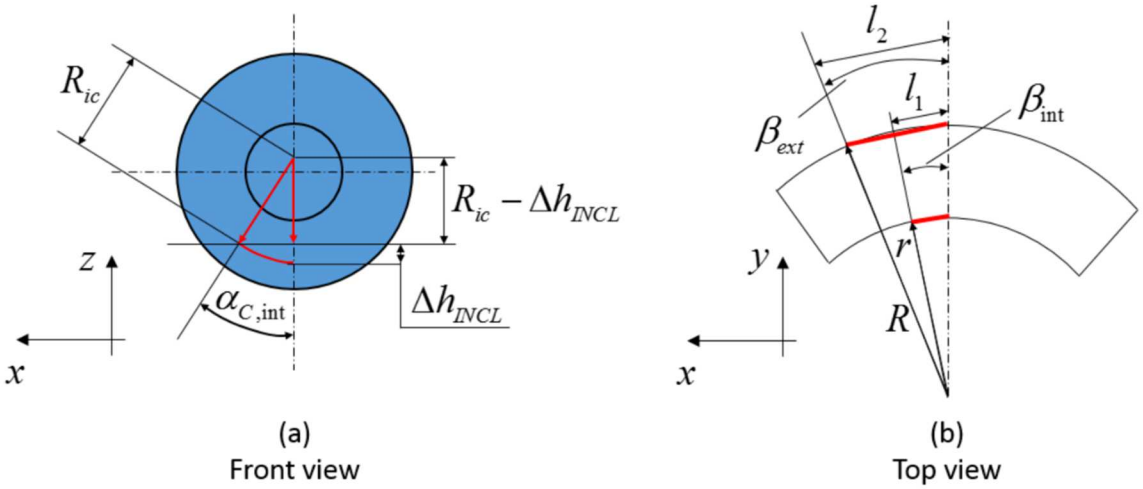

Fig. 28 – Contact geometry in the axial rolls gap, (a) front view and (b) top view.

Considering the front view, Fig. 28a, the contact angle between the onset and the exit of the deformation gap is defined as in (126).

$$\alpha_{\text{C,int}} = \arccos\left(\frac{R_{ic} - \Delta h_{INCL}}{R_{ic}}\right) \tag{126}$$

Considering now the arc relevant for the contact angle $\alpha_{\text{C,int}}$, related to the inner contact point P2, and the outer contact angle $\alpha_{C,out}$, related to the outer contact point P1, the two contact length can be estimated as well, as shown in (127).

$$l_1 = \alpha_{C,int} \cdot R_{ic} \quad ; \quad l_2 = \alpha_{C,out} \cdot R_{oc} \tag{127}$$

The contact angles related to these two arcs, as shown in Fig. 28b, can be calculated considering the projection of l_1 and l_2 on the x-y plane, resulting in Eq. (128) where r and R represent the inner and the outer radius of the ring section being deformed.

$$\beta_{\text{int}} = \frac{\alpha_{C,\text{int}} \cdot R_{ic}}{r} \quad ; \quad \beta_{out} = \frac{\alpha_{C,\text{out}} \cdot R_{oc}}{R} \tag{128}$$

Accordingly, the summation of the products between the contact angles, namely β_{int} and β_{out}, with the inner and outer radius of the portion of the ring undergoing the deformation, namely r and R, returns the total contact length which can be multiplied by the average thickness of the ring, $\overline{s}$, resulting in the first approximation of the contact area between ring and axial rolls, Eq. (129).

$$A_A = \left(\beta_{\text{int}} \cdot r + \beta_{out} \cdot R\right) \cdot \frac{\overline{s}}{2} \tag{129}$$

The gear ratio between the contact area and the undeformed top, or bottom, surface of the ring allows estimating the contact time between tools and ring in the axial rolls deformation gap, as shown in Eq. (130), where t_i is the time for the completion of the generic i-round of the process.

$$t_A = t_i \frac{A_C}{\pi \frac{R^2 - r^2}{2}} \tag{130}$$

However, in the ring rolling process, thickness and height of the ring vary according to parabolic laws, as defined in Berti and Quagliato (2015) thus, in order to properly calculate the contact area, the utilization of a linear function to describe their time-based behavior is too rough. In addition to that, since the values of thickness and height are utilized for the calculation of inner and outer radius, this consideration is also extended to these other two parameters. According to this statement, a better estimation for these geometrical data can be obtained by adopting a parabolic variation between the beginning and the end of the considered slice (a second order relationship is a reasonable approximation of a portion of a circumference), assuring the continuity of the first derivative at the transition between slices. The values of $R_{med,par}$ and $r_{med,par}$ used in Eq. (131) are calculated considering the values of the outer, and the inner, radius of pairs of consecutive slices for the half of the ring exiting the axial rolls gap to the onset of the mandrel-main roll gap, thus for the second half of the ring.

$$A_{equiv,A} = 2\left[\frac{\pi}{2} \cdot \left(R_{med,par}{}^2 - r_{med,par}{}^2\right)\right] \tag{131}$$

The factor "2" in Eq. (131) takes into account that both top and bottom surfaces of the ring are simultaneously in contact with both upper and lower axial rolls.

Based on the knowledge of the contact time and the contact area between the ring and the axial rolls for the considered i-round of the process, the heat exchange equations (132) presents a similar structure to that of Eq. (122) where the parameters relevant for the axial rolls gap contact are utilized instead.

$$T_{axial,i} = \left(T_{k-1} - T_T\right) \cdot \exp\left(\frac{2A_{equiv,A} \cdot t_A \cdot HTC}{C\rho V}\right) \tag{132}$$

This last results, summarized in Eq. (132), allows calculating the temperature of the half ring exiting from the axial rolls gap as a consequence of the conductive heat exchange between ring and tools. Once again the subscript "k" is a counter of the half rounds of the process. In addition to that, the definition of the parameters T_T, C, ρ, HTC and V is the same detailed after Eq. (122).

3.5.3 Mixed convective-radiant heat exchange model

During the radial-axial ring rolling process, especially if it is carried out at high temperature, the ring thermodynamically interacts with the surrounding environment by releasing heat through convective and radiant heat exchange modalities. This should be accounted for if a precise estimation of the temperature drop is meant to be achieved. To this aim, Newton's and radiation laws have been considered in the mixed convective-radiant heat exchange model, which combines both contributions in a single final equation, as it will be shown.

The combined convective-radiant heat losses are considered to arise when a generic slice of the ring is rigidly rotating from the mandrel-main roll gap to the axial rolls gap or from the axial rolls gap to the mandrel-main roll gap, assuming a ring rotating clockwise. Accordingly, the model presented in this section of the thesis is applied two times for each round of the process.

Considering the working environment to be largely greater than the ring, its temperature T_{amb} can be assumed to be constant, an assumption which is not far from the reality. Considering the average temperature of half ring coming from one of the above-mentioned two deformation gaps, namely $T_{k-1,i}$, the heat flow between the ring and the environment, due to convective and radiant heat exchange is estimated by equations (133) and (134), respectively. Both equations can be easily integrated over the total time for one round of the process, namely t_i.

$$\left.\frac{dQ}{dt}\right|_{conv} = A \cdot HTC_{conv}\left(T_{k-1,i} - T_{amb}\right) \tag{133}$$

$$\left.\frac{dQ}{dt}\right|_{rad} = \varepsilon \cdot \sigma \cdot A \cdot \left(T_{k-1,i}{}^4 - T_{amb}{}^4\right) \tag{134}$$

Since both models considered to whole outside area of the ring, the heat transfer coefficients can be summed up, allowing to define one single equation which accounts for the convective and radiant heat loss for a considered half portion of the ring, as shown in Eq. (135).

$$HTC_{equiv} = HTC_{conv} + \varepsilon\sigma \cdot \left(T_{k-1,i} + T_{amb}\right)\left(T_{k-1,i}^{\ 2} + T_{amb}^{\ 2}\right) \tag{135}$$

Finally, the temperature of the ring after the heat loss due to convective and radiant heat exchange in the considered half of the generic i-round of the process can be estimated by means of Eq. (136).

$$T_{C-R,k,\mathrm{i}} = T_{amb} + \left(T_{k-1,i} - T_{amb}\right)\exp\left[\left(-\frac{A \cdot HTC_{equiv}}{C\rho V}\right)t_i\right] \tag{136}$$

3.5.4 Combined utilization of the heat exchange models

In order to better clarify the procedure through which the average temperature of the ring is estimated for each half round of the process, the following explanation is reported.

At the beginning of the process, the ring is considered to have a uniform temperature $T_{k,i}$, where $k = i = 0$, since the process has not started yet. Once the process has started, considering the generic slice at the right of the mandrel-main roll deformation gap, it will rotate from this first deformation gap to the axial rolls gap, namely for 180°. During this rigid rotation, the slice exchanges heat with the surrounding environment, thus the model presented in section 3.5.3 is utilized and a first temperature loss is estimated. Afterwards, the slice enters the axial rolls deformation gap and the conductive heat exchange model presented in section 3.5.2 is utilized to estimate the consequent heat loss. The input temperature for this second stage is not the original of the ring but that resulting from the previous stage, where the mixed convective-radiant heat exchange model was utilized.

After this second stage, by considering as input temperature that calculated in the second stage, the mixed convective-radiant heat exchange model is applied once again, considering, this time, the temperature loss in the transit from the exit of the axial rolls gap to the onset of the mandrel-main roll gap. Finally, the conductive heat exchange model presented in section 3.5.1 is applied, allowing to estimate the final average temperature for the ring in the considered i-round of the process.

Thanks to the recursive procedure, the average temperature of the ring for each half round of the rotation can be estimated. This fact allows estimating the average temperature of the material undergoing the deformation, which is one of the most important parameters for the calculation of the flow stress of the material, presented in the following paragraph of the thesis.

These lumped heat exchange models offer an estimation of the average temperature of the ring at each half rotation of the ring and they neglect any distribution of temperature inside the ring, any heat flow from

the ring core to the outer surface of ring or circumferential heat flow from hot slices to cool slices, as well as any internal heating due to plastic deformation and friction, being these instantaneous phenomena limited to a very small portion of the ring.

3.6 Analytical estimation of strain rate and material flow stress

In the previous section 3.4 and 3.5, an analytical model for the estimation of the strain and of the temperature have been described and their reliability will be proven in the result section where their results will be compared with those of the relevant numerical simulations.

Based on the information calculated by utilizing these two models the last parameter required for the analytical estimation of the flow stress of the material, namely the strain rate, can also be estimated. The values of the strain, for each j-slice and for each round of the process, are known based on the strain estimation algorithm, section 3.3, whereas the average temperature of the ring, for each half round of the rotation, can be calculated by means of the model presented in section 3.5.4 In addition to that, in section 3.5.4, also the equations for the estimation of the contact time between ring and tools, for both deformation gaps, have been presented. Accordingly, the ratio between the equivalent plastic strain and the contact time, for both deformation gaps, allows calculating the strain rate in the material during the process, Eq. (137).

In principle, also the strain rate could be estimated for each slice and for each round of the process but, since the temperature model estimates only one average temperature for the ring for each half round of the process, both strain rate and flow stress have been calculated according to this half round-based subdivision.

$$\dot{\varepsilon}_{M,i} = \frac{\varepsilon_{eq,M,i}}{t_{M,i}} \quad ; \quad \dot{\varepsilon}_{A,i} = \frac{\varepsilon_{eq,A,i}}{t_{A,i}} \tag{137}$$

The contact times $t_{M,i}$ and $t_{A,i}$ are defined on the basis of the contact algorithm presented in previous sections 3.5.2 and 3.5.3, respectively, and are related to the mandrel-main roll gap and to the axial rolls, respectively. The combined utilization of the half round-based information of strain, strain rate, and temperature allows calculating the flow stress of the material, according to a chosen flow stress model.

The research presented in this thesis has been almost all carried out on hot ring rolling process and, for the estimation of the flow stress of the material, the Hansel-Spittel model (Hansel 1978, Opela 2015), Eq. (138), has been utilized.

$$\sigma_{fl} = C_1 e^{(C_2 \cdot T)} \varepsilon^{(n_1 \cdot T + n_2)} e^{\left(\frac{L_1 \cdot T + L_2}{\varepsilon}\right)} \dot{\varepsilon}^{(m_1 \cdot T + m_2)} \tag{138}$$

One of the main advantages of the flow stress model of Eq. (138) is given by the fact that it considered the reciprocal influence of strain and temperature thus its utilization allows a precise estimation of the flow stress of the material, especially in case of high temperature and highly-plastic deformations.

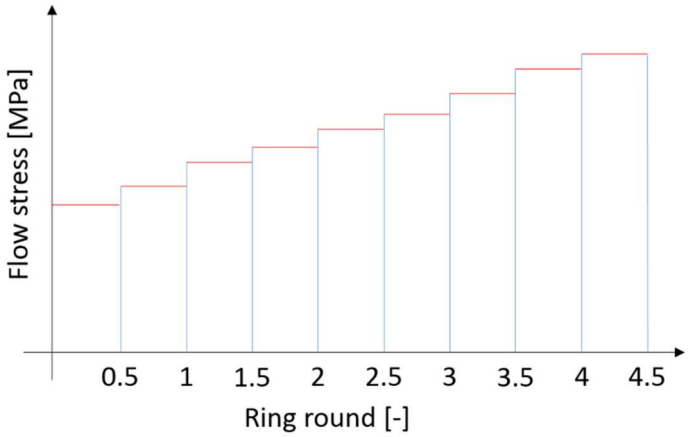

Fig. 29 – Flow stress update concept.

For each half round of the process, the flow stress of the material is estimated according to Eq. (138) and the data are stored and utilized, as it will be shown in the following section of the thesis, for the calculation of the process forces in the two deformation gaps. The shape of the progressive calculation of the flow stress, for increasing rounds of the process, is shown in Fig. 29.

For each round of the rotation, the material is considered to have a perfect plastic behavior, which allows directly utilizing the material flow stress for the calculation of the yield stress and of the yield shear stress, the last one according to the von Mises yield criterion, as shown in Fig. 30.

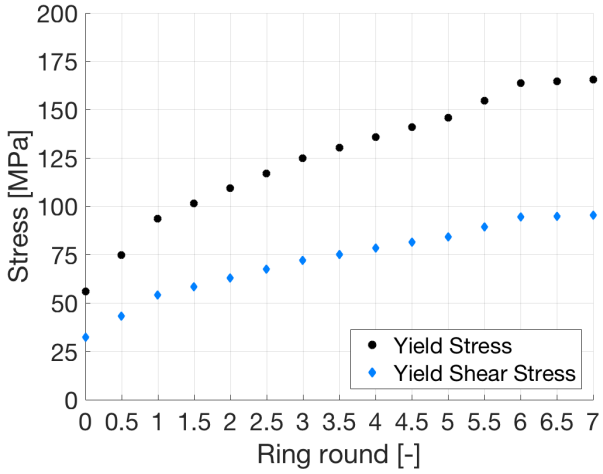

Fig. 30 – Yield strength and yield

The values shown in Fig. 30 are taken from one of the analyzed study cases but are reported only in terms of exemplification of how the results of the proposed algorithm look like.

In the following, and last, section of chapter 3, the developed slip line based generalized force model is presented and the values of both geometry of the ring and flow stress will be utilized for the estimation of the process forces, both in the mandrel-main roll and in the axial rolls deformation gap.

Both the lumped heat transfer model as well as the analytical estimation of the flow stress of the material are contained in Quagliato (2017).

3.7 Generalized slip line-based force model

The estimation of the process forces in the ring rolling process has always been one of the most important topics researched by investigators, mainly due to its high importance in the industry. For this reason, as summarized in the literature survey section, several authors focused on the development of analytical models for the prediction of the process forces according to a chosen set of process parameters. However, as also previously highlighted, the developed models either show an intrinsic unreliability due to too strict or not realistic assumptions or have proven to be accurate only on specific ranges of ring dimensions.

For these reasons, a new force model based on the slip line theory has been developed and, thanks to a generalized contact geometry algorithm, which can be adapted both to the mandrel-main roll gap and to the axial rolls gap, the proposed approach can be utilized for the estimation of both process forces only by changing the geometrical inputs and the relevant boundary conditions.

In this last section of chapter 3, both the mathematical background of the slip line method and the recursive algorithm through which to construct the slip line field will be presented, aiming to give a full perspective of the developed approach.

3.7.1 Introduction to the method

In a state of plane strain, slip lines are defined as the directions of maximum shear strain rate or, in other words, the direction along which the material plastically flows during the deformations, Hill (1950). Starting from the definition of the boundary conditions on specific points where the stress field is known, the pressure distribution can be calculated on the overall slip line field, allowing to derive the relevant pressure distribution. On the basis of the pressure distribution, also the process force can be calculated.

The theory of the slip lines is based on two main assumptions, namely the consideration of a perfect plastic material and of a state of plane strain, those are normally not the case of the ring rolling process.

However, both issues can be resolved by taking into account for the following considerations. First of all, although the plane strain assumption has shown not to be fulfilled in the ring rolling process, ref. section 3.4, the consideration of a plane strain condition only for the estimation of the process forces does not introduce a large error in the calculation. In fact, in the developed algorithm, the calculation of the flow stress is based on the estimation of the equivalent plastic strain, which in turn is estimated on the basis of a 3D strain tensor. This fact allows accounting for the 3D nature of the strain, by means of the estimation of the flow stress, while it allows fulfilling the assumption of the slip line method. In the proposed slip line-

based model, the slip line field will be constructed on a 2D plane, considering the main plastic deformation to occur along the movement direction of the tools, namely mandrel and upper axial roll, with a deformation field expanding along to circumferential direction of the ring.

Concerning the second assumption of the slip line method, the consideration of a perfect plastic material is an assumption already introduced in the approach, as highlighted in the previous section of the thesis. In fact, the proposed approach considers the material to have a perfect plastic behavior, whose yield stress value is updated on a half round basis.

On the basis of these considerations, the utilization of the slip line method for the estimation of the process forces in the ring rolling process seems to be consistent and, as it will be shown in the result section, the application of the proposed approach allows estimating both radial and axial forming force with a limited and reasonable error in comparison to both experimental and numerical results.

3.7.2 Slip line method theoretical background

Considering a generic portion of the plastically deformed material, as shown in Fig. 31a, it will be bounded by two pairs of slip lines, those always cross themselves with an $\pi/2$ angle. The counterclockwise angle between the tangent to the α-line, in a considered point of the network, and the x-axis is defined as ϑ . For a generic portion of material enclosed by two-pairs of slip lines, Fig. 31a, the relevant Mohr circle, under plane strain conditions, is defined as in Fig. 31b and, accordingly, the two stress and the shear stress components can be written as in Eq. (139)-(141), where $\bar{\sigma}$, k and 2ϑ represent the hydrostatic pressure, the yield shear strength of the material and the angle between the stress vector and the pure shear direction in the Mohr plane, respectively.

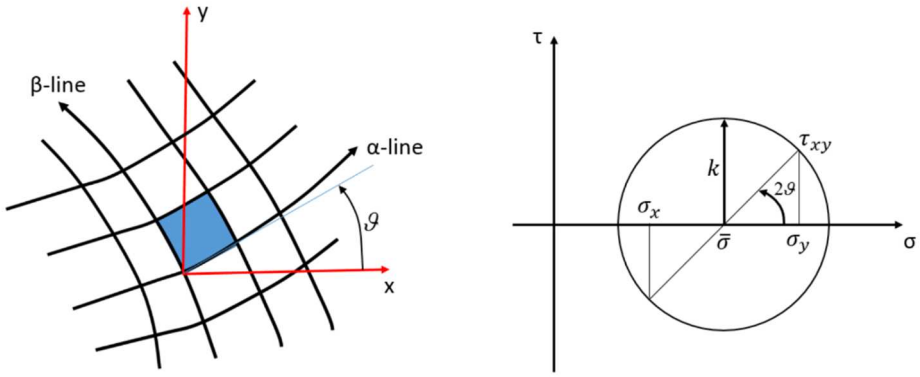

Fig. 31 – (a) Generic portion of material enclosed in a slip line network and (b) relevant Mohr circle.

$$\sigma_x = -\bar{\sigma} - k \sin 2\vartheta \tag{139}$$

$$\sigma_y = -\bar{\sigma} + k \sin 2\vartheta \tag{140}$$

$$\tau_{xy} = k \cos 2\vartheta \tag{141}$$

In case of plane strain condition, the von Mises yield criterion is reduced to the form shown in Eq. (142) where Y represents the yield stress of the material under uniaxial tension.

$$\frac{Y}{\sqrt{3}} = \frac{1}{4}\left(\sigma_x - \sigma_{xy}\right)^2 + {\tau_{xy}}^2 = k^2 \tag{142}$$

By neglecting the contribution of the internal forces, the differential equilibrium equation is reduced to $\nabla \sigma_{i,j} = 0$. Considering the two directions on the slip line plane, namely x- and y-direction, it results in equilibrium Eqs. (143) and (144).

$$\frac{\partial \sigma_x}{\partial x} + \frac{\partial \tau_{xy}}{\partial y} = 0 \tag{143}$$

$$\frac{\partial \sigma_y}{\partial y} + \frac{\partial \tau_{xy}}{\partial x} = 0 \tag{144}$$

In addition to that, by neglecting the elastic contribution to the deformation, the volume constancy principle defined in terms of infinitesimal displacements is defined according to (145), where u_x represents the infinitesimal displacement along the x-direction whereas u_y that along the y-direction.

$$\frac{\partial u_x}{\partial x} + \frac{\partial u_y}{\partial y} = 0 \tag{145}$$

From the equilibrium equations (144), it can be immediately verified that in case the stress components along the x-direction and the y-direction are equal, their first-order partial derivate, along with their relevant directions, x-direction for σ_x and y-direction for σ_y, are both equal to zero. Substituting the stress state equations (139)-(141) into $\partial \sigma_x / \partial x = \partial \sigma_y / \partial y = 0$ and considering the direction where the tangent of the α-line and the β-line coincide with x- and y-axis, namely $\vartheta = 0$, it is possible to define a relationship between the variation of the hydrostatic pressure, namely $\bar{\sigma}$, and the angle of the stress vector in the Mohr plane, namely ϑ, as in (146), for the α-line, and in (147), for the β-line.

$$\frac{\partial \sigma_x}{\partial x} = 0 \quad \Rightarrow \quad \frac{\partial \bar{\sigma}}{\partial x} + 2k \frac{\partial \vartheta}{\partial x} = 0 \tag{146}$$

$$\frac{\partial \sigma_y}{\partial y} = 0 \quad \Rightarrow \quad \frac{\partial \bar{\sigma}}{\partial y} - 2k \frac{\partial \vartheta}{\partial y} = 0 \tag{147}$$

Integrating Eqs. (146) and (147) the so-called Hencky's equations are derived, Eqs. (148) and (149), defining the equilibrium equations on the slip line network. The meaning of the Hencky's equations and

that of previous equilibrium equation (143) and (144) are equal, but the first ones are defined for the slip line network whereas the second one for the whole plastically deformed material.

$$\bar{\sigma} - 2k\vartheta = \text{constant on an } \alpha\text{-line} \tag{148}$$

$$\bar{\sigma} + 2k\vartheta = \text{constant on an } \beta\text{-line} \tag{149}$$

As previously anticipated, once the stress state is fully known at one point of the slip line field domain, by means of the Hencky's equations (148) and (149), it can be calculated on the overall slip line field, allowing to define the state of stress in the plastically deformed region of the material.

3.7.3 Slip line field construction algorithm

As shown in previous Fig. 7, the deformation pattern of a generic cross-section of the ring when it passes either through the mandrel-main roll gap or through the axial rolls gap is, in principle, very similar and characterized by a curvilinear contact arc on both sides. Even though the sizes of the rolls are different, by changing the geometrical boundary conditions on the contact zone a generalized and unique algorithm for the construction of the slip line field can be utilized. The developed algorithm, presented in this section, is an improvement of the original one defined by Hill (1950) for the case of a flat punch indenting on a flat surface, Fig. 10, and summarized in previous section 2.1.3.

For a more clear understanding of the steps by which the slip line field is constructed, the representation of a slip line field similar to the field resulting from the algorithm described in this section of the thesis is shown in Fig. 32.

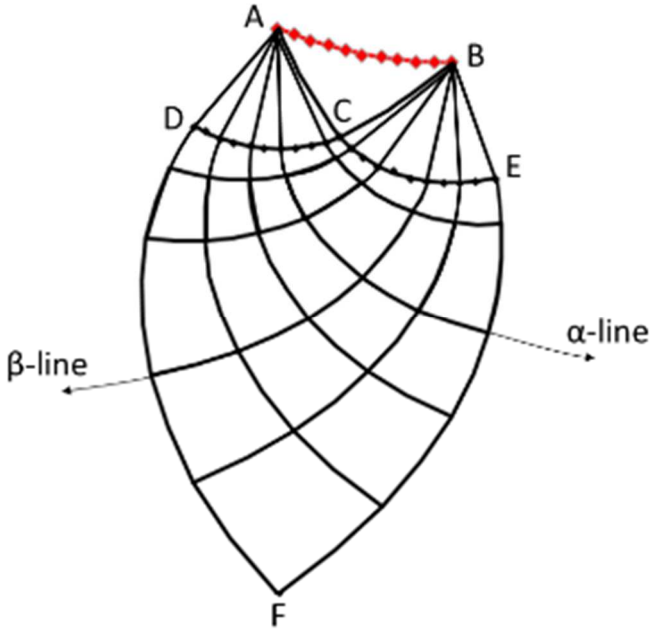

Fig. 32 – Generic representation of a slip line field with a curvilinear contact boundary (AB curve).

As generally recognized in the literature dealing with the construction of slip line field, among them Alexander (1955), Collins (1969) and Dewhurst (1973), the stress field solution inside the region of material ABC, the so-called dead metal zone is not known and this material rigidly rotates from the onset to the exit of the deformation. However, the solution can be calculated on the AC and BC lines on the basis of the boundary conditions on A and B. The boundary conditions on A and B should be defined in terms of hydrostatic pressure $\bar{\sigma}$ and inclination of the stress vector with the respect the 1-direction in the Mohr plane, namely ϑ .

For the creation of the dead metal zone region ABC the geometrical boundary conditions on the point A and B, as well as their state of stress should be accounted for. Concerning the geometrical conditions, the inclination of the onset contact point A, with respect to the x-direction, which is also the reference direction for the calculation of the angle ϑ , is affected by the reciprocal size of tool and workpiece, as shown in Fig. 33.

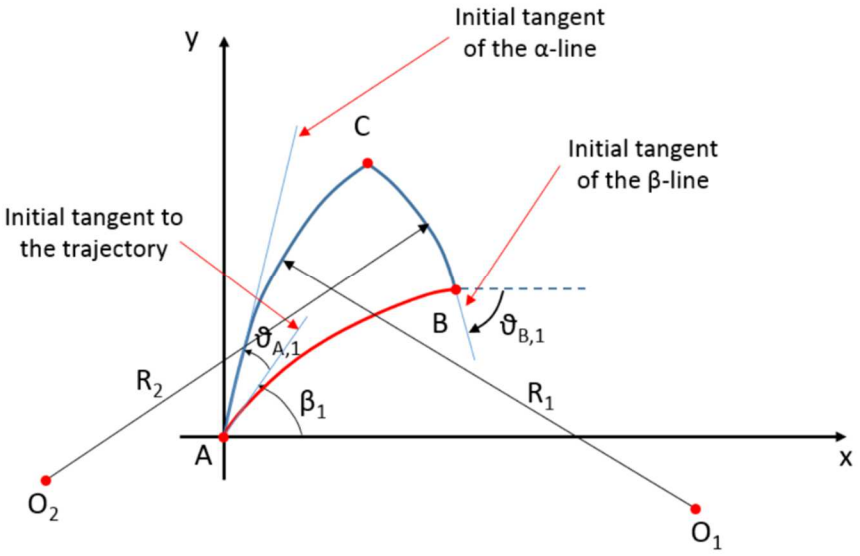

Fig. 33 – Initial construction of the slip line field, the dead metal zone.

The angle β_1 is influenced by the size of the roll acting on the workpiece as well as by the draft, either thickness or height draft, operated on the material. This higher the draft or the greater the diameter of the roll the greater the angle β_1. According to this geometrical boundary condition, the slip line starting from the point A will have an inclination of $\beta_1 + \vartheta_{A,1}$, the first one based on the above-mentioned geometrical boundary condition whereas the second one based on the stress boundary conditions.

For the point B, located at the exit of the deformation gap, since it is aligned with the center of the rolls, see Fig. 26, no β angle is defined and the inclination of the slip line starting from this point, $\vartheta_{B,1}$, only depends on the stress boundary conditions.

In order to create the triangular-like region ABC, the α-line starting from A and the β-line from B have to intersect themselves in the point C forming an $\pi/2$ angle. For this reason, each one of them can be considered as an arc of circumference starting at point A, for the α-line, and in B for β-line. The radii of these arcs are orthogonal to the line inclined, in their relevant starting point, at an $\beta_i + \vartheta_{j,i}$ angle, therefore the line where the center of arc O_i lays is determined. The subscript "i" refers to the counter for the lines starting from one point of the slip line domain, namely i=1…n, whereas "j" stands for the point name counter, namely j=A or B.

The radii of these arcs, R_1 and R_2 in Fig. 33, are unknown but they can be related to the slip lines angles $\vartheta_{A,1}$ and $\vartheta_{B,1}$ by an inverse proportionally, the wider the angle the smaller the relevant radius.

In the point C, these two arcs form a π/2 angle, which means that the triangle O_1O_2C is rectangular in O_1CO_2, with the two cathetouses having lengths equal to R_1 and R_2. In order to trace these two arcs, their relevant centers, namely O_1 and O_2, have to be determined considering that, by construction, $R_1^2 + R_2^2 = \overline{O_1O_2}^2$, and that, the following correlation is considered between radii and inclination angles, namely $R_1 / R_2 = \vartheta_{B,1} / \vartheta_{A,1}$. The coordinates of the two centers, O_1 and O_2, can be defined based on the coordinates of A and B and on the β_i and $\vartheta_{j,i}$ angles, as shown in Eqs. (150) and (151), respectively, where $\vartheta_{B,1} < 0$ angle.

$$O_1 = \begin{Bmatrix} x : A_x + R_1 \sin\left(\vartheta_{A,1} + \beta_1 + \beta_m\right) \\ y : A_y - R_1 \cos\left(\vartheta_{A,1} + \beta_1 + \beta_m\right) \end{Bmatrix} \tag{150}$$

$$O_2 = \begin{Bmatrix} x : B_x - R_2 \sin\left(\vartheta_{B,1}\right) \\ y : B_y - R_2 \cos\left(\vartheta_{B,1}\right) \end{Bmatrix} \tag{151}$$

One important consideration concerning the initial inclination of the slip line starting from A is related to the friction, which can be accounted for in terms of friction angle and which influences the stress boundary conditions on A.

Since no forces are applied on the left of point A along x-direction, point A belongs to a free edge, it results in that $\sigma_{x\_A} = \tau_{x,y\_A} = 0$. Substituting this result in (139) and (141), the first α-line, starting from A, will have an inclination angle, due to the stress boundary conditions, equal to $\vartheta_A = \pi / 4$, which results in $\bar{\sigma}_A = k$. Substituting this last result into (140) the initial stress boundary conditions on A are determined, with $\sigma_{x\_A} = \tau_{x,y\_A} = 0$ and $\sigma_{y\_A} = 2k$. In addition to that, in A, also the contribution of the β_1 angle should be added as well as the friction angle, calculated according to a chosen friction criterion. In

conclusion, the inclination of the α-line starting from A is the summation of three contributions: $\vartheta_{A,1}$ calculated according to the stress boundary conditions, β_1 resulting from the geometrical boundary conditions and β_m accounting for the friction effect. This summation of contributions is clearly visible in Eq. (150). On the point B, only the boundary conditions related to the stress state are present and allow calculating similar results to those derived for the point A.

Considering the x-y coordinates of the points A and B, defined as (A_x, A_y) and (B_x, B_y) respectively, and the above-mentioned boundary conditions for the points A and B, the only unknown quantities of the equations systems (150) and (151) are the two radii of the arc of circumference, namely R_1 and R_2. By making explicit these two variables, following equation system (152) is defined. Being a second-order polynomial equation, only the solution which satisfies $R_1 + R_2 > O_1O_2$ should be considered since the other one does not have physical meaning. The parameters P, Q, M and N in (152) are defined as reported in (153).

$$\begin{cases} R_2 = \left[2PM - 2QN \pm \sqrt{\left(2PM - 2QN\right)^2 - 4\left(N^2 + M^2\right)\left(Q^2 + P^2\right)} \right] \dfrac{1}{2\left(N^2 + M^2\right)} \\ R_1 = R_2 \dfrac{\left|\vartheta_{B,1}\right|}{\left|\vartheta_{A,1}\right|} \end{cases} \tag{152}$$

$$\begin{aligned} P &= A_y - B_y \\ Q &= A_x - B_x \\ M &= \left(\vartheta_{B,1} / \vartheta_{A,1}\right)\cos\left(\beta_1 + \vartheta_{A,1}\right) - \cos\vartheta_{B,1} \\ N &= \left(\vartheta_{B,1} / \vartheta_{A,1}\right)\sin\left(\beta_1 + \vartheta_{A,1}\right) + \sin\vartheta_{B,1} \end{aligned} \tag{153}$$

In C, the triangular shape formed by R_1 R_2 and O_1O_2 has the configuration shown in Fig. 34 thus, once the coordinates of the two centers O_1 and O_2 are known, also φ_{orig} can be calculated as in Eq. (154).

$$\varphi_{orig} = \arctan\left(\frac{O_{1,y} - O_{2,y}}{O_{1,x} - O_{2,x}}\right) \tag{154}$$

Finally, considering the geometrical relations between O_1, O_2 and C the remaining inner angle of the rectangular triangle $O_1\hat{C}O_2$ is immediately estimated (155) and, accordingly the coordinate of the point C are estimated as well (156).

$$\delta_2 = \arccos\left(\frac{R_2}{\left|O_2O_1\right|}\right) \tag{155}$$

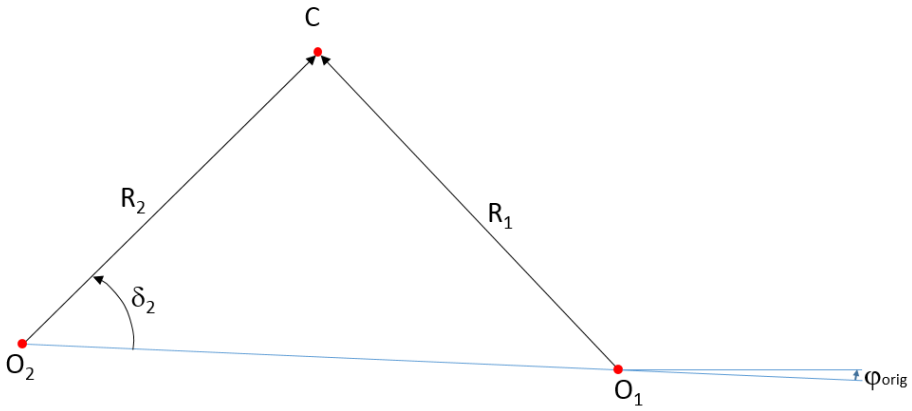

Fig. 34 – Geometrical construction of the point C, end of the dead metal zone.

$$\begin{aligned} C_x &= R_2 \cos\left(\delta_2 + \varphi_{orig}\right) + O_{2,x} \\ C_y &= R_2 \sin\left(\delta_2 + \varphi_{orig}\right) + O_{2,y} \end{aligned} \tag{156}$$

According to the derivation presented so far, the dead metal zone can be constructed according to the stress, geometrical and friction boundary conditions on the onset and at the exit points of the contact curve between ring and tools. According to this solution, the procedure how to build the remaining portions of the slip line field is hereafter detailed.

The regions of the left and on the right of the dead metal zones are defined as fans and, for the construction of these two portions of the slip line domain, an additional consideration regarding the hydrostatic pressure $\bar{\sigma}$ should be given. In the case of compressive deformation of materials, the boundary of the slip line network is defined as the border, in the plain strain-section of the ring, where the hydrostatic pressure becomes zero and afterward positive. Although the mathematical solution, according to the governing equation, can be calculated, it does not have physical meaning, since the material is undergoing a compression deformation thus no tension stresses should arise. The width of the two regions on the left and on the right of the ABC dead metal zone depends on the pressure boundary conditions between tool and workpiece which are not known a priori.

For this reason, the developed algorithm is designed in order to determine the increment of the ϑ angle that makes the relevant hydrostatic pressure to become zero and, accordingly, to subdivide into equi-spaced sub-sectors the so-determined portion of the domain, allowing to construct the two fans with a chosen discretization angle. By definition, each slip line of the domain must satisfy the Hencky's equation (148) (for a α-line) or equation (149) (for a β-line), namely meaning that the sum, with a sign, of hydrostatic pressure and the $2k\vartheta$ factor is constant along a slip line.

Considering the β-line exiting from point C and reaching a generic point D where the hydrostatic pressure vanished ($\bar{\sigma}_D = 0$), Fig. 35, this point represents the boundary between compression and tension stress solutions and only compressive solutions are considered to be physically acceptable.

Using Eq. (149) for point C and point D, the absolute angle in point D is determined as in (157), limiting the extension of the left fan.

$$\vartheta_D = \vartheta_C + \frac{\bar{\sigma}_C}{2k} \tag{157}$$

The same rationale is applied to determine the extension of the right fan by considering the condition which makes $\bar{\sigma}_E = 0$. By utilizing Eq. (148) from point C to E the absolute angular extension of the right fan is determined according to (158).

$$\vartheta_E = \vartheta_C - \frac{\bar{\sigma}_C}{2k} \tag{158}$$

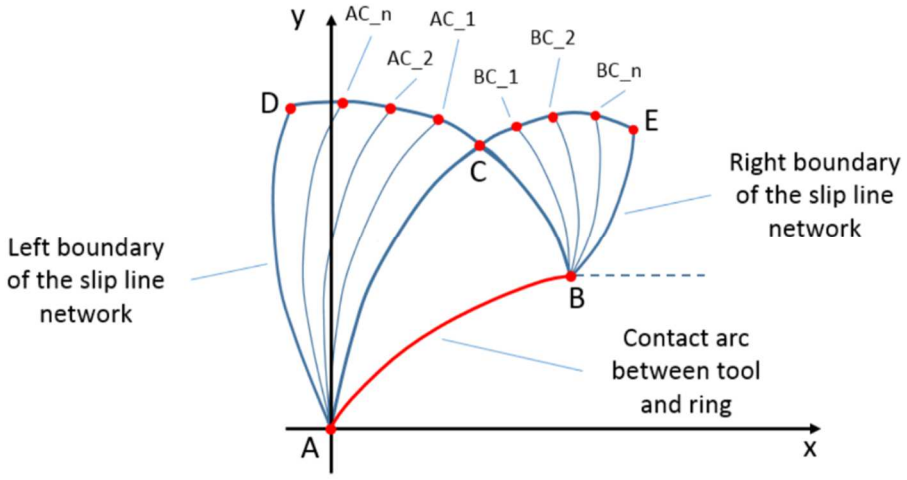

Fig. 35 – Geometrical construction of the fan regions.

In order to improve the accuracy of the calculation, a definable number of intermediate subdivisions for both left and right fans are operated, resulting in intermediate angles $\Delta\vartheta_1$ for the left fan and $\Delta\vartheta_2$ for the right fan. The number of subdivision is a choice made at the beginning of the calculation but, as also stated in Hill (1950), a 5° discretization angle allows a proper calculation of the results while it allows reducing the complexity of the calculation.

$$\Delta\vartheta_1 = \frac{\vartheta_D - \vartheta_C}{nsubdiv} \quad ; \quad \Delta\vartheta_2 = \frac{\vartheta_E - \vartheta_C}{nsubdiv} \tag{159}$$

The slip line network, for each fan, is represented by arcs centered in fan center (point A for left fan, point B for right fan) whose shape is obtained by rigid rotation around the fan center of an incremental angle calculated as in (159), for the left fan and for the right fan, respectively, as shown in Fig. 35.

The coordinates of the crossing points between α-lines and β-lines, moving from C to D (or from C to E), are determined as the final point of the vector $\hat{L}_A$ (or $\hat{L}_B$) from the center of the fan to point C, rotated around the center of the fan by the incremental angle calculated in (159).

Based on the Hencky's equations (148) and (149), also the ϑ angle and the hydrostatic pressure $\bar{\sigma}$, for all the points on the β-line from C to D and on the α-line from C to E, can be calculated. The set of equations for the left fan, related to the β-line passing through BCD, is given in (160) whereas that for the right fan, related to the α-line passing through ACE, are reported in (161).

In (160) and (161), the subscript "j" stands for the point counter and starts from j=0 in the point C to j=n in the point D and to j=-n to the point E. Finally, λ_{CD} and λ_{CE}, define the angle between the $\hat{L}_A$ and $\hat{L}_B$ vectors with respect to the horizontal axis.

$$\begin{aligned}
&\hat{L}_A = \sqrt{\left(x_C - x_A\right)^2 + \left(y_C - y_A\right)^2} \qquad ; \qquad \lambda_{AC} = \arctan\left(\frac{y_C - y_A}{x_C - x_A}\right) \\
&x_{AC_j} = \hat{L}_A \cos\left(\lambda_{AC} + j\Delta\vartheta_1\right) + x_A \\
&y_{AC_j} = \hat{L}_A \sin\left(\lambda_{AC} + j\Delta\vartheta_1\right) + y_A \\
&\vartheta(\alpha)_{AC_j} = \vartheta_j + j\Delta\vartheta_1 \\
&\bar{\sigma}_{AC_j} = \bar{\sigma}_j - j\Delta\vartheta_1 2k
\end{aligned} \tag{160}$$

$$\begin{aligned}
&\hat{L}_B = \sqrt{\left(x_C - x_B\right)^2 + \left(y_C - y_B\right)^2} \qquad ; \qquad \lambda_{BC} = \arctan\left(\frac{y_C - y_B}{x_C - x_B}\right) \\
&x_{BC_j} = x_B - \hat{L}_B \cos\left(\lambda_{BC} + j\Delta\vartheta_2\right) \\
&y_{BC_j} = y_B - \hat{L}_B \sin\left(\lambda_{BC} + j\Delta\vartheta_2\right) \\
&\vartheta(\alpha)_{BC_j} = \vartheta_j + j\Delta\vartheta_2 \\
&\bar{\sigma}_{BC_j} = \bar{\sigma}_j - j\Delta\vartheta_2 2k
\end{aligned} \tag{161}$$

At this point of the algorithm, the dead metal zone and the two fans on its left and right have been constructed. In addition to that, on the basis of the initial boundary conditions on A and B, both hydrostatic pressure and theta angle can be calculated all over the domain constructed so far.

The final part of the algorithm deals with the construction of the last portion of the slip line network, whose last point F, see Fig. 32, represents the end of the plastically deformed region of the material. To build this last portion of the network, the starting points are the two curvilinear line CD and CE and their relevant solutions, in terms of $\bar{\sigma}$ and ϑ.

One important theorem related to the Hencky's equations (148) and (149) concerns with the relationship between the ϑ of two pairs of crossing slip lines, as shown in Fig. 36.

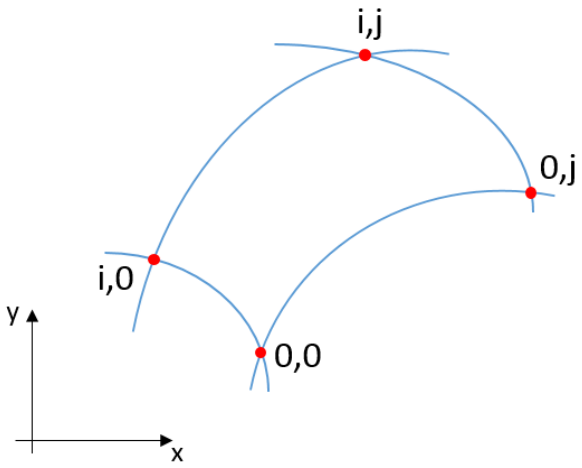

Fig. 36 – General quadrilateral element bounded by two pairs of slip lines.

By applying the Hencky's equations (148) and (149) to a generic quadrilateral element bounded by two pairs of slip lines, as shown in Fig. 36, it is possible to determine the relationship between the hydrostatic pressure on these four points, (162) and (163), as well as that between the relevant ϑ angles, as shown in Eq. (164).

$$\bar{\sigma}_{i,j} - \bar{\sigma}_{0,0} = \left(\bar{\sigma}_{i,j} - \bar{\sigma}_{i,0}\right) + \left(\bar{\sigma}_{i,0} - \bar{\sigma}_{0,0}\right) = 2k\left(2\vartheta_{i,0} - \vartheta_{i,j} - \vartheta_{0,0}\right) \tag{162}$$

$$\bar{\sigma}_{i,j} - \bar{\sigma}_{0,0} = \left(\bar{\sigma}_{i,j} - \bar{\sigma}_{0,j}\right) + \left(\bar{\sigma}_{0,j} - \bar{\sigma}_{0,0}\right) = 2k\left(\vartheta_{i,j} + \vartheta_{0,0} - 2\vartheta_{0,j}\right) \tag{163}$$

$$\vartheta_{i,j} = \vartheta_{i,0} - \vartheta_{0,0} + \vartheta_{0,j} \tag{164}$$

If the ϑ angle is known for three out of four points on two pairs of slip lines enclosing a portion of material, for instance, point (0,0), (i,0) and (0,j), that of point (i,j) can be calculate according to (164) as well as the radii, to trace the relevant α-line from i,0 and the β-line from 0,j, are determined according to Eqs. (165). In (165), $R_{\alpha-i,j}$ and $R_{\beta-i,j}$ represents the radii of the arcs, starting from i,0 and from 0,j, whose intersection allows determining point i,j.

$$R_{\alpha-i,j} = \frac{1}{\tan\left[\left(\vartheta_{i,j} + \vartheta_{i,0}\right)/2\right]} \quad ; \quad R_{\beta-i,j} = \frac{1}{\tan\left[\left(\vartheta_{i,j} + \vartheta_{0,j}\right)/2\right]} \tag{165}$$

The coordinates of the generic point i,j of the domain are calculated starting from those of the neighbor ones, as shown in Eq. (166), resulting in the slip line network for the last portion of the slip line field, as shown in Fig. 37.

$$x_{i,j} = -\left(y_{i,0} - y_{0,j} - R_{\alpha-i,j}x_{0,j} - R_{\beta-i,j}x_{i,0}\right)\frac{1}{\left(R_{\alpha-i,j} + R_{\beta-i,j}\right)}$$
$$y_{i,j} = y_{i,0} + \left(x_{i,j} - x_{i,0}\right)\tan\left(\frac{\vartheta_{i,j} + \vartheta_{i,0}}{2}\right) \quad (166)$$

The last point of the slip line network is the point F where the original two lines, namely the α-line and the β-line, degenerate in a single point which is also the end of the plastically deformed region of the material. By changing the boundary conditions on A and B, as a consequence of a higher or lower draft along the depth of the workpiece, which is valid both in the case of thickness or height draft, the endpoint F as well as the angular width of the fans will change accordingly.

The algorithm detailed in this section of the paper has been implemented in an MS Excel spreadsheet which allows a fast calculation of the stress boundary conditions those allow the two slip line fields, starting from opposite tools (rolls), to intersect each other at one point.

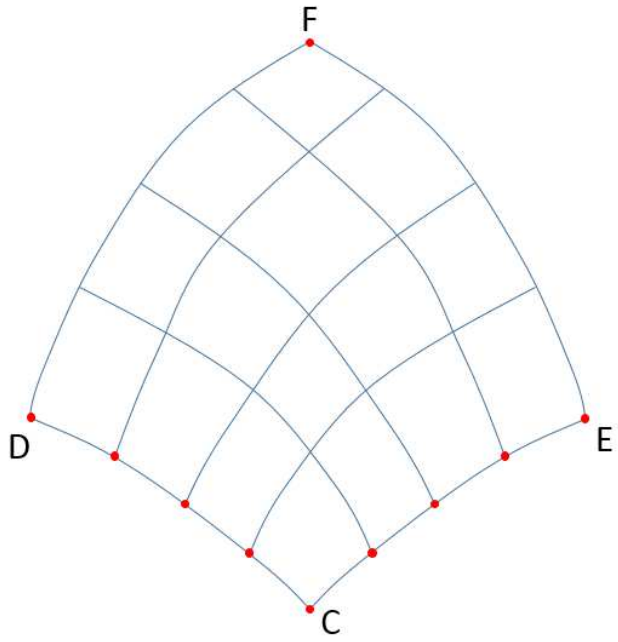

Fig. 37 – Geometrical construction of the end-region of the slip line network.

3.7.4 Calculation of the solution for the slip line field

The developed algorithm is finalized to estimate the values of pressure boundary conditions on the point A and B or A' and B', those make the two slip line fields, starting from these two contact curves, to join in one point, Fig. 38.

The ratio between the stress boundary conditions those make the two slip line fields to join at one point and those required to start the indentation, namely $2k$, is defined as pressure factor and indicated with the

symbol γ. k stands for the yield shear stress of the material under plane strain conditions and is a parameter analytically estimated by utilizing the model presented in previous section 3.6.

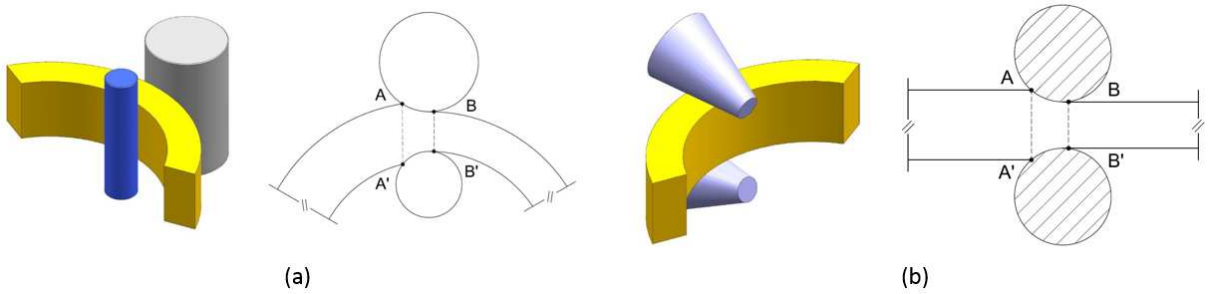

Fig. 38 – Ring deformation pattern in the (a) mandrel-main roll and (b) axial rolls deformation gap.

As shown in Fig. 39, for increasing values of the boundary conditions on A and B, set equal to those on A' and B' in force of force equilibrium along the y-direction, the two slip line fields expand both in width and depth to the point they intersect themselves, Fig. 39d.

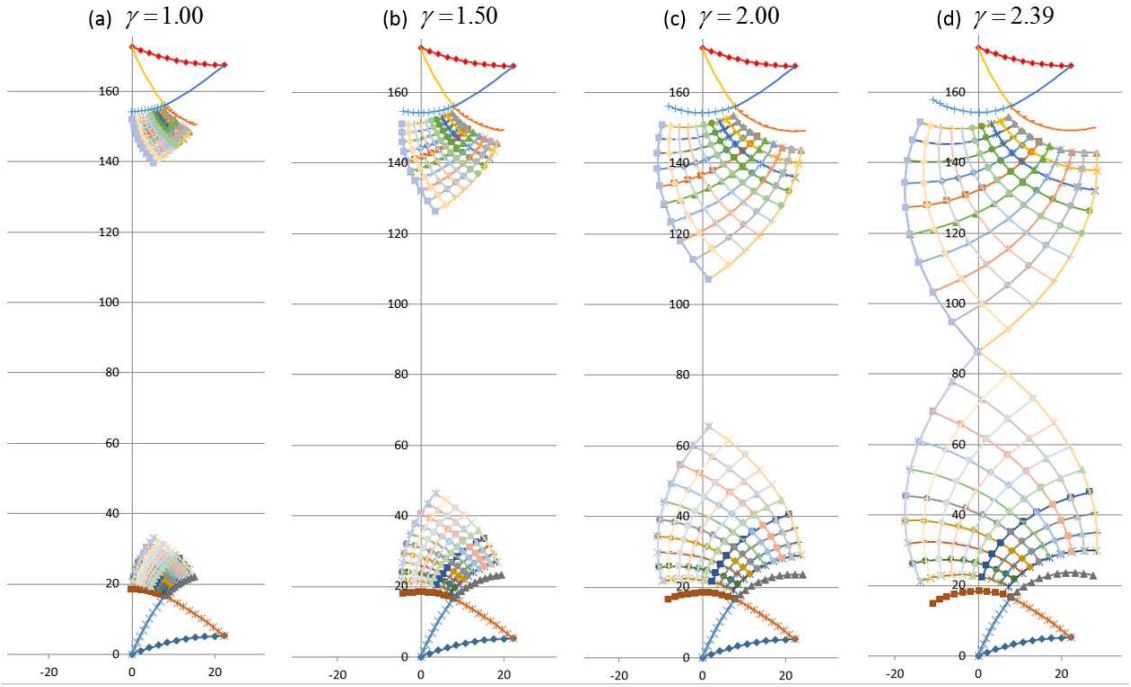

Fig. 39 – Incremental variation of the pressure factor and relevant expansion of the plastic field in the cross-section of the ring.

The value of the pressure factor γ or, in other words, of boundary conditions of A and B, which make the two slip line fields to intersect in one point is considered to be the statically determined solution for the analyzed case. The meaning of "statically determined solution" is referred to the fact that, in the proposed algorithm, no explicit verification of the admissible velocity field is carried out thus the calculation is based only on the determination of the stress field in the material in the plastically deformed region.

The algorithm presented in this section can be applied to each slice of the ring and for each round of the process, allowing a full mapping of the evolution of the process forces during the process. In addition to that, thanks to the generalized approach through which the boundary between tools and ring, namely AB and A'B' curves, have been defined, it can be utilized for the estimation of both radial and axial forming forces. The generalized force model, expressed in terms of parameters for the calculation of the radial and the axial forming forces is reported in following Eqs. (167) and (168), respectively.

$$F_{rad} = 2k\gamma\bar{s}L_{C,rad} \tag{167}$$

$$F_{axi} = 2k\gamma\bar{h}L_{C,axi} \tag{168}$$

The values of $L_{C,rad}$ and $L_{C,axi}$ are estimated by utilizing previous Eq. (115) for the first one and the average of the two values reported in Eq. (127) for the second one, respectively. The remaining parameters, namely $\bar{s}$ and $\bar{h}$, are the average thickness and height of a specific slice in the considered round of the process.

Chapter 4: Numerical analysis implementation

For the verification of the developed algorithms, numerical simulations have been carried out and have been utilized as reference especially for the cases where the laboratory experiment were not feasible, such as in the case of the strain estimation model or of the temperature model. The numerical models have been all carried out by utilizing the commercial software Simufact.Forming, from the release 12.03 to the release 14.0. One of the main advantages of Simufact.Forming is related to its well-implemented ring rolling simulation module, which allows a quick and precise setting of the ring rolling process. In addition to that, differently from other commercial software those implement the same kind of module, specific process stabilizer can be completely disabled making the numerical simulation to represent very well the reality of the process. A concept of the developed numerical model is shown in Fig. 40.

All the models have been meshed with hexahedral elements having the following dimensions: 16 mm (axial), 14 mm (radial) and 16 mm (tangential) and the mesh details are hereafter reported.

The mesh elements are three-dimensional arbitrarily distorted brick, a hexahedral eight-node isoparametric arbitrary element (Marc element type 7) associated with a 3D eight-node brick (heat transfer element) defined as an eight-node isoparametric arbitrary hexahedral element for 3D heat transfer applications (Marc element type 43). The element type 7 presents three degrees of freedom for each one of its nodes whereas the type 43 only one. Both elements use Gaussian integration for the computation of the results between their boundary points. By selecting the option “geometry” for the element type 7, it is possible to impose a constant dilatation strain to the element. This means that the eight points utilized for the Gaussian integration are used for the calculation of the deviatoric contribution of the strain whereas the centroid for the dilatation contribution. This option allows significantly improving the bending behavior of the element and helps to avoid the volumetric locking. In addition to that, element type 7 is particularly suitable for simulations where the contact is the predominant issue, such as in the case of ring-tools contact

in ring rolling. Marc element type 43 shares the same geometrical and integration features of element type 7, but it is dedicated to the heat transfer calculation during the process.

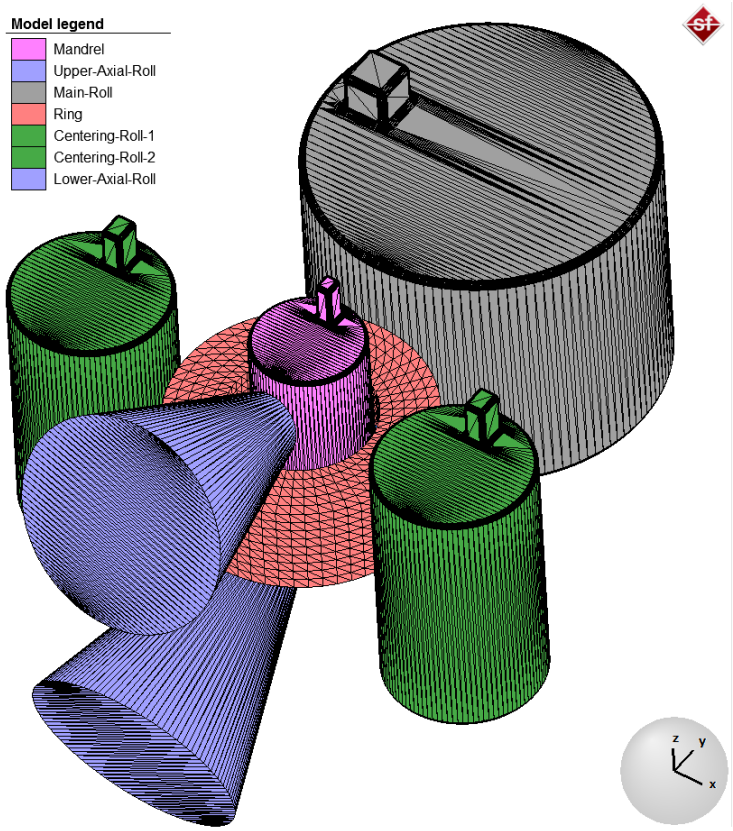

Fig. 40 – Numerical implementation of the radial-axial ring rolling process in Simufact.Forming.

All implemented numerical simulations are full thermo-mechanical explicit FE analysis, carried out considering rigid dies with heat exchange. The utilized solver for the simulation is the MUltifrontal Massively Parallel sparse direct Solver (MUMPS), especially indicated for solving systems of linear equations of the form A*x = b, where A is a square sparse matrix that can be either asymmetric, symmetric positive definite, or general symmetric. MUMPS implements a direct method based on a multifrontal approach, which performs a Gaussian factorization. The kinematics of deformation is formulated according to the updated Lagrangian algorithm where the reference configuration is set at the incremental motion n+1. True (or Cauchy) stress and an energetically conjugate strain measure, namely the true strain, are used in the constitutive relationship. The updated Lagrangian approach is particularly indicated in case of large deformation, so it fits the ring rolling process.

During the contact process, a contact tolerance is associated with each surface. If a node is within the contact tolerance, it is considered to be in contact with the segment. The contact tolerance is determined as 1/20 of the smallest element size of all elements in any contact body. For a continuum element, the element size is defined as the smallest edge of the surrounding box (3D), set up in the global coordinate system and

a node separates from a body when the stress exceeds 20 MPa. Contact affects the friction and in order to overcome the discontinuity of friction when relative velocity is zero, a nonlinear arctangent smoothing function, based on the relative sliding velocity between contact bodies, was defined adopting a threshold of 0.001 mm/s for the relative velocity below which sticking is simulated. Concerning the convergence criteria, the control is performed on two different levels: i) the maximum allowed residual convergence ratio between two consecutive steps, for the nodal displacement calculation, is set to 0.25 whereas ii) it is set to 0.35 for the nodal force.

4.1 Material model

In order to limit the influencing factors in the validation process of the developed analytical models, a steel normally utilized for the manufacturing of rings by means of ring rolling process has been utilized in most of the study cases, namely the 42CrMo4 steel alloy. The material data have been acquired from the material library available in Simufact.Forming, directly originated from the MATILDA® (Material Information Link and Database Service) archive. The material properties for the 42CrMo4 steel alloy are hereafter reported in terms of flow stress equation (169) and thermal properties in Fig. 41a, 41b, and 41c.

In following Table 1, the model ranges and coefficients for the flow stress equation (169) are reported.

$$\sigma = C_1 e^{(C_2 \cdot T)} \varepsilon^{(n_1 \cdot T + n_2)} e^{\left(\frac{L_1 \cdot T + L_2}{\varepsilon}\right)} \dot{\varepsilon}^{(m_1 \cdot T + m_2)} \tag{169}$$

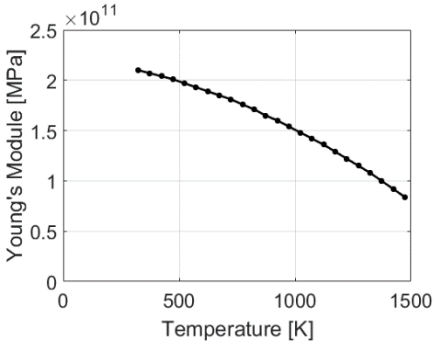

Figure 41a - Young's modulus.

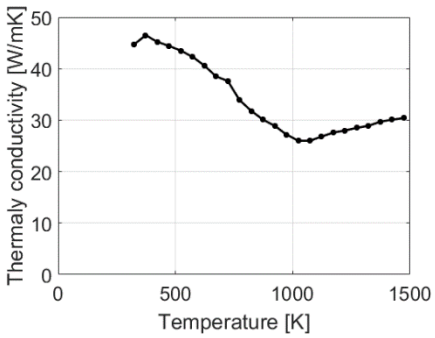

Figure 41b - Thermal conductivity.

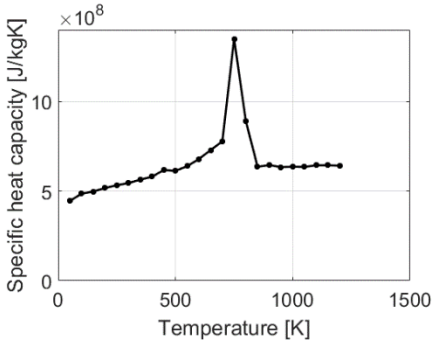

Figure 41c - Specific heat capacity.

Table 1 – 42CrMo4 alloy material model ranges and constants

Parameters	Value
Temperature range for the model [°C]	800–1250
Strain range for the model [–]	0.05–2
Strain rate range for the model [1/s]	0.01–150
C_1	5290.47
C_2	–0.0036967
n_1	–0.000334025
n_2	0.20612
L_1	–8.26584e-5
L_2	0.0289085
m_1	0.000300752
m_2	–0.156181

For the numerical simulations related to the laboratory experiments carried out with the Pb75-Sn25 soft alloy the relevant material properties, characterized by means of a compression test, have been utilized. The material characterization, as well as the resulting material properties, are presented in chapter 5 of the thesis.

4.2 Ring rolling mill and process boundary conditions

Following the same rationale of limiting the influencing factors in the validation procedure of the developed analytical models, also the dimensions of the ring rolling mill and the process boundary conditions have been set same for almost all the analyzed study cases, with the only exception of those related to laboratory experiments. In these last cases, the dimensions of the ring rolling mill utilized for the experiments have been utilized also in the numerical simulations and are summarized in the following chapter of the thesis. The dimensions of the ring rolling mill and the process boundary conditions utilized for the study cases used for the validation of the analytical models are reported in Table 2.

Table 2 – Ring rolling mill dimensions.

Parameters	Value
Radius of the main roll [mm]	325.0
Radius of the mandrel [mm]	125.0
Length of the axial rolls [mm]	595.9
Axial roll vertex angle [°]	35.0
Radius of the centering rolls [mm]	150

Concerning the process conditions, common for all the validation simulations study cases, they are reported in following Table 3.

The choice of setting the main roll rotational speed to 3 rad/s is given by the fact that this value which falls in the admissible velocity range, calculated according to Eq. (8), for all the validation study cases and is also a reasonable value in standard ring rolling processes.

Table 3 – Process general settings and boundary conditions.

Parameters	**Value**
Main roll rotational speed [rad/s]	3.0
Friction coefficient	0.3
Temperature of the environment [°C]	50
Ring initial temperature [°C]	1200
Tool temperature [°C]	150
Emissivity [-]	0.25
Heat transfer coefficient (conduction) [W/m^{2}K]	20000
Heat transfer coefficient (convection) [W/m^{2}K]	50

In all the numerical simulation study cases the number of variables has been kept as lower as possible in order to verify the influence of the variation of the most important process parameters, namely the mandrel and the upper axial roll feeding speed, on the accuracy of the different developed models, those are also the main process design choices which largely influence the process forces.

4.3 Validation study cases

The numerical simulation study cases carried out for the validation of the developed analytical models are presented in the present thesis as they have been summarized in the published papers concerning the above-mentioned topics.

Concerning the geometry estimation algorithm, presented in Berti and Quagliato (2015), the six study cases reported in Table 4, with rings ranging from 810 mm to 1800 mm as final outer diameter, have been taken into account. In Table 5, the process conditions for all the six simulation study cases are reported.

Table 4 – Geometry evolution algorithm validation cases.

	Ring1G	**Ring2G**	**Ring3G**	**Ring4G**	**Ring5G**	**Ring6G**
D_0 [mm]	552.9	660.5	607.8	698.1	1345.1	1041.9
d_0 [mm]	325.0	325.0	325.0	325.0	500.0	500.0
h_0 [mm]	143.6	110.5	233.2	149.3	469.7	231.7
D_f [mm]	809.6	810.0	1100.0	1100.0	2190.0	2180
d_f [mm]	645.0	500.0	950.0	800.0	1635.0	1800.0
h_f [mm]	120.0	90.0	200.0	100.0	345.0	128.0

Table 5 – Geometry evolution algorithm validation cases process parameters.

	Ring1G	**Ring2G**	**Ring3G**	**Ring4G**	**Ring5G**	**Ring6G**
$v_{M,0}$ [mm/s]	2.50	2.00	7.50	2.50	5.00	3.00
$v_{M,F}$ [mm/s]	2.00	1.50	5.00	2.00	2.00	1.50
$v_{A,0}$ [mm/s]	1.98	3.04	4.55	3.12	4.50	3.51
$v_{A,F}$ [mm/s]	1.37	2.58	1.88	3.00	1.64	2.23

For all the study cases reported in Table 4 the material 42CrMo4 along with the material model presented in section 4.1, have been utilized. According to the process setting algorithm detailed in section 3.1 of the paper, the ring blank dimensions shown in Table 4 have been calculated according to the final dimensions of the ring as well as the process parameters reported in Table 5 have been calculated following the procedure detailed in section 3.2. The results of the developed numerical model, for the six analyzed study cases, both in comparison with the results of the developed numerical model presented in section 3.3 as well as with the previous model available in the literature, namely Guo (2011), are discussed in chapter 6 of the thesis.

Concerning the validation of the strain estimation algorithm, previously presented in section 3.4, the validation has been carried out by applying the developed model to rings having all the same final outer diameter equal to 1400 mm but with different ratios between final height and final thickness. The simulation study cases are those also shown in Quagliato (2016). The rationale behind the choice of this validation strategy is given by the fact that the strains in the ring are not largely influenced by the dimensions of the ring but by the initial and final distribution of the material in the cross-section of the ring itself. In addition to that, ranging between a relatively thin ring, $h_F/s_F = 3$, to a relatively thick ring, $h_F/s_F = 0.7$, the accuracy of the model in predicting predominant radial strain or predominant vertical strain conditions could be analyzed. The initial and final dimensions for the ring as well as the ratio between final height and final thickness are reported in Table 6, whereas the relevant process parameters in Table 7.

Table 6 – Strain estimation algorithm validation cases.

	Ring1S	**Ring2S**	**Ring3S**	**Ring4S**
d_0 [mm]	600.00	600.00	600.00	600.00
D_0 [mm]	821.74	876.15	917.87	986.57
s_0 [mm]	110.87	138.08	158.94	193.28
h_0 [mm]	214.69	208.24	158.93	152.84
d_F [mm]	1270.00	1220.00	1130	1070.00
D_F [mm]	1400.00	1400.00	1400.00	1400.00
s_F [mm]	65.00	90.00	135.00	165.00
h_F [mm]	195.00	180.00	135.00	115.00
h_F/ s_F [–]	3.00	2.00	1.00	0.70

Table 7 – Strain estimation algorithm validation cases process parameters.

	Ring1S	**Ring2S**	**Ring3S**	**Ring4S**
$v_{M,0}$ [mm/s]	6.00	5.50	4.50	5.00
$v_{M,F}$ [mm/s]	3.90	3.50	3.00	3.00
$v_{A,0}$ [mm/s]	3.10	3.65	4.50	6.32
$v_{A,F}$ [mm/s]	1.30	1.75	3.00	4.30

Since no previous literature models where available, the validation of the strain estimation model has been carried out by comparing the analytical prediction with the results of the relevant numerical simulation, for the study cases reported in Table 6.

In relation to the validation of the temperature model, being the heat transfer largely influenced by the size of the ring, in terms of its mass, a larger amount of simulation study cases have been carried out. The considered study cases range between 650 mm to 2400 mm for the final outer diameter of the ring and, for each of the considered final outer diameters, three different study cases with the ratio between the final height and the final thickness equal to 3, 2 and 1 have been considered, for a total of 30 cases. The simulation study cases are those summarized in Quagliato (2017).

Table 8 – Temperature model validation cases ring geometries and process parameters.

		Ring blank dimensions			**Final ring dimensions**			**Mandrel feeding speed**	
Ring Case	G_f	**Outer diam. [mm]**	**Inner diam. [mm]**	**Height [mm]**	**Outer diam. [mm]**	**Inner diam. [mm]**	**Height [mm]**	**Initial speed [mm/s]**	**Final speed [mm/s]**
Ring1T	3.0	575.25	325.00	218.75	1100.00	975.00	190.00	7.2	5.0
Ring2T	2.0	621.60	325.00	209.00	1100.00	930.00	170.00	6.5	4.5
Ring3T	1.0	668.70	325.00	171.80	1100.00	855.00	122.50	5.8	4.5
Ring4T	3.0	518.85	325.00	195.43	800.00	680.00	180.00	7.7	6.6
Ring5T	2.0	550.92	325.00	175.44	800.00	645.00	155.00	7.5	5.0
Ring6T	1.0	574.51	325.00	124.76	800.00	600.00	100.00	6.0	4.5
Ring7T	3.0	821.74	600.00	214.69	1400.00	1270.00	195.00	6.0	3.9
Ring8T	2.0	876.15	600.00	208.24	1400.00	1220.00	180.00	5.5	3.5
Ring9T	1.0	917.87	600.00	158.93	1400.00	1130.00	135.00	4.5	3.0
Ring10T	3.0	544.04	325.00	201.98	950.00	830.00	180.00	6.7	4.6
Ring11T	2.0	589.95	325.00	194.85	950.00	785.00	165.00	6.0	4.5
Ring12T	1.0	650.19	325.00	162.60	950.00	700.00	125.00	6.0	4.5
Ring13T	3.0	837.80	600.00	207.21	1700.00	1580.00	180.00	6.0	3.0
Ring14T	2.0	897.70	600.00	209.36	1700.00	1530.00	170.00	5.5	3.0
Ring15T	1.0	943.41	600.00	171.71	1700.00	1460.00	120.00	4.7	3.0
Ring16T	3.0	490.53	325.00	188.81	650.00	530.00	180.00	7.0	5.0
Ring17T	2.0	510.93	325.00	156.24	650.00	505.00	145.00	7.0	5.0
Ring18T	1.0	549.33	325.00	112.17	650.00	450.00	100.00	6.0	4.5
Ring19T	3.0	682.81	450.00	213.88	1250.00	1125.00	190.00	6.5	4.0
Ring20T	2.0	730.52	450.00	203.34	1250.00	1080.00	170.00	6.5	4.0
Ring21T	1.0	809.30	450.00	179.65	1250.00	980.00	135.00	5.7	4.0
Ring22T	3.0	875.65	600.00	226.25	2000.00	1875.00	190.00	5.5	2.7
Ring23T	2.0	944.45	600.00	232.41	2000.00	1820.00	180.00	5.5	2.7
Ring24T	1.0	1049.33	600.00	224.67	2000.00	1700.00	150.00	4.7	2.7
Ring25T	3.0	908.68	600.00	243.72	2200.00	2067.00	200.00	5.5	2.3
Ring26T	2.0	947.15	600.00	227.61	2200.00	2030.00	170.00	5.3	2.3
Ring27T	1.0	1070.05	600.00	235.03	2200.00	1900.00	150.00	4.5	2.3
Ring28T	3.0	910.07	600.00	237.13	2400.00	2275.00	190.00	5.5	2.3
Ring29T	2.0	964.80	600.00	234.40	2400.00	2230.00	170.00	5.3	2.3
Ring30T	1.0	1089.59	600.00	244.79	2400.00	2100.00	150.00	4.4	2.3

In Table 8, the values in the second column represent the ratio between the final height and the final thickness of the ring, defined by the symbol G_f.

Additionally, in Quagliato (2017), the slip line model developed by Hill (1950) for a case of a flat punch acting on a flat surface has been employed for the estimation of the radial forming force and the limitations of this approach, also used in other literature works, Hawkyard (1973) and Mamalis (1976), has been highlighted. The results of the accuracy of the lumped temperature model, as well as this last-mentioned ones concerning the estimation of the radial forming force by means of the slip line model proposed by Hill (1950), are reported in chapter 6.

Finally, for the validation of the developed slip line based force model, whose relevant paper is under review at the International Journal of Mechanical Science (submission August 2017), has been carried out by comparison with both numerical and experimental results. Nine different numerical study cases with ring ranging from 800 mm to 2000 mm as ring final outer diameter have been carried out and the process settings are reported in following Table 9.

Table 9 – Slip line based force algorithm validation cases ring geometries and process parameters.

Case	**Ring initial geometry [mm]**			**Ring final geometry [mm]**			**Mandrel speed [mm/s]**		**Upper Axial roll speed [mm/s]**	
	Outer diam.	Inner diam.	Height	Outer diam.	Inner diam.	Height	Initial	Final	Initial	Final
Ring1F	518	325	195	800	680	180	7.70	6.00	3.82	2.00
Ring2F	551	325	175	800	645	145	7.50	5.00	4.83	2.50
Ring3F	575	325	125	800	600	100	6.00	4.50	6.00	4.50
Ring4F	822	600	215	1400	1270	195	6.00	3.90	3.10	1.30
Ring5F	876	600	208	1400	1220	180	5.50	3.50	3.65	1.75
Ring6F	918	600	159	1400	1155	123	4.50	3.00	4.50	3.00
Ring7F	876	600	226	2000	1875	190	5.50	2.70	3.35	0.89
Ring8F	945	600	232	2000	1820	180	5.00	2.70	3.71	1.35
Ring9F	1049	600	225	2000	1700	150	4.70	2.70	4.70	2.70

4.4 Mesh sensitivity analysis

In order to analyze the influence of the mesh size of the accuracy of the simulation results, the case of a ring with initial dimension equal to R_0 = 575.25 mm, r_0 = 325.00 mm, h_0 = 218.75 mm and final geometry equal to R_F = 1100.00 mm, r_F = 975.00 mm, h_F = 190.00 mm has been taken into account (R1F in Table 8).

The geometry of the ring rolling mill utilized in most of the study cases are reported in Table 2, the general process boundary conditions and settings in Table 3 whereas the material information are those reported in section 4.1 and relevant for the 42CrMo4 steel alloy.

Four different mesh densities have been taken into account and the variation of the percentual maximum radial forming force, in comparison to the previous mesh study case, has been calculated. The relevant information is reported in Table 10.

Table 10 – Mesh influence verification study cases.

	Mesh size [mm]						
Mesh case	**Axial**	**Radial**	**Tangential**	**Number of elements**	**Computational time [h-m]**	**Max radial force [kN]**	**Relative error**
0	34	32	34	1728	5h 38’	1290.2	-
1	24	22	24	4560	10h 32’	1395.1	7.52 %
2	20	18	20	8640	16h 25’	1379.8	1.11 %
3	14	12	14	20280	73h 3’	1366.7	0.96 %

As shown in Table 10, the relative difference between mesh case 0 and 1 is too much high, the mesh case 2 has been also run, showing an error a little greater than 1%. To confirm the trend, also mesh case 3 was run, with a considerable increase of the computational time. For this reason, being the computation time of mesh case 2 lower than mesh case 3 and being the result, in terms of maximum radial forming force, very similar each other, the mesh settings of mesh case 2 have been utilized in all the analyzed study cases.

For this reason, as mentioned above, all FE models were meshed utilizing a hexahedral 3D element with dimensions of 20 mm (axial), 18 mm (radial) and 20 mm (tangential).

Chapter 5: Laboratory experiments

Even if the experimental campaigns on the ring rolling process are complex, high time-consuming and expensive, both concerning the utilization of the machine and for the materials, a limited number of experiments have been carried out by utilizing a laboratory-size ring rolling machine and a soft Pb75-Sn25 alloy. The reason for the utilization of this soft alloy is given by the fact that its plastic behavior under severe plastic deformations at room temperature resembles that of steel at high temperature.

As just mentioned, the ring rolling experiments have been carried out on a laboratory size ring rolling machine, Fig. 42, which has lower power on the actuators of the tools but allows to carry out experiments for the verification of the developed models, both from the kinematic and the dynamic point of view.

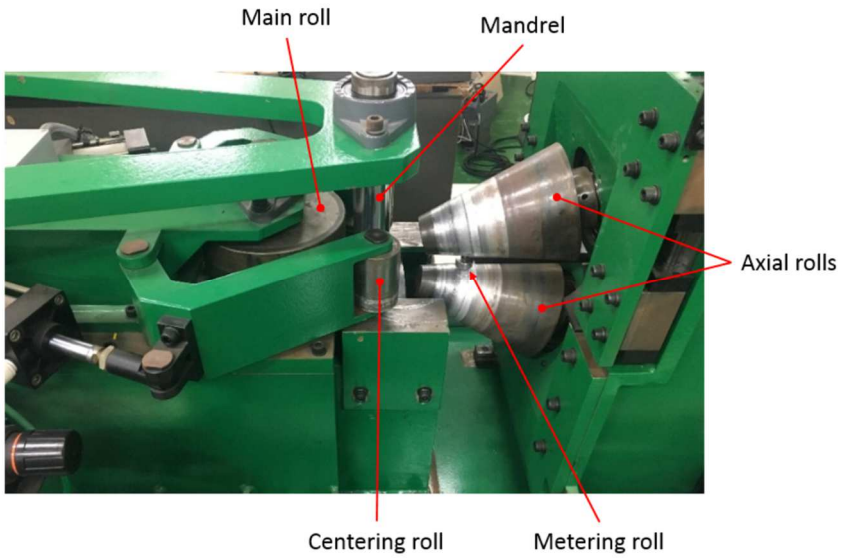

Fig. 42 – Laboratory size ring rolling machine.

In terms of kinematic, the geometrical expansion of the ring is recorded by a metering roll always in contact with the ring on the opposite side of the mandrel-main roll deformation gap. Concerning the

dynamic measurements, both main roll and upper axial roll actuators are equipped with load cells those allow the record of the load data during the ring rolling process. The main specifications of the utilized ring rolling machine are reported in following Table 11. In addition to that, differently compared with the majority of the industrial ring rolling machines, the radial feeding of that utilized for the experiments is operated by the main roll rather than the mandrel. The choice of the difference is related to the construction procedure which made easier to apply the actuator on a tool with a larger diameter, such as the main roll.

Table 11 - Ring rolling test machine data, ring dimensions, and process conditions.

Parameters	**Value**
Mandrel diameter	50 mm
Main roll diameter	200 mm
Axial rolls working plane length	190 mm
Axial rolls vertex angle	15.166 °
Guide rolls diameter	60 mm
Main roll rolling speed (maximum)	60 rpm
Mandrel maximal pushing force	55 kN
Upper axial roll maximal pushing force	45 kN

Concerning the utilized Pb75-Sn25 soft alloy, the material properties have been determined by means of compression test at room temperature and considering different strain rates, as shown in Fig. 43. The plastic behavior of the material has been fitted with the power law reported in Eq. (170) and the relevant model constants are reported in Table 12.

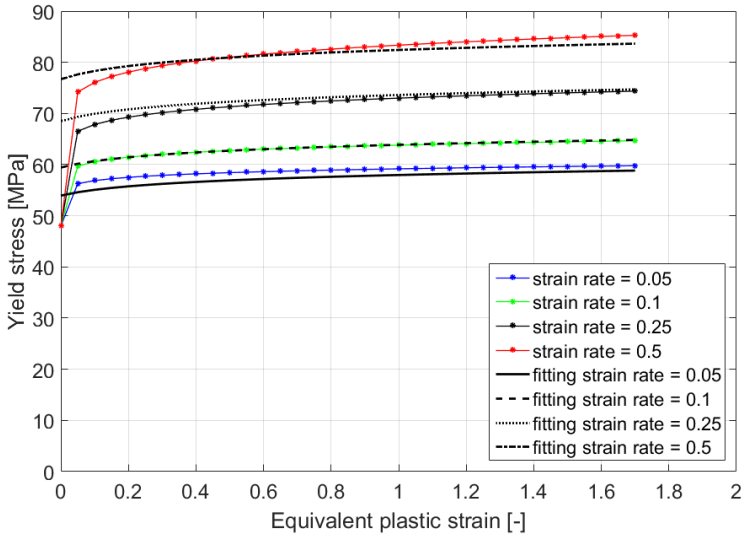

Fig. 43 – Material properties of Pb75-Sn25 alloy and plastic behavior fitting curves.

$$\sigma = K_0 \left(a_0 + \varepsilon\right)^{a_1} \left(b_0 + \dot{\varepsilon}\right)^{b_1} \tag{170}$$

Table 12 – Material model constants for the Pb75-Sn25 material.

Parameters	Value	Parameters	Value
K_0	92	b_0	0.015
a_0	0.1	b_1	0.17
a_1	0.03		

Material Eq. (170) is a strain-strain rate uncoupled flow stress model based on the concept of the Swift power law which allows accounting for the strain rate effect on the material flow stress. Since the experiments have been carried out at room temperature, no temperature term has been included in the material model. The utilized soft alloy has a density, Young's modulus and Poisson ratio equal to 9947.3 kg/dm^3, 28 GPa and 0.42, respectively.

Concerning the manufacturing of the rings for the experiments, they have been obtained by melting Pb75-Sn25 ingots and pouring the molten metal inside two different ring molds, with the dimensions reported in Table 13.

Table 13 – Initial and final dimensions of the Pb75-Sn25 rings.

Ring-Exp-1	**Value**	**Ring-Exp-2**	**Value**
D_0	200 mm	D_0	155 mm
d_0	150 mm	d_0	105 mm
s_0	25 mm	s_0	25 mm
h_0	40 mm	h_0	42 mm
D_F	235 mm	D_F	195 mm
d_F	195 mm	d_F	155 mm
s_F	20 mm	s_F	20 mm
h_F	37 mm	h_F	36 mm

The process settings for the two experiments are summarized in Table 14 whereas the images of the rings before and after the ring rolling process are shown in Fig. 44a and 44b for the Ring-Exp-1 and in Fig. 44c and 44d for the Ring-Exp-2.

Table 14 – Process settings for the Pb75-Sn25 ring's experiments.

Ring-Exp-1	**Value**	**Ring-Exp-2**	**Value**
$v_{M,0}$ [mm/s]	0.23	$v_{M,0}$ [mm/s]	0.075
$v_{M,F}$ [mm/s]	0.16	$v_{M,F}$ [mm/s]	0.025
$v_{A,0}$ [mm/s]	0.14	$v_{A,0}$ [mm/s]	0.05
$v_{A,F}$ [mm/s]	0.09	$v_{A,F}$ [mm/s]	0.03
ω_S [rad/s]	2.09	ω_S [rad/s]	2.09
Rolling time [s]	42	Rolling time [s]	60
Calibration time [s]	13	Calibration time [s]	20

Fig. 44 – (a) Initial and (b) final ring for the Ring-Exp-1 and (c) initial and (d) final ring for the Ring-Exp-2.

The data coming from the metering roll and from the load cells installed on the main roll and on the upper axial roll have been recorded and are reported, along with the relevant results from the numerical simulations and the analytical models in the following chapter of the thesis.

Chapter 6: Results and discussion

In this last section of the paper, the results of the analytical models presented in previous chapter 3 will be presented one by one, starting from those relevant for the estimation of the geometrical expansion of the ring to the estimation of radial and axial process forces. As previously anticipated, in case previous literature models where available in the literature, a cross-comparison with the developed one and with the relevant numerical simulation will be also proposed. In addition to that, concerning the two experimental cases detailed in previous chapter 5, a cross-comparison among analytical, numerical and experimental results concerning the evolution of the outer diameter of the ring and of both radial and axial forming force will be presented.

6.1 Process setting and ring geometry algorithms performances

The developed model for the estimation of the evolution of the ring geometry throughout the process has been validated by applying it to six different study cases, previously summarized in Table 4 in terms of ring initial and final geometry and in Table 5 in terms of process parameters. The results of the numerical simulation, in terms of stability of the expansion of the ring as well as the absence of irregular expansion at the end of the process, will testify the reliability of the algorithm for the choice and determination of the process parameters. In addition to that, the accuracy in predicting the geometrical expansion of the outer diameter of the ring and also to account for the calibration phase, absent in previous literature models, will be the proof of the improvement of the developed model in comparison to previous literature one.

In Fig. 45 to Fig. 50, the images of initial and final conditions for the ring rolling process, in terms of equivalent plastic strain, are reported and, as it can be evinced from the appearance of the ring, in all the cases the ring shows a good circularity at the end of the process. The initial beginning of the process is shown in the figure “(a)” whereas the end at the figure “(b)”, respectively.

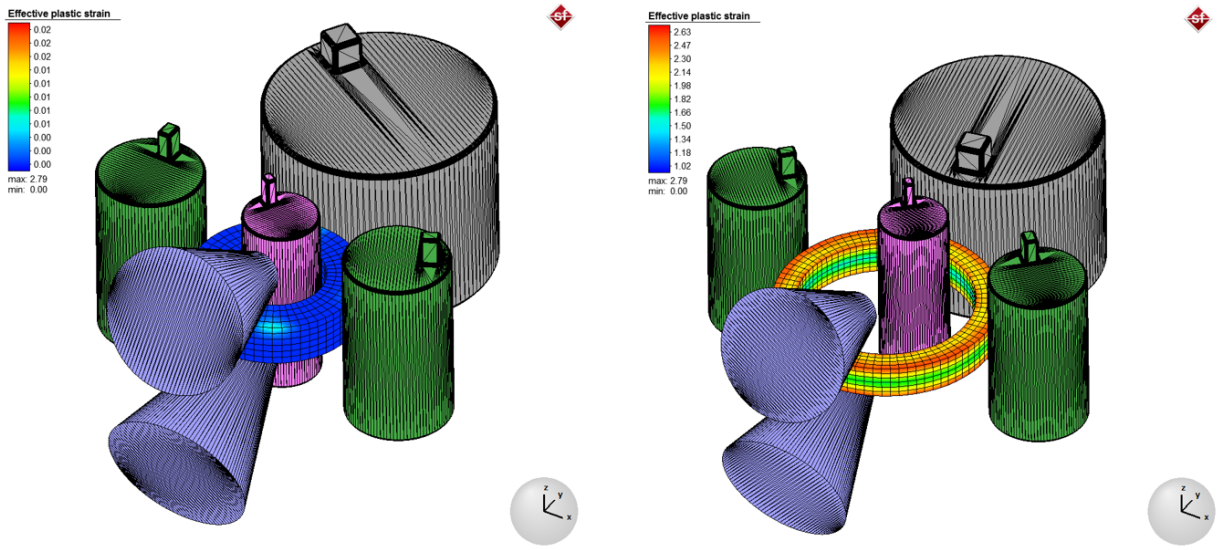

(a)
R1G Beginning of the process

(b)
R1G Beginning of the process

Fig. 45 – (a) Initial and (b) final results for the Ring1G.

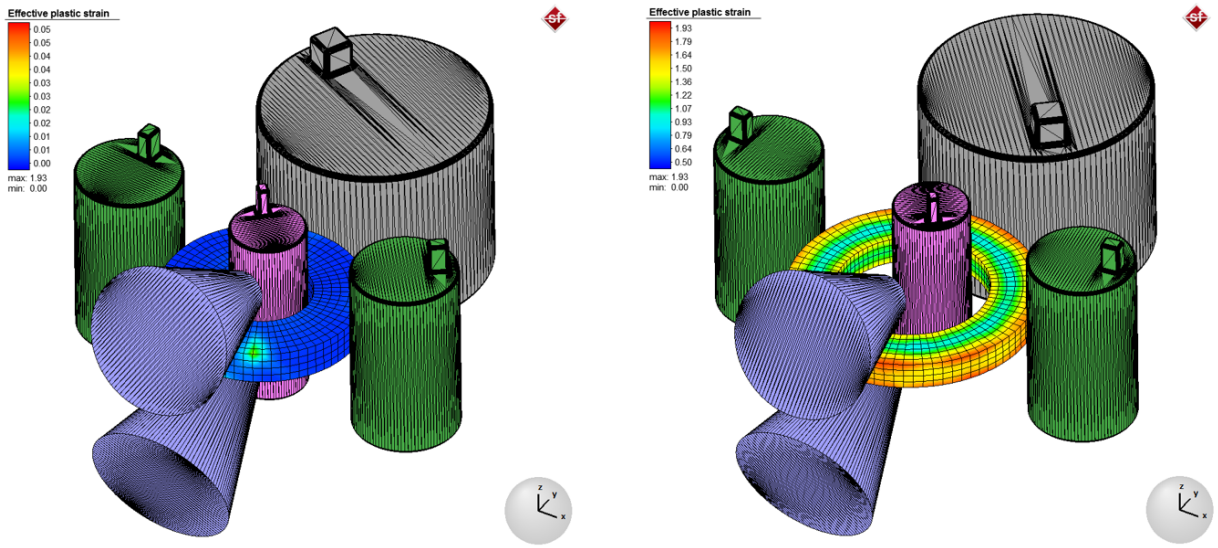

(a)
R2G Beginning of the process

(b)
R2G Beginning of the process

Fig. 46 – (a) Initial and (b) final results for the Ring2G.

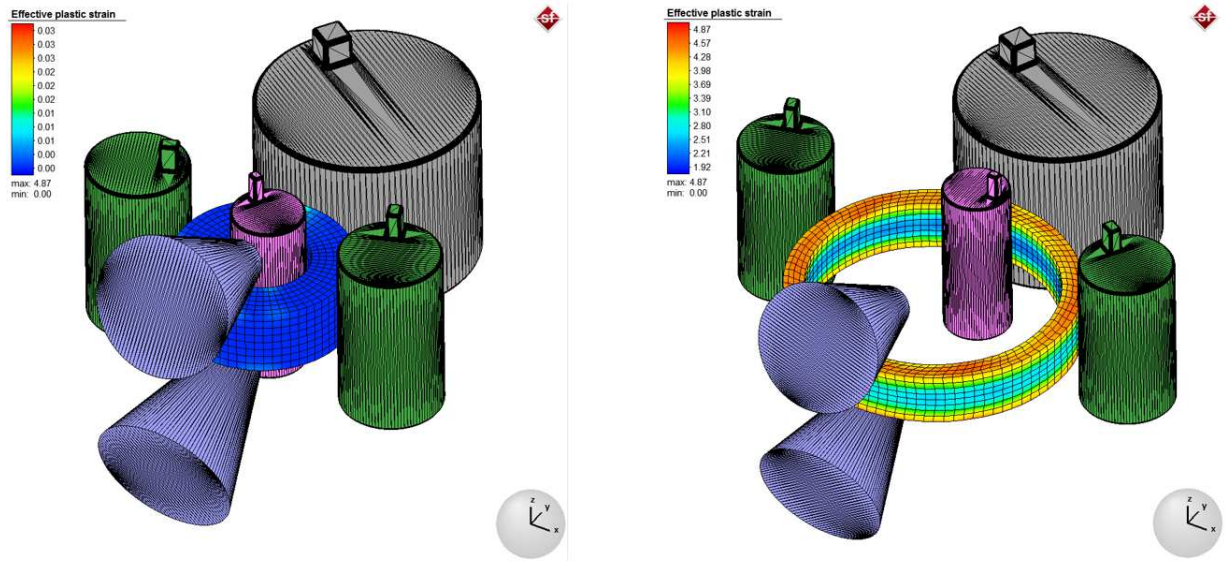

(a)
R3G Beginning of the process

(b)
R3G Beginning of the process

Fig. 47 – (a) Initial and (b) final results for the Ring3G.

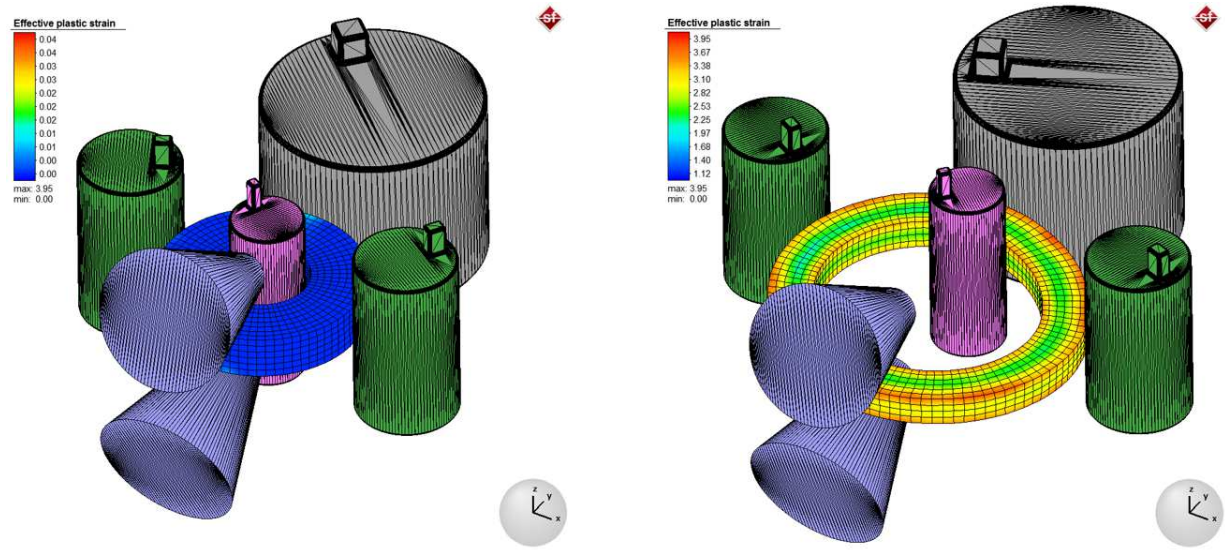

(a)
R4G Beginning of the process

(b)
R4G Beginning of the process

Fig. 48 – (a) Initial and (b) final results for the Ring4G.

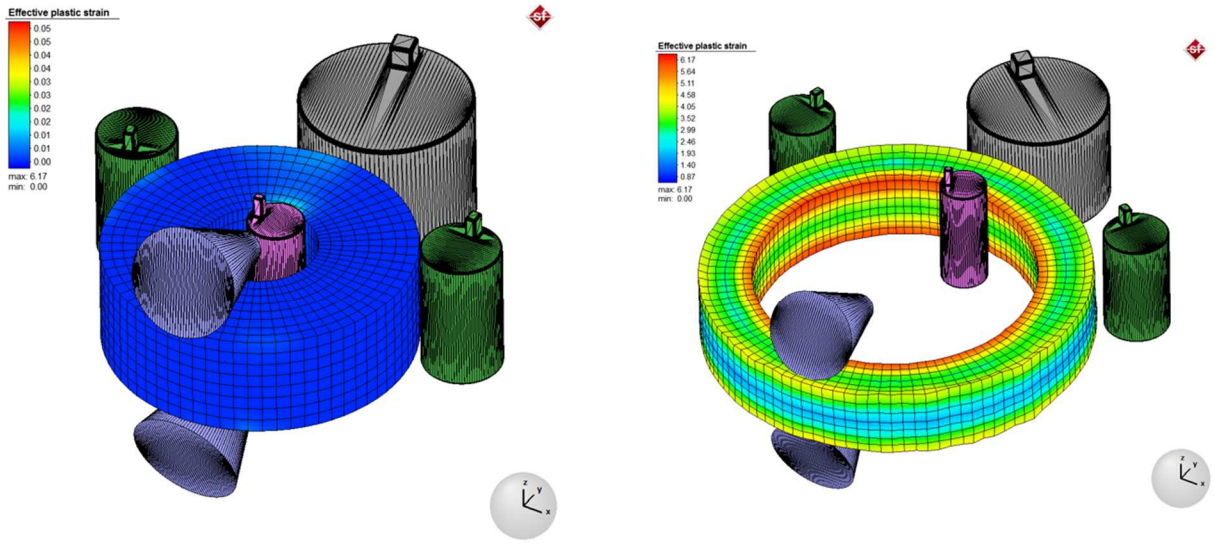

(a)
R5G Beginning of the process

(b)
R5G Beginning of the process

Fig. 49 – (a) Initial and (b) final results for the Ring5G.

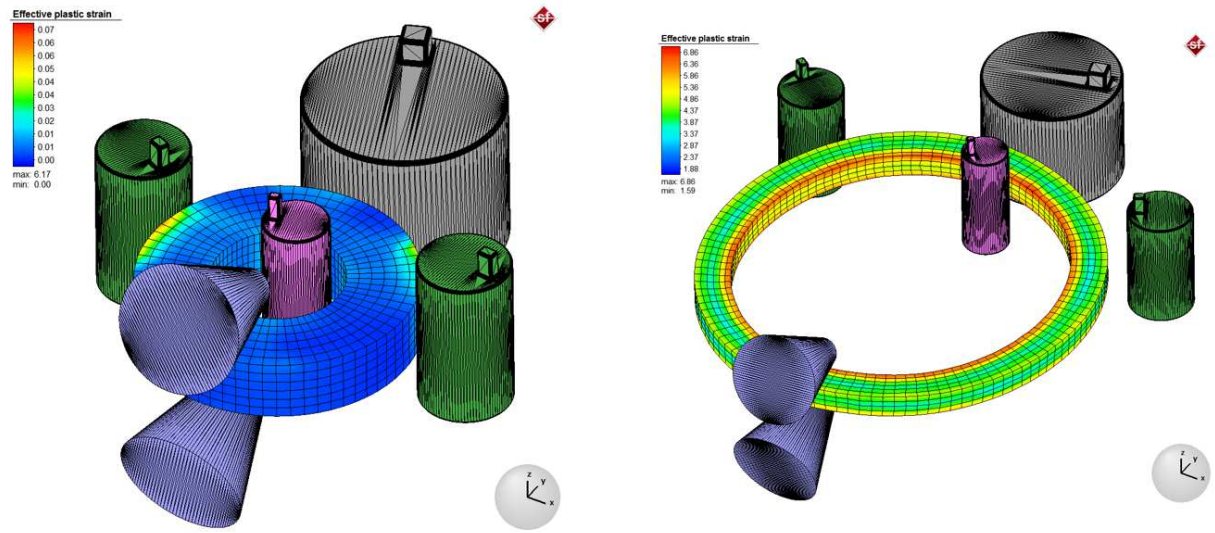

(a)
R5G Beginning of the process

(b)
R5G Beginning of the process

Fig. 50 – (a) Initial and (b) final results for the Ring4G.

The comparison among the numerical simulation, the developed model for the estimation of the ring geometry expansion and the result of the same analytical estimation carried out by utilizing the model proposed by Zhou (2011), in terms of outer diameter of the ring, are presented in Fig. 51 to Fig. 56, respectively.

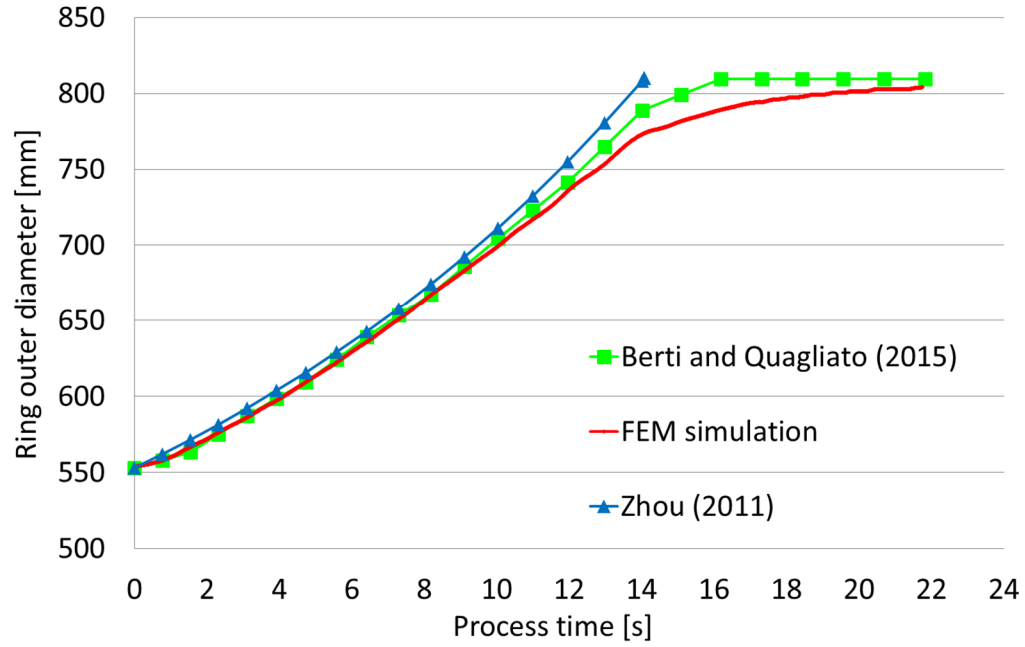

Fig. 51 – Berti and Quagliato (2015), Zhou (2011) and FEM simulation results for the evolution of the outer diameter of the Ring1G.

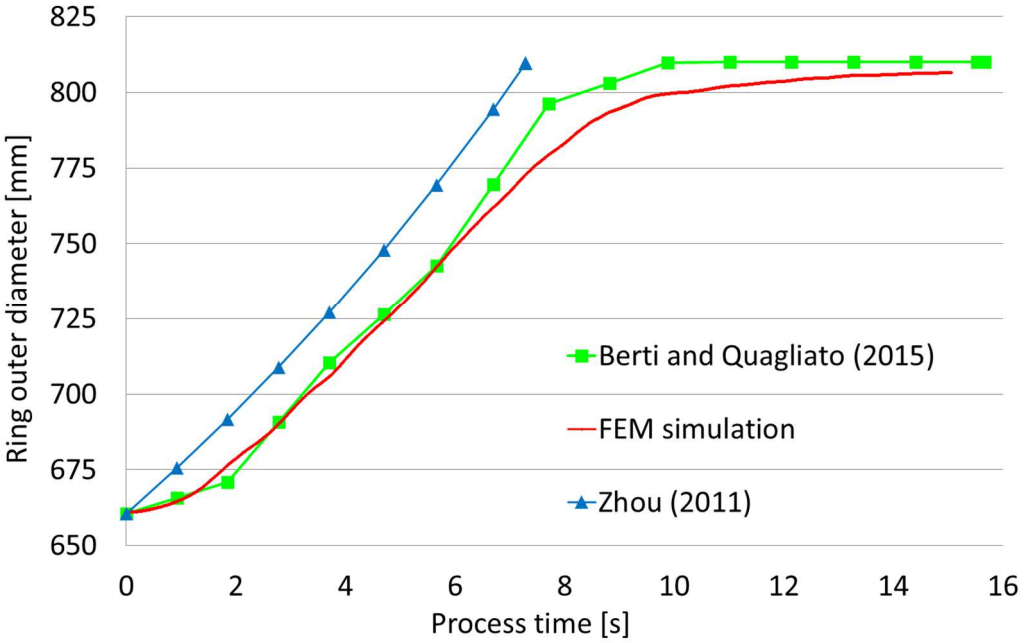

Fig. 52 – Berti and Quagliato (2015), Zhou (2011) and FEM simulation results for the evolution of the outer diameter of the Ring2G.

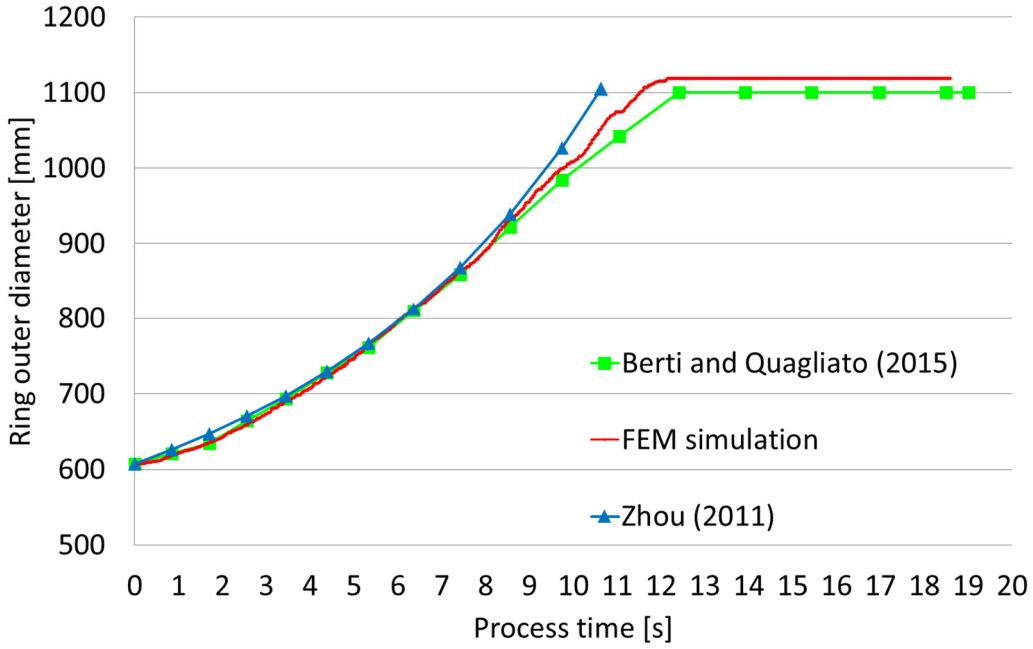

Fig. 53 – Berti and Quagliato (2015), Zhou (2011) and FEM simulation results for the evolution of the outer diameter of the Ring3G.

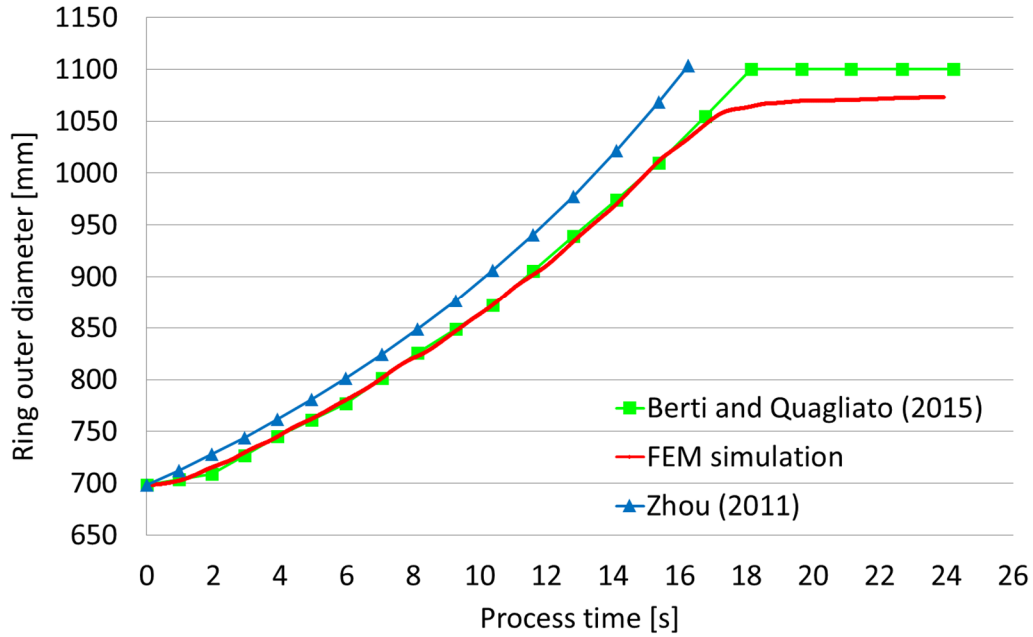

Fig. 54 – Berti and Quagliato (2015), Zhou (2011) and FEM simulation results for the evolution of the outer diameter of the Ring4G.

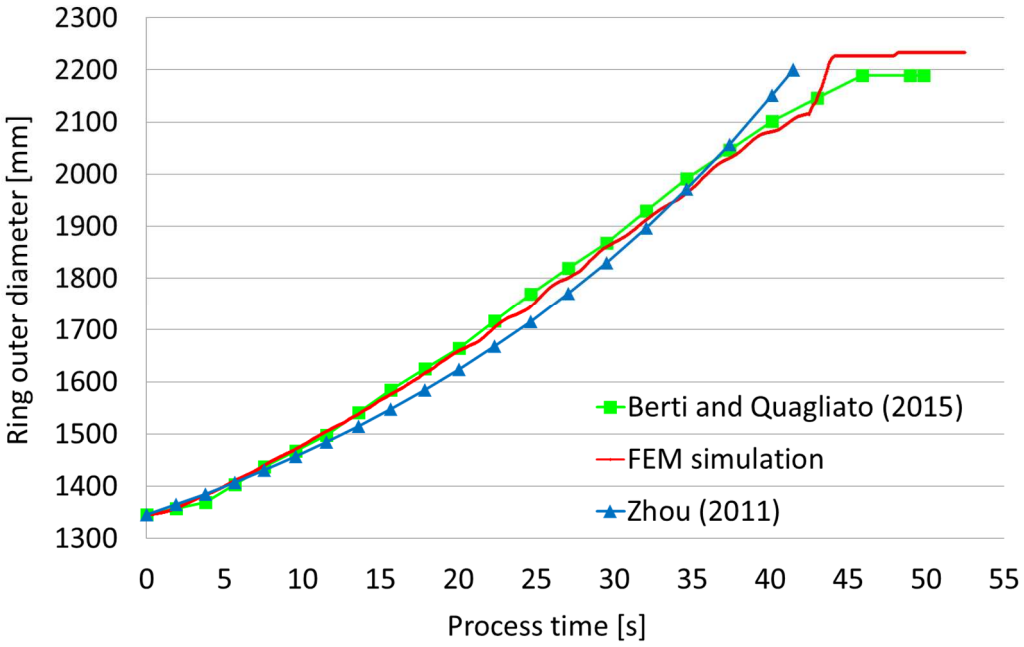

Fig. 55 – Berti and Quagliato (2015), Zhou (2011) and FEM simulation results for the evolution of the outer diameter of the Ring5G.

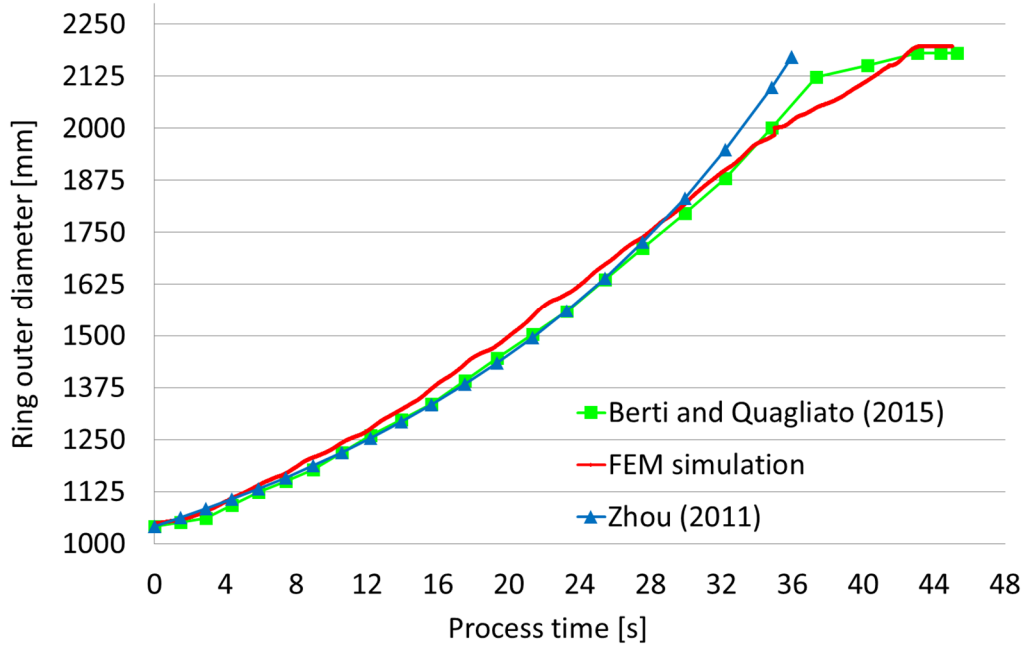

Fig. 56 – Berti and Quagliato (2015), Zhou (2011) and FEM simulation results for the evolution of the outer diameter of the Ring6G.

For all the study cases shown in Fig. (51) to Fig. (56), the proposed model is able to follow the natural transition zone between expansion and calibration of the ring, whereas the previous literature model, Zhou (2011), tends to anticipate the time at which the ring reaches its final diameter as well as it does not account for the calibration phase.

As it will be shown in the following section, the enhancement of the calculation carried out by considering the incremental geometry, which causes left and right faces of each slice to have different dimensions, even a higher accuracy of that shown so far will be achieved.

In order to highlight the limitations of the model proposed by Hua (1997), also utilized by Zhou (2011), Gou (2011), Wang (2010) and Yan (2007), the case of Ring3G has been taken into account. By calculating the ranges for the mandrel feeding speed according to the algorithm proposed in Zhou (2011), it results in the extreme values shown in the first column of Table 15 whereas, by utilizing that proposed in Berti and Quagliato (2015), two different ranges are calculated, one for the choice of the initial mandrel feeding speed and one for the choice of the final one, as shown in the second column of Table 15.

Table 15 – Mandrel and upper axial roll feeding speed interval

Reasonable ranges for mandrel and upper axial roll feed speed proposed **by Zhou (2011)**	Reasonable ranges for mandrel and upper axial roll feed speed proposed **in Berti and Quagliato (2015)**	Chosen Values (according to Berti and Quagliato (2015) ranges)
$0.602 < v_{M,0} < 6.733$	$0.602 < v_{M,0} < 9.161$	$v_{M,0} = 7.50$ mm/s
	$0.124 < v_{M,F} < 6.733$	$v_{M,F} = 5.00$ mm/s
$4.284 < v_{A,0} < 16.004$	$4.284 < v_{A,0} < 26.170$	$v_{A,0} = 1.88$ mm/s
	$1.573 < v_{A,F} < 16.004$	$v_{A,F} = 4.55$ mm/s

If the range for the mandrel feeding speed is calculated according to Zhou (2011), both initial and final mandrel feeding speed should be chosen inside the same range, a fact which makes the resulting upper axial roll feeding speed not to fall inside the prescribed range, whatever choice is made for the mandrel feeding speed. Thus, according to Zhou (2011), there is no feasible mandrel feeding speed for the mandrel which makes the relevant axial roll feeding speed to fall inside the prescribed ranges or, in other words, the process cannot be carried out without either instabilities or irregular expansions of the ring. However, as demonstrated both Fig. 47 and Fig. 53, by utilizing the model proposed in Berti and Quagliato (2015) the process can be carried out until the end, granting a uniform expansion of the ring, without instabilities or irregularities in the final ring shape. The relevant simulation has been set-up with the process parameters reported in the last column of Table 15.

6.2 3D strain tensor estimation and geometry update results

In order to map the evolution of the three strain components as well as of the equivalent plastic strain during the process, one process variable tracking strategy available in Simufact.Forming has been utilized. In Fig. 57, the blue dots represent the so-called particles, material points attached to the mesh of the ring which allows recording local results during the process. The choice of placing the particles in the middle of the cross-section of the ring is given by the fact that on the top, or at the bottom, of the ring, local deformations could give unprecise results. On the other hand, in the middle of the cross-section of the ring, along the vertical direction, the strain distribution is more uniform and allows a better comparison with the estimation carried out with the developed numerical model, presented in section 3.4.

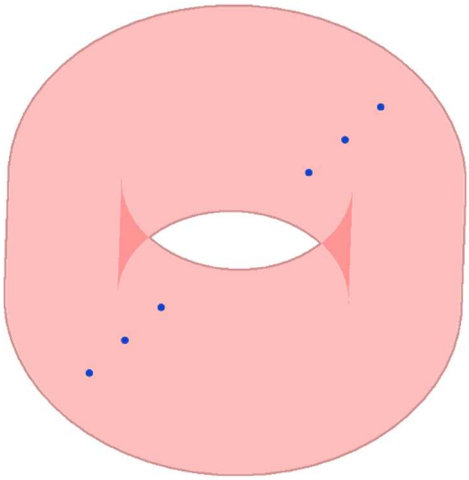

Fig. 57 – Strain components and equivalent plastic strain tracking strategy (particle tracking).

By utilizing the proposed model, the three strain components as well as the equivalent plastic strain, both at the inner radius and outer radius of the ring have been estimated throughout the process. The considered study cases are those previously listed in Table 6, whose relevant process settings are reported in Table 7. For the tracking of both strain components and equivalent plastic strain, the particles located at the inner side and outer side of the ring have been utilized.

As it is possible to see from the results reported in Fig. 58 to Fig. 61, the increment of the strain is caused by the deformation occurring in the ring in both deformation gaps, according to the amount of thickness and height drafts. For the plot of the results, the first slice to enter the deformation gap, after the start of the process, has been selected both for the numerical simulation and in the analytical computation.

In the comparison between analytical and numerical results, some anticipation or postponements made by the analytical model can be seen and are related to presence of small slippage between the ring and the tools, which can are considered in the numerical simulation but, due to their causality, cannot be accounted for in the analytical model. These small differences gradually reduce from the middle to the end of the ring rolling process, where the process becomes more stable and less slippage occurs between ring and tools.

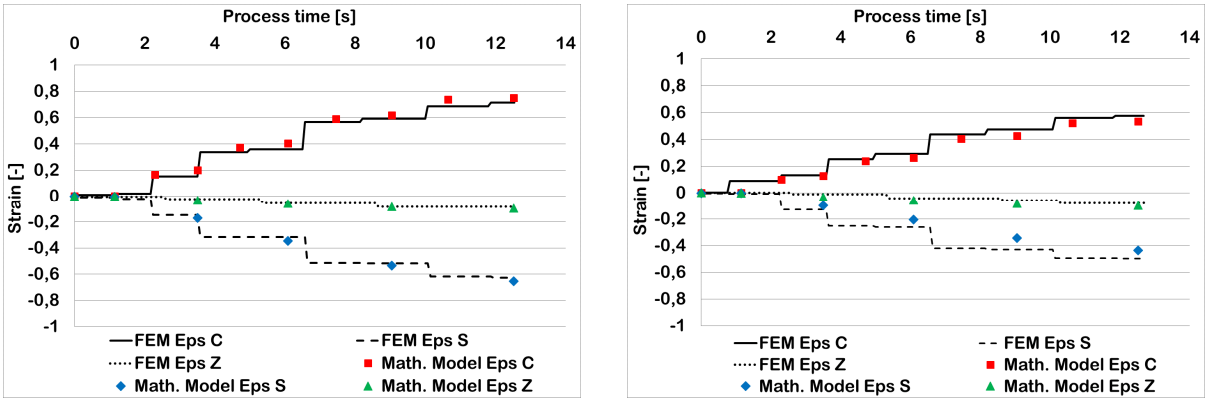

Fig. 58 – Strain components for inner (left) and outer (right) radii of the ring for Ring1S.

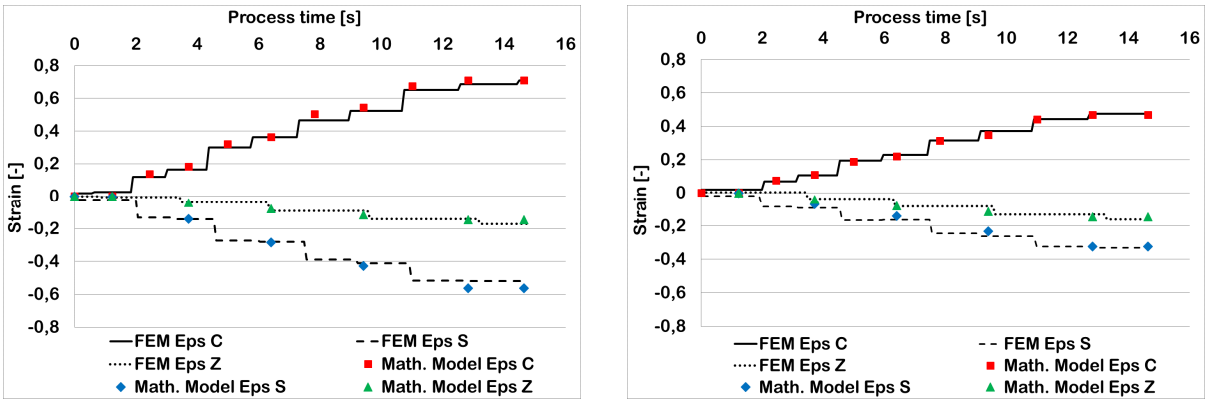

Fig. 59 – Strain components for inner (left) and outer (right) radii of the ring for Ring2S.

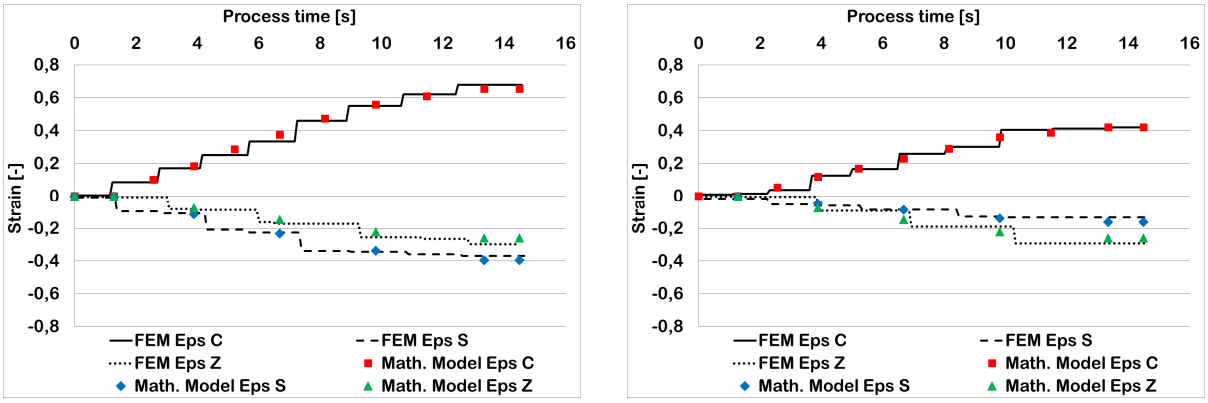

Fig. 60 – Strain components for inner (left) and outer (right) radii of the ring for Ring3S.

Concerning the estimation of the equivalent plastic strain, in order to estimate the accuracy of its prediction, the results relevant for the inner and the outer radius of the ring, for each round of the rolling process, both from the analytical calculations and numerical simulations, are reported in Table 16.

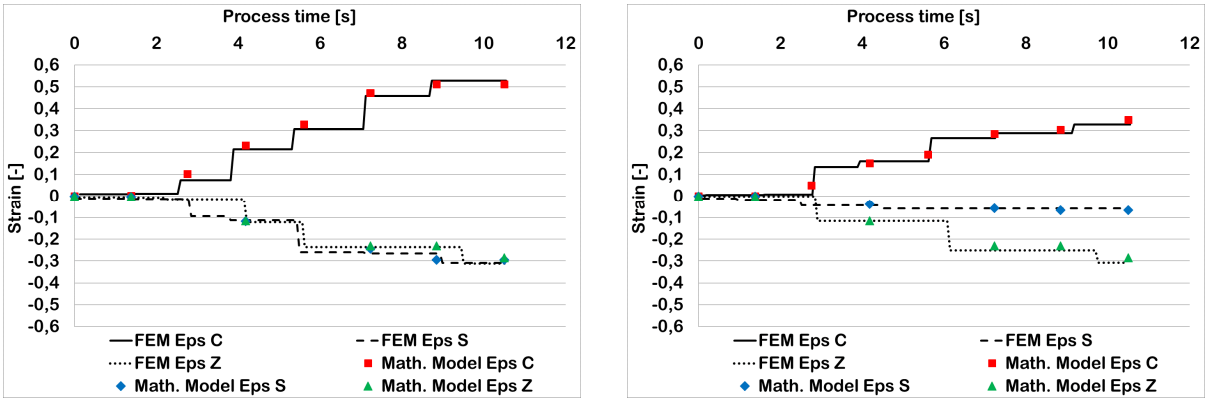

Fig. 61 – Strain components for inner (left) and outer (right) radii of the ring for Ring4S.

Table 16 – Effective plastic strain comparisons and errors

Ring1S	Inner radius					Outer radius				
Ring round	1	2	3	4	5	1	2	3	4	5
Eq. Pl. Strain Quagliato ('16)	0.174	0.391	0.658	0.905	1.035	0.211	0.368	0.682	0.795	0.986
Eq. Pl. Strain FEM simulation	0.179	0.396	0.6669	0.903	1.008	0.195	0.367	0.681	0.822	1.043
% Error	2.87%	1.28%	1.67%	0.19%	2.61%	7.58%	0.27%	0.15%	3.40%	5.78%
Ring2S	Inner radius					Outer radius				
Ring round	1	2	3	4	5	1	2	3	4	5
Eq. Pl. Strain Quagliato ('16)	0.141	0.410	0.560	0.674	0.827	0.105	0.400	0.575	0.697	0.893
Eq. Pl. Strain FEM simulation	0.130	0.390	0.537	0.673	0.805	0.099	0.367	0.564	0.718	0.894
% Error	8.69%	5.13%	4.28%	0.15%	2.73%	5.63%	9.26%	1.95%	2.92%	0.11%
Ring3S	Inner radius					Outer radius				
Ring round	1	2	3	4	5	1	2	3	4	5
Eq. Pl. Strain Quagliato ('16)	0.106	0.394	0.513	0.760	0.897	0.077	0.275	0.529	0.810	0.946
Eq. Pl. Strain FEM simulation	0.104	0.386	0.500	0.773	0.916	0.089	0.275	0.508	0.814	0.916
% Error	2.37%	2.07%	2.60%	1.68%	2.07%	13.77%	0.00%	4.24%	0.43%	3.28%
Ring4S	Inner radius					Outer radius				
Ring round	1	2	3	4	5	1	2	3	4	5
Eq. Pl. Strain Quagliato ('16)	0.105	0.338	0.617	0.910	-	0.213	0.476	0.724	0.938	-
Eq. Pl. Strain FEM simulation	0.116	0.349	0.633	0.894	-	0.211	0.411	0.708	0.941	-
% Error	9.32%	3.07%	2.50%	1.73%	-	1.04%	7.73%	2.26%	0.31%	-

Considering the results reported in Table 16 concerning the estimation of the equivalent plastic strain, its estimation is carried out with a maximum error of 13.77% if the first round of the process is considered and of 9.26% is it is ignored. As previously mentioned, the issue related to the slippage in the first stages of the ring rolling is one of the reasons for a higher inaccuracy in the first round. In addition to that, in the

first round of the process, the absolute strain components are normally relatively small and this makes the percentage error to be more evident.

Thanks to the geometry update based on the calculation of the strain the so-called third-directions, the vertical one in the mandrel-main roll deformation gap and the radial one in the axial rolls gap, also the accuracy of the geometry estimation is increased. As shown in Fig. 62 to Fig. 65, the utilization of the enhanced algorithm for the estimation of the outer diameter of the ring, Quagliato (2016), allows to reduce the discrepancies between analytical and numerical results, in comparison to the previously developed one and that previously proposed in the literature, namely Zhou (2011).

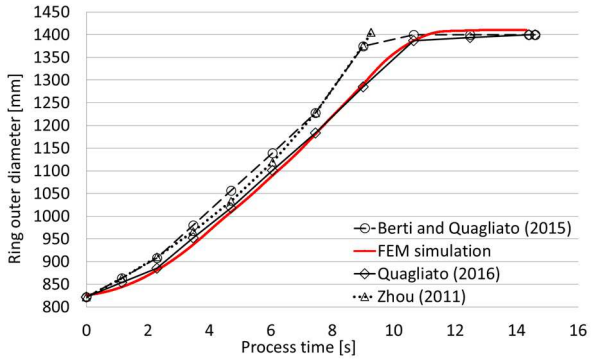

Fig. 62 – Cross-comparison of Quagliato (2016), Berti and Quagliato (2015), Zhou (2011) and FEM simulation for the estimation of the outer diameter of Ring1S.

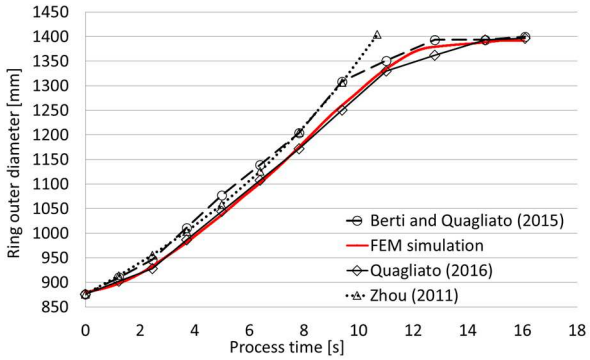

Fig. 63 – Cross-comparison of Quagliato (2016), Berti and Quagliato (2015), Zhou (2011) and FEM simulation for the estimation of the outer diameter of Ring2S.

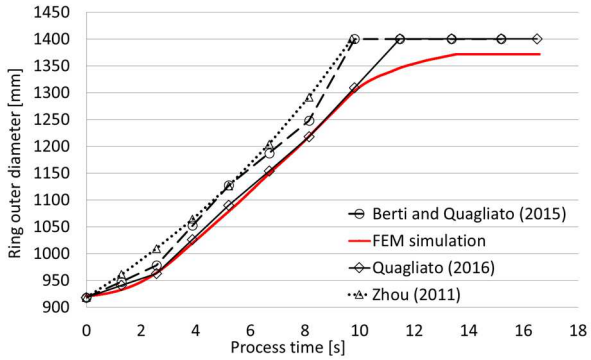

Fig. 64 – Cross-comparison of Quagliato (2016), Berti and Quagliato (2015), Zhou (2011) and FEM simulation for the estimation of the outer diameter of Ring3S.

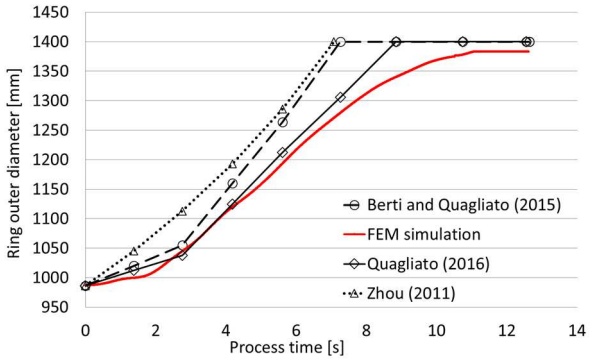

Fig. 65 – Cross-comparison of Quagliato (2016), Berti and Quagliato (2015), Zhou (2011) and FEM simulation for the estimation of the outer diameter of Ring4S.

6.3 Temperature estimation model validation and accuracy

The temperature drop in the ring during the process is an issue largely related to the mass of the ring itself, as well as to its thermal properties and the process time. For this reason, in order to verify the reliability of the developed analytical model, previously presented in section 3.5, 30 study case with rings ranging from 650 mm to 2400 mm, as final outer diameter, have been taken into account. The study cases are those summarized, along with the relevant process parameters, in previous Table 8.

Since the developed model estimates an average temperature for the ring as a consequence of conductive, convective and radiant heat exchange by neglecting eventual heat flow from the core of the ring to its surface, in order to properly compare numerical and analytical results, the average temperature data of inner and outer surface of the ring, in both deformation gaps, have been collected and averaged. The resulting temperature, for each half round of the process, have been compared with the analytical prediction and the percentage error has been calculated in order to prove the accuracy of the prediction.

The local temperature on inner and outer surfaces of the ring, for two chosen slices of the ring, have been recorded by utilizing the above-mentioned particles elements, attached to the inner and the outer surfaces of the ring. The results, in terms of average ring estimation for each round of the process, for the 30 ring study cases, are reported in following Table 17 where the maximum errors are highlighted in red.

Table 17 – Round based temperature prediction (analytical-numerical comparison).

		Round of the process [-]						
Ring Case	**Value**	**1**	**2**	**3**	**4**	**5**	**6**	**7**
1	FE Simulation	1182.9	1159.8	1136.0	1111.1	1084.0	1068.5	
	Analytical	1179.0	1143.5	1119.5	1094.0	1075.5	1065.0	
	% Error	0.33	1.43	1.48	1.56	0.79	0.33	
2	FE Simulation	1184.3	1161.7	1138.4	1114.3	1088.3	1065.9	
	Analytical	1182.0	1143.5	1110.5	1089.0	1072.0	1064.0	
	% Error	0.20	1.59	2.52	2.33	1.52	0.18	
3	FE Simulation	1186.0	1162.2	1137.5	1111.6	1087.7		
	Analytical	1184.0	1152.0	1173.5	1098.0	1079.0		
	% Error	0.17	0.89	-3.06	1.23	0.80		
4	FE Simulation	1179.1	1151.2	1121.7	1107.9	1107.9		
	Analytical	1186.0	1146.0	1115.5	1091.0	1074.5		
	% Error	-0.59	0.46	0.56	1.56	3.12		
5	FE Simulation	1181.0	1154.2	1126.5	1113.7			
	Analytical	1183.5	1148.5	1114.0	1090.5			
	% Error	-0.21	0.49	1.12	2.13			
6	FE Simulation	1183.5	1154.4	1127.1	1127.1			
	Analytical	1181.5	1149.0	1108.5	1086.5			
	% Error	0.17	0.47	1.68	3.74			
7	FE Simulation	1181.4	1153.1	1122.1	1096.3			
	Analytical	1182.0	1141.5	1123.0	1106.0			
	% Error	-0.05	1.02	-0.08	-0.88			

8	FE Simulation	1184.4	1158.9	1131.7	1104.2			
	Analytical	1183.0	1152.5	1130.0	1111.5			
	% Error	0.12	0.56	0.15	-0.66			
9	FE Simulation	1186.2	1157.9	1127.0	1115.0			
	Analytical	1179.5	1146.5	1122.0	1108.0			
	% Error	0.57	1.00	0.45	0.63			
10	FE Simulation	1181.5	1156.5	1130.6	1103.2	1073.2		
	Analytical	1180.5	1140.5	1098.0	1069.5	1051.5		
	% Error	0.09	1.41	2.97	3.15	2.06		
11	FE Simulation	1179.2	1156.0	1131.8	1106.5	1079.1		
	Analytical	1180.0	1142.5	1110.0	1083.5	1066.5		
	% Error	-0.07	1.18	1.97	2.13	1.18		
12	FE Simulation	1185.5	1160.8	1135.2	1112.9			
	Analytical	1185.0	1151.5	1119.0	1097.5			
	% Error	0.04	0.81	1.45	1.40			
13	FE Simulation	1182.2	1154.3	1124.0	1090.3	1059.7		
	Analytical	1182.0	1145.5	1128.0	1110.0	1096.0		
	% Error	0.02	0.77	-0.36	-1.77	-3.31		
14	FE Simulation	1185.1	1160.1	1133.4	1104.4	1071.7	1060.9	
	Analytical	1179.0	1142.5	1120.5	1109.5	1099.5	1094.0	
	% Error	0.52	1.54	1.15	-0.46	-2.53	-3.03	
15	FE Simulation	1186.5	1159.4	1129.8	1097.2	1067.4		
	Analytical	1182.0	1152.5	1128.5	1107.0	1094.5		
	% Error	0.38	0.60	0.12	-0.89	-2.47		
16	FE Simulation	1178.1	1150.1	1129.5	1108.0			
	Analytical	1157.0	1108.5	1092.5	1094.5			
	% Error	1.83	3.75	3.38	1.23			
17	FE Simulation	1179.6	1151.0	1122.5				
	Analytical	1134.0	1098.0	1092.5				
	% Error	4.02	4.83	2.74				
18	FE Simulation	1182.9	1165.8					
	Analytical	1163.5	1117.5					
	% Error	1.67	4.32					
19	FE Simulation	1182.1	1156.2	1128.7	1098.8	1073.7		
	Analytical	1192.0	1157.0	1135.5	1114.5	1104.0		
	% Error	-0.83	-0.07	-0.60	-1.41	-2.74		
20	FE Simulation	1184.0	1158.9	1132.5	1104.3	1072.1		
	Analytical	1188.0	1156.5	1135.0	1114.0	1098.5		
	% Error	-0.34	0.21	-0.22	-0.87	-2.40		
21	FE Simulation	1185.0	1158.0	1140.0	1122.0			
	Analytical	1185.5	1155.5	1131.0	1109.5			
	% Error	-0.04	0.22	0.80	1.13			
22	FE Simulation	1184.4	1157.9	1129.5	1098.7	1063.7	1042.9	
	Analytical	1185.0	1152.5	1129.0	1110.5	1099.0	1089.5	
	% Error	-0.05	0.47	0.05	-1.07	-3.22	-4.28	
23	FE Simulation	1186.9	1163.0	1137.9	1111	1081.1	1063.8	
	Analytical	1185.5	1149.5	1121.0	1101.0	1085.0	1078.0	
	% Error	0.12	1.18	1.50	0.91	-0.36	-1.32	
24	FE Simulation	1189.0	1165.7	1141.1	1114.9	1085.4	1068.3	
	Analytical	1186.0	1153.5	1126.5	1105.5	1096.5	1089.5	
	% Error	0.25	1.06	1.29	0.85	-1.02	-1.95	

25	FE Simulation	1185.5	1160.8	1134.7	1106.6	1075.3	1056.9	
	Analytical	1184.0	1148.0	1122.5	1108.0	1097.5	1090.5	
	% Error	0.12	1.12	1.09	-0.12	-2.02	-3.08	
26	FE Simulation	1186.6	1161.9	1135.8	1107.8	1076.4	1058.1	
	Analytical	1184.5	1157.5	1134.0	1117.5	1103.5	1093.5	
	% Error	0.18	0.38	0.16	-0.87	-2.46	-3.24	
27	FE Simulation	1189.5	1167.3	1144.0	1119.5	1092.2	1076.5	1028.1
	Analytical	1187.5	1164.0	1137.0	1116.5	1102.5	1090.5	1084.0
	% Error	0.17	0.28	0.62	0.27	-0.93	-1.28	-5.15
28	FE Simulation	1185.5	1159.1	1131.1	1100.9	1066.8	1046.7	
	Analytical	1179.0	1146.5	1119.0	1101.0	1088.0	1080.5	
	% Error	0.55	1.10	1.08	-0.01	-1.95	-3.12	
29	FE Simulation	1187.3	1163.8	1138.9	1112.4	1082.9	1065.7	1008.8
	Analytical	1183.0	1151.0	1122.0	1101.5	1091.0	1083.5	1076.5
	% Error	0.37	1.11	1.51	0.99	-0.75	-1.65	-6.29
30	FE Simulation	1189.8	1168.4	1146.0	1122.4	1096.2	1081.1	1027.6
	Analytical	1173.5	1155.0	1131.5	1112.5	1099.0	1092.0	1086.0
	% Error	1.39	1.16	1.28	0.89	-0.25	-0.99	-5.38

Among all the analyzed study cases, the maximum error is calculated in 6.79% whereas the average one in 1.87%, proving the reliability of the developed model in estimating the average temperature of the ring.

In addition to that, since a direct validation of the model was not directly possible, a validation based on the estimation of the process force, on the basis of the flow stress of the material calculated by utilizing the model presented in sections from 3.1 to 3.6, has been carried out. For this first cross-comparison among analytical, numerical and experimental data, the numerical and experimental results available in Kim (2012) have been utilized.

In order to achieve a reliable comparison among the results, the material properties, the size of the ring rolling mill, the process boundary conditions as well as initial and final geometries of the ring have been inputted in the numerical algorithms. The material model equation is that shown in (170) whereas the model constant, for the considered AISI 304 material, are reported in Table 18.

Table 18 – AISI-304 material model constants, Kim (2012).

Temperature [°C]	K_0	a_0	a_1	n	b_0	b_1	m
1100	160.00	0.00	2.14	0.09	0.00	0.10	0.10
1000	225.20	0.00	0.04	0.09	0.17	1.30	0.13
800	330.90	0.00	0.17	0.08	4.50	3.20	0.06

Additionally, the initial and final ring geometries, the dimensions of the tools of the ring rolling mill and the main process boundary conditions are reported in Table 19. In Table 19, the material properties followed by the symbol "*" are derived from Kim (2012) whereas those followed by the symbol "**" are taken from the MATILDA® (Material Information Link and Database Service) archive, available in Simufact.Forming, for the AISI-304 steel.

Table 19 – Model validation case study Kim (2012) data.

Parameters	**Value**
Ring blank outer diameter [mm]	454
Ring blank inner diameter [mm]	150
Ring blank height [mm]	200
Final ring outer diameter [mm]	900
Final ring inner diameter [mm]	722
Final ring height [mm]	110
Radius of the main roll [mm]	423
Radius of the mandrel [mm]	65
Length of the axial rolls [mm]	800
Half of cone vertex angle [°]	20
Main roll rotational speed [rad/s]	2
Mandrel initial feeding speed [mm/s]	5
Mandrel final feeding speed [mm/s]	1
Friction coefficient	0.5
Temperature of the environment [°C]	20
Tool temperature [°C]	150
Ring initial temperature [°C]	1100
*Density [kg/m^3]	7770
**Specific heat capacity [J/kgK]	610
**Emissivity [-]	0.25
**Heat transfer coefficient (conduction) [W/m^{2}K]	20000
**Heat transfer coefficient (convection) [W/m^{2}K]	50

The result of the progressive temperature drop in the ring, as a consequence of conductive, convective and radiant heat exchange is shown in Fig. 66. As previously mentioned, the developed model allows estimating the average temperature of the ring after each deformation gap or, in other words, for each half round of the process.

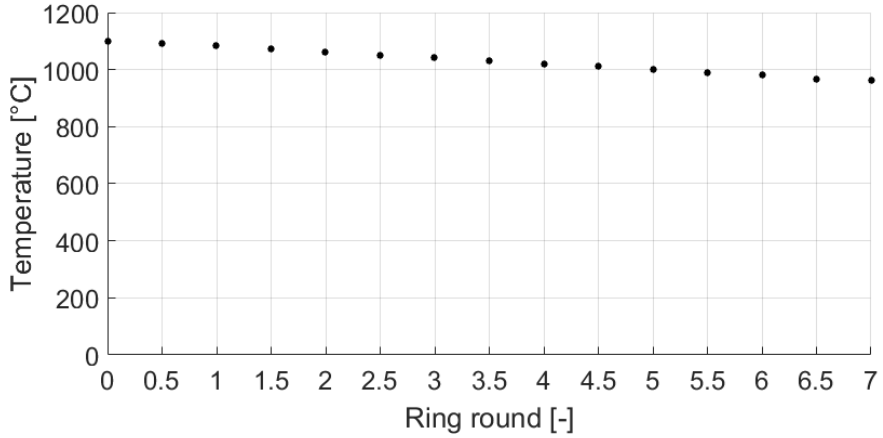

Fig. 66 – Temperature drop prediction for the study case Kim (2012) utilizing the lumped heat transfer model Quagliato (2017).

By utilizing together the information of strain, strain rate and temperature as estimated by utilizing the developed models, shown in previous section 3.3, 3.4 and 3.5, the half round based flow stress of the material has been analytically calculated. In addition to that, based on the von Mises yield criterion, also the yield shear stress is calculated, as shown in Fig. 67. The requirement for the calculation of the yield shear stress of the material is related to the input parameters needed for the estimation of the process force by means of the slip line model proposed in Hill (1950) and utilized by Hawkyard (1973) for the estimation of the radial forming force in cold ring radial rolling process, Eq. (30).

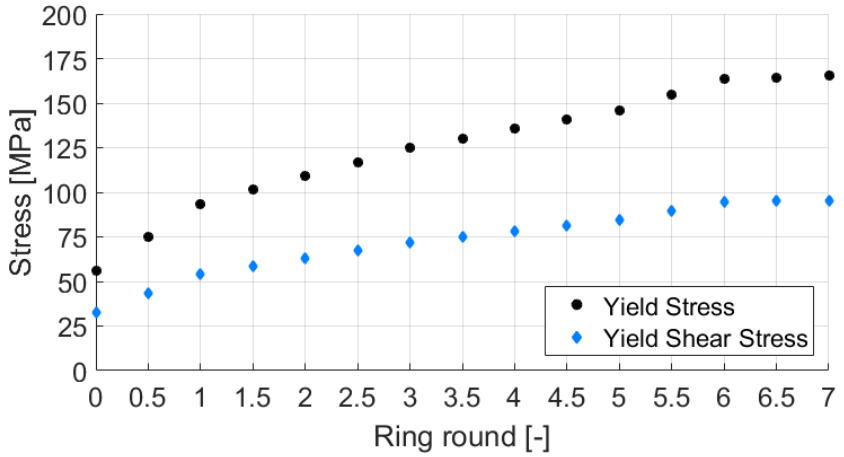

Fig. 67 – Analytical estimation of the yield stress and yield shear stress for the study case of Kim (2012).

The resulting estimation of the radial forming force, in comparison to the experimental and numerical results presented in Kim (2012) is shown in Fig. 68.

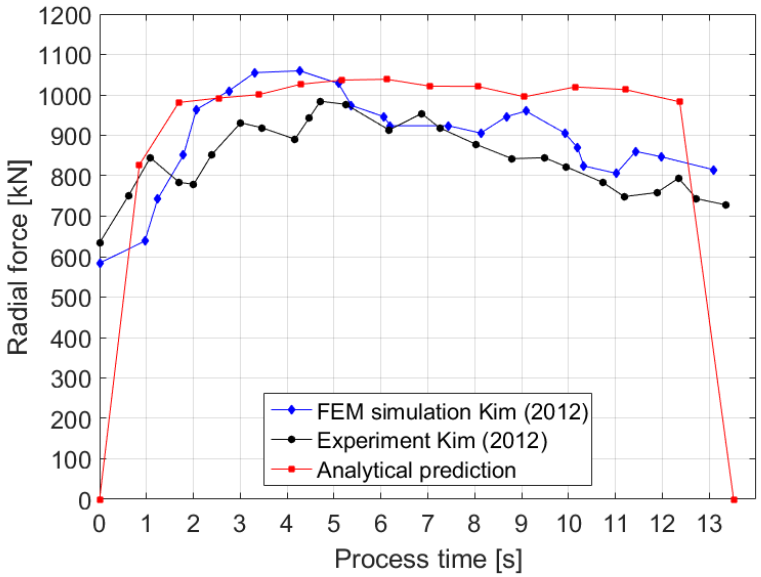

Fig. 68 – Radial forming force results cross-comparison for the Kim (2012) study case.

Concerning the maximum forming force, one of the most important results being that which can influence the choice of the erring rolling machine, the combination of the proposed approach together with the Hawkyard (1973) force model, allows estimating a maximum forming force of 1038.7 Kn whereas the maximum value resulting from the numerical simulation is 1059.6 kN and 984.4 kN from the industrial experiment. Accordingly, the estimation carried out by means of the combination of analytical model proposed in sections from 3.1 to 3.5, together with the literature force model Hawkyard (1973) is equal to 2.0% in comparison to the numerical simulation and to 5.5% in comparison to the relevant industrial experiment, both presented in the work of Kim (2012).

The cross-comparison among analytical, numerical and experimental data allows a first sight of the potentiality of the combined utilization of the proposed approach, especially in terms of computational time. For the calculation of the analytical solution presented in Fig. 68, the total computational time is related only to the setting of the input parameters in the models (implemented in MS Excel) which requires a time lower than 2 hours. However, as shown in previous Table 10, the time required to run a simulation with an adequate mesh is around 16 hours. This time increases if the process parameters setting is done according to a trial-error approach.

In the following section of the thesis, the limitations observed while utilizing the slip line based force model Hawkyard (1973), highlighting the main reason behind the choice of developing a more realistic slip line based force model which considers a better approximation of the contact geometry between tools and ring, as detailed in section 3.7.

6.4 Limitations of the previous slip line based force model

When utilizing the force model proposed by Hawkyard (1973), and based on the slip line field theory developed for a flat punch indenting on a flat surface, one of the key issue is related to the assumption of a flat contact surface between ring and tools. As it will be proved and quantified in this section of the thesis, this assumption is fulfilled if the curvature of ring and rolls are big enough.

By applying the developed combination of analytical models to the study cases reported in previous Table 8, the maximum radial forming force has been calculated by utilizing the force model of Eq. (30), Hawkyard (1973). The accuracy of the prediction of the maximum forming force, for different final outer ring dimensions and for different ratios between the final height and the final thickness of the ring, as shown in following Fig. 69. As previously mentioned, the so-called geometry factor G_f represents the ratio between the final height and the final thickness of the ring and has been utilized in order to analyze possible variation in the accuracy of the algorithms in case of different distributions of the material in the cross-section of the ring.

The R^2 correlation factors for the three interpolation curves have been calculated as 0.955 for the $G_f = 1$ interpolation curve, as 0.916 for the $G_f = 2$ interpolation curve and as 0.973 for the $G_f = 3$ interpolation curve, respectively.

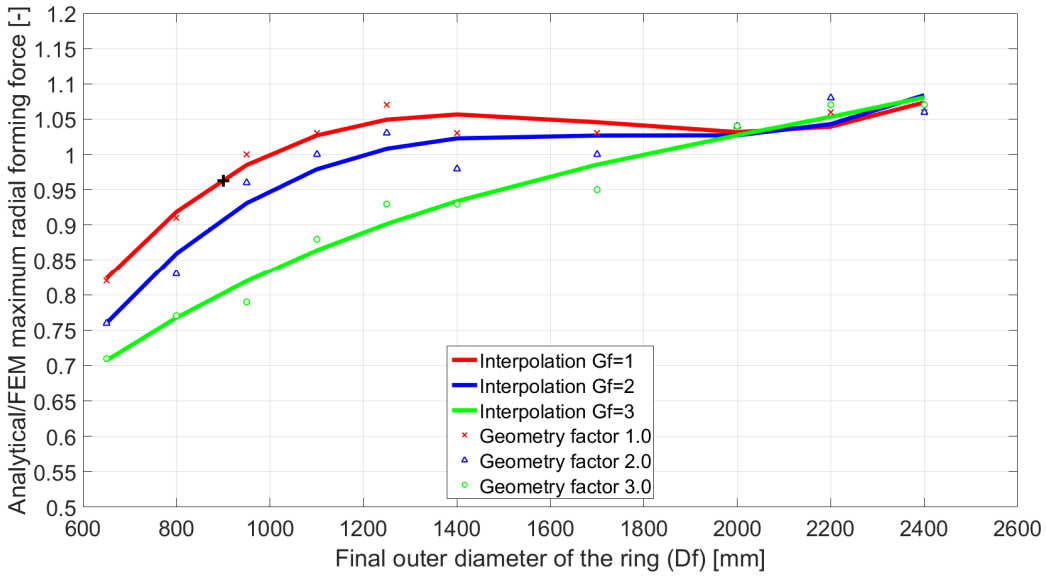

Fig. 69 – Accuracy of the prediction of the maximum radial forming force with the Hawkyard (1973) force model.

The study cases summarized in Fig. 69 have been carried out with the same sizes of the tools of the ring rolling mill in order to avoid any additional influencing factor in the analysis. The ring rolling mill data are those reported in Table 2 with the general process conditions summarized in Table 3. According to this choice, the only influencing parameters are the initial/final dimensions of the ring and the feeding speed of mandrel and upper axial roll.

In addition to that, the accuracy of the prediction of the radial forming force concerning the study case of Kim (2012), presented in the previous section of the thesis, black cross in Fig. 69, perfectly matches the interpolation curve, even if the relevant result has not been utilized for the calculation of the regression curve. This also proves that, even by changing material, process settings and ring rolling mill dimensions, the regression curve is able to predict the accuracy of the estimation of the radial forming force.

Considering the high correlation between ring final geometry, expressed in terms of its final outer diameter, and the accuracy in the prediction of the radial forming force, as shown in Fig. 69, it has been concluded that the assumption of a straight line for the description of the contact between tools and ring, under some specific geometrical conditions, is too rough and leads to lack of precision in the estimation of the radial forming force.

Based on these considerations, the slip line based force model previously detailed in section 3.7 has been developed and the relevant results, in terms of quality of the estimation of the maximum radial and axial forming force, in comparison to both numerical and experimental results, are presented in the following section of the thesis.

6.5 Generalized slip line based force model accuracy

In this last section of chapter 6, two series of results are presented. In the first part, the cross-comparison among analytical, numerical and experimental results concerning the two study cases previously summarized in Table 13, in terms of the evolution of the outer diameter of the ring, radial force and axial force will be presented. In addition to that, the developed generalized slip line based force model (section 3.7) has been applied to nine different study cases and the accuracy in estimating the maximum radial and the maximum axial forming force have been evaluated.

Concerning the two study case where also laboratory experiments have been carried out, the comparison among analytical, numerical and experimental results concerning the evolution of the outer diameter of the ring are presented in Fig. 70 and Fig. 71, respectively. The results comparison in terms of radial and axial forming forces, same for the Ring-Exp-1 and the Ring-Exp-2 study cases, are reported in Fig. 72, Fig. 73, Fig. 74 and Fig. 75, respectively.

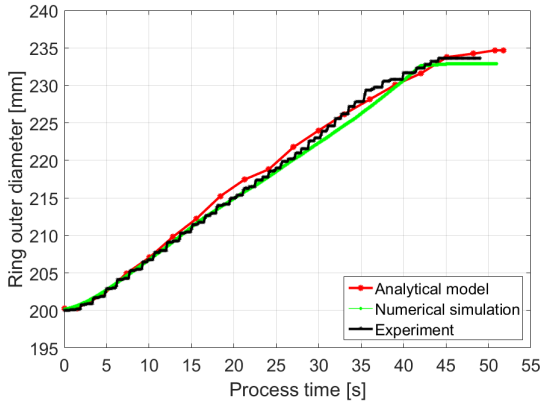

Fig. 70 – Outer diameter evolution for Ring-Exp-1 study case.

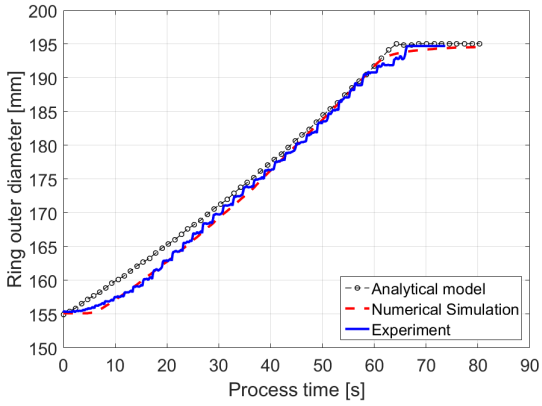

Fig. 71 – Outer diameter evolution for Ring-Exp-2 study case.

In comparison to the relevant experiment, the estimation of the expansion of the outer diameter of the ring is predicted with an error lower than 2%, for both the considered study cases. These positive results prove, once again, that the developed model for the estimation of the geometry evolution of the ring is reliable and capable precise estimations, both in comparison to FEM and experimental results.

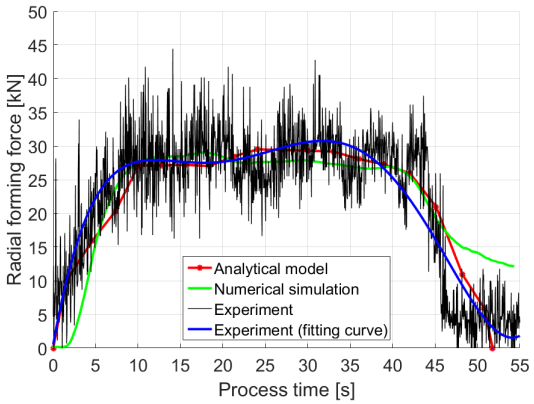

Fig. 72 – Radial force estimation for Ring-Exp-1 study case.

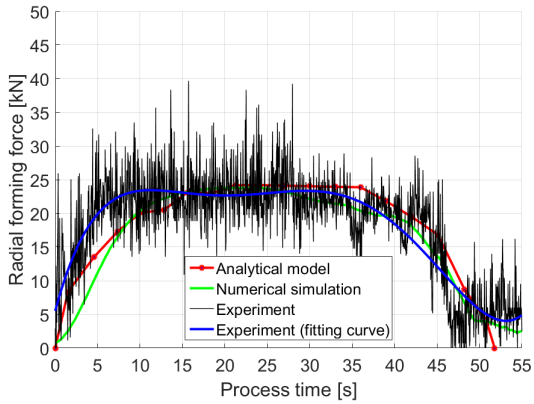

Fig. 73 – Axial force estimation for Ring-Exp-1 study case.

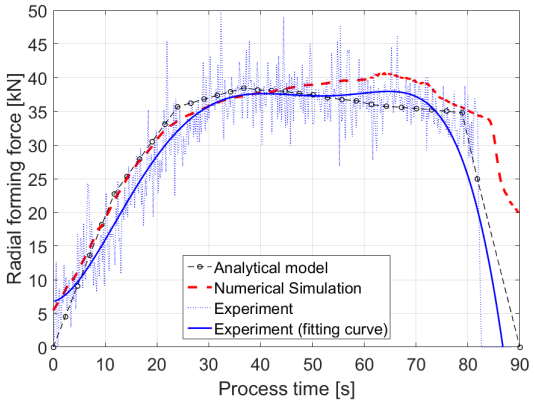

Fig. 74 – Radial force estimation for Ring-Exp-2 study case.

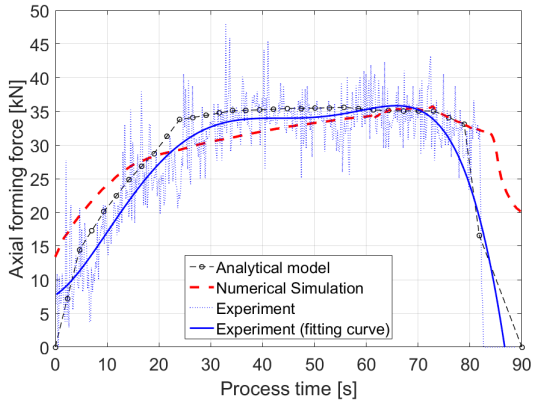

Fig. 75 – Axial force estimation for Ring-Exp-2 study case.

Concerning the estimation of the maximum radial and axial forming forces for the Ring-Exp-1, the deviations of the analytical estimations are estimated in 4.05% and 3.23% whereas that of the numerical simulation in 5.52% and 1.57%, respectively. For Ring-Exp-2, a more detailed analysis has been carried out in order to check the accuracy of the estimations of outer diameter, radial force, and axial force at different times during the rolling process, as shown in Table 20, where the experimental results have been taken as references.

The relatively high deviation of the numerical simulation result, in comparison to the relevant experiment, shown in the beginning of the process for the Ring-Exp-2 (column “Value at 20s”) is mainly caused by the fact that the non-steady expansion of the ring in the first part of the process.

Table 20 – Comparison among analytical, numerical and experimental results at different rolling times for the Ring-Exp-2.

	Value at 20s	**Value at 40s**	**Value at 60s**	**Value at 80s**
Ring outer diameter				
- Experiment	161.37	175.99	188.94	194.72
- Analytical prediction	164.81	177.11	190.64	195.00
- % Error	-2.13	-0.64	-0.90	-0.14
- Numerical simulation	162.17	175.18	189.99	194.52
- % Error	-0.50	0.46	-0.56	0.10
Radial forming force				
- Experiment	28.99	37.62	37.77	33.68
- Analytical prediction	30.51	38.20	36.12	35.37
- % Error	-5.24	-1.54	4.37	-5.02
- Numerical simulation	33.09	37.81	39.61	36.35
- % Error	-14.14	-0.51	-4.87	-7.93
Axial forming force				
- Experiment	27.09	33.95	35.21	31.55
- Analytical prediction	28.75	35.15	35.39	34.08
- % Error	-6.13	-3.53	-0.51	-8.02
- Numerical simulation	27.69	31.73	33.95	35.15
- % Error	-2.21	6.54	3.58	-11.41

When the ring rolling process is started, the ring is put into rotation by the main roll and this initiation of the contact can cause slippage or sudden jamming and releasing of the ring. This issue is also related to higher or lower concentration of lubricant on the surface of the ring. All these issues can be controlled neither in the numerical simulation nor in the analytical model since are all related to unpredictable phenomena. In the same way, at the end of the rolling process, the ring enters the calibration phase, the final stage of the process in which there is not feeding motion of the tools and the dimensions of the ring are homogenized to the final ones. The prediction of the process forces during the calibration phase, as well during the initial phase of the process, is largely influenced by phenomena those are hard to be taken into account in the constitutive equation of an analytical model or even in a detailed numerical simulation.

For all these reasons, the accuracy of the force prediction in the initial and final stages of the process is lower than that in the center of the process, when the ring is steadily expanding. However, although this limitation in the initial and final stages of the process, the developed algorithm is able to predict both radial and axial forming forces with an accuracy ~ 92% in comparison to the relevant experiment, a remarkable results considering that the calculation is carried out almost in the real time, with the exception of the time required for the process data input phase in the MS Excel spreadsheet where the algorithms have been implemented, which averagely takes 2 hours.

In conclusion to this last section of the result chapter 6, the results of the application of the developed generalized slip line based force model for the estimation of the maximum radial and axial forming force for the nine study case summarized in Table 9 are hereafter reported. The main target of this final analysis

is to prove that the developed force model is able to overcome the limitations shown by that proposed by Hawkyard (1973) and that a relatively constant accuracy is obtainable, regardless the dimensions of the ring. The results, in terms of values and relevant parentage error, are reported in following Table 20 whereas in Fig. 76, Fig. 77 and Fig. 78 the final shape of the Ring1F, Ring4F, and Ring7F at the end of the process and the results of the equivalent plastic strain are reported. Once again it is proved that, by setting the numerical simulations by utilizing the set-up parameters as suggested by the algorithm detailed in section 3.2, a uniform expansion and a regular final shape of the ring can be obtained, for relatively small rings (Ring1F, Df = 800 mm), average rings (Ring4F, Df = 1400 mm), and relatively large rings (Ring7F, Df = 2000 mm).

Table 20 – Ring study cases radial and axial forming force analytical vs numerical results comparison.

Case	FEM (radial)	Analytical model (radial)	% Error (radial)	FEM (axial)	Analytical model (axial)	% Error (axial)
Ring1F	1370	1378	0.61	364	376	3.19
Ring 2F	1152	1120	2.78	503	486	3.22
Ring 3F	717	705	1.62	459	461	0.30
Ring 4F	1241	1180	4.92	472	480	1.57
Ring 5F	1201	1183	1.50	637	658	3.35
Ring 6F	852	881	3.40	754	738	2.08
Ring 7F	1300	1350	3.85	643	605	5.88
Ring 8F	1417	1472	3.88	851	863	1.52
Ring 9F	1476	1541	4.40	127	1202	5.36

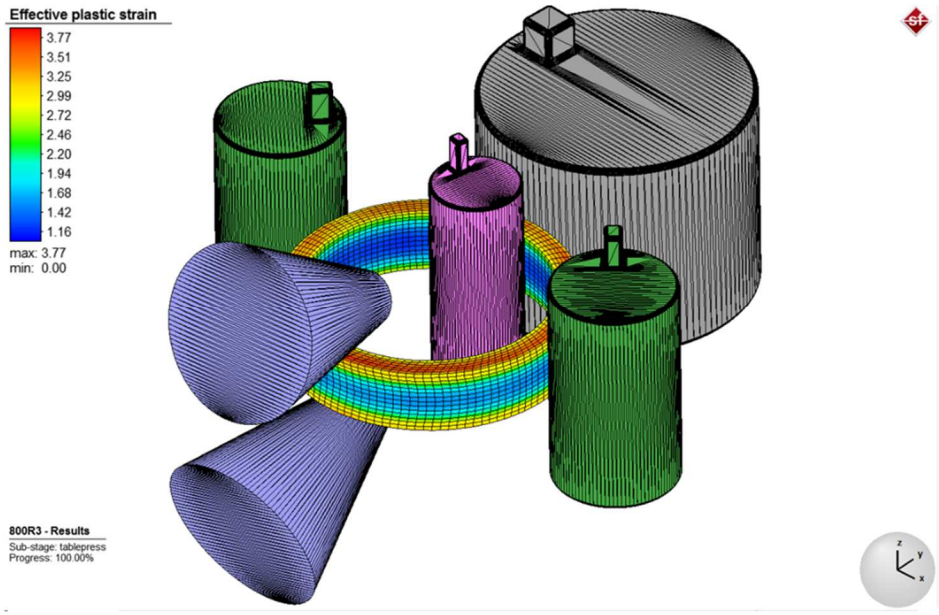

Fig. 76 – Equivalent plastic strain at the end of the rolling time for the Ring1F.

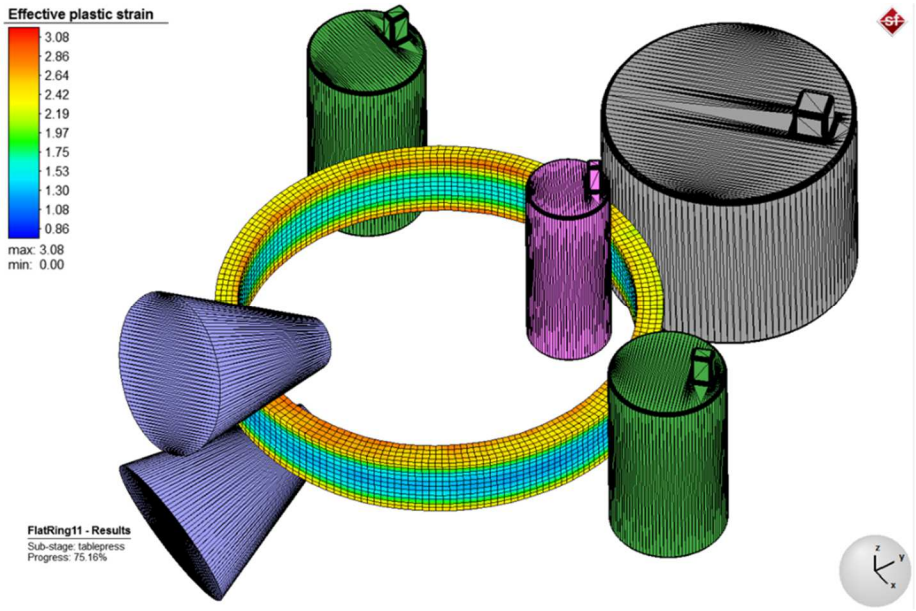

Fig. 77 – Equivalent plastic strain at the end of the rolling time for the Ring1F.

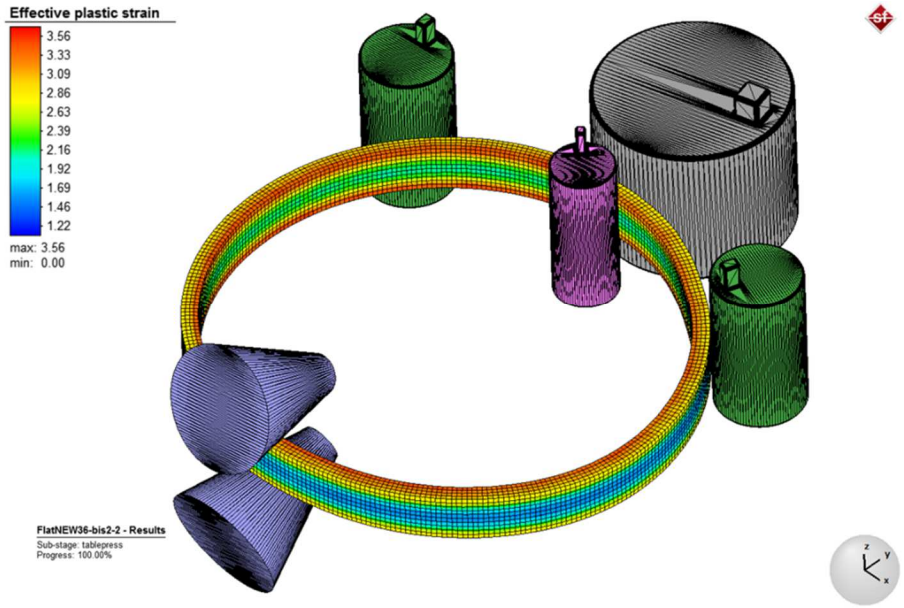

Fig. 78 – Equivalent plastic strain at the end of the rolling time for the Ring1F.

The huge results summary presented in this last section of the paper aimed to give an overview on the potentiality of the developed algorithms and, especially, how the possible estimation are reliable, both in comparison to numerical simulations and experiments.

In the developed algorithms, average accuracy of the estimation, always higher than 90%, make them to be reliable for an initial vast case-studies analysis, finalized to the identification of the few best combinations of process parameters those allow a successful ring rolling process and is not aimed to the complete avoiding of the numerical simulation, indeed.

Chapter 7: Conclusions

The radial-axial ring rolling process has been a manufacturing technic largely used in all the industry for more than 150 years but, spite of its long history, a deep and clear understanding of the strong dependence between process setting and output variables is still not well spread, especially in the industrial compartment.

The main purpose of the research work contained in the present thesis has, and still is, the development of algorithm which can help process planners and engineers in the early stages of the design stage, when the utilization of numerical simulation is not convenient, especially because of the time required for both their setting and for the computation of the results. For this reason, the collection of algorithms presented in the thesis, initially implemented in MS Excel and Matlab, is being included a Fortran-based program which shall have a GUI of easy utilization, making the developed research work to be utilizable by a large variety of researchers and employees dealing with the radial-axial ring rolling process.

The good agreement proved by the comparison with numerical simulation and, where possible, with the experimental results, both from the literature and carried out on soft-alloy rings, shown the reliability of both the single models themselves as well as of their combined utilization. The importance of a complete and bottom-to-top analytical algorithms frame is of key importance, especially in terms of the different results which can be derived from their utilization. For instance, the simple knowledge of the process forces is not consistent since also the kinematic of the process, especially in terms of geometrical expansion of the ring, is of key importance for a successful manufacturing of the ring.

To this aim, the developed combination of algorithms covers all the most important aspects of the ring rolling process, from the process set-up to the estimation of the forming forces, allowing a real-time evaluation of the impact of the design choices, both in terms of process parameters and ring sizes, on important output variables. The “real-time” calculation is, evidently, the main advantage of the proposed approach, in comparison to numerical simulations. Although well-set numerical simulation is able to

replicate quite accurately the real kinematic and dynamic of the process, the computational time is one of its main drawbacks. The proposed approach aims to fill the gap between the start of the design phase and the setting of the numerical simulation, acting as a sort of FEM pre-processor whose aim is twofold. In first instance, the process engineer ought to analyze the influence of the process parameters on the main output variables and identifies the few combination those show to be able to grant a successful manufacturing of the ring, fulfilling the process boundary condition, i.e. the maximum forming force of the available ring rolling mill. At this point, by adopting the process settings defined by utilizing the proposed algorithm, the numerical simulation can be set-up only on the few chosen cases those have given good results from the initial analysis. The second stage allows obtaining, of course, a more detailed and deep analysis but it will be carried out on a smaller amount of combinations of process parameters, allowing to speed-up the whole design phase.

To better highlight improvement in the time required for the design of the ring rolling process by utilizing the proposed approach, a generic study case has been selected and two different approaches have been followed for its set-up. In the first case, the design of the process has been carried out only by means of numerical simulations, without any initial study-phase with the proposed collection of algorithms. In the second case, the proposed algorithms have been utilized for the definition of the best 3-combinations of process parameters, subsequently tested by means of numerical simulation. In the first case-scenario, in order to obtain a stable process with a good expansion of the ring, 16 FEM have been necessary, with a total setting and computational time of 112 hours. In the second case-scenario, the initial study phase carried out by utilizing the proposed algorithms took approximately 8 hours and, after it, only 4 FEM simulation have been set-up on the four combinations of process parameters identified in the first phase, for a total design time of 36 hours. It is immediately clear that the indication given by the utilization of a more rigorous design approach, based on the mechanics at the base of the process, allows sparing time and to focus the analysis only on the promising combinations of process parameters, avoiding to invest computational time on inappropriate sets of parameters.

Chapter 8: Future work

In the present thesis, several analytical models concerning the radial-axial ring rolling process of flat rings have been presented and validated by comparison them with both numerical and experimental results as well proving their higher accuracy in comparison to previous literature ones, where they were available.

As concerns future work related to this research topic, one of the most important aspect is probably the extension of part of the developed algorithms to the profiled ring rolling process, where the ring cross-section is not flat anymore but it presents different shapes, from the most common L-shape, C-shape and U-shape to more complex ones. The work towards this research direction has been already started at the moment this thesis is being drafted and will proceed in the future in order to develop a similar collection of algorithms, able to allow a full understanding of the profiled ring rolling process. Especially, in the profiled ring rolling process, the evolution of the ring geometry is not straightforward as in the flat ring rolling since the flange expansion is not directly controlled by two opposite tools but it is normally free to expand. This fact makes the set-up of the profiled ring rolling process a more complex task, in comparison to that of flat rings, thus an algorithm able to propose a certain set of initial ring preform and process parameters necessary to reach the final desired shape while foreseeing the geometrical expansion of both wall and flange during the process, would be of very interest for the industry.

An issue which is common for both flat and profiled rings is related to the estimation of the mechanical properties of the ring after the production, in terms of estimation of the ring microstructure. In the literature, different models correlating the strain and temperature fields to the microstructure have been already developed an validated but, to this aim, a more local temperature model should be developed in order to predict not only the average temperature of the ring but the temperature distribution throughout the thickness. As also previously stated in section 3.5 of the thesis, the utilization of a more complex formulation for the estimation of the temperature gradient in the ring cross-section is feasible but the

complexity of the calculation as well as the non-close-form of the relevant equations shall result in a more complex algorithm thus is longer computational time.

Finally, both concerning the developed model for the flat ring rolling process as well for the on-going algorithms development related to profiled rings, the aim is to include them into Fortran-based programs in order to favorite their utilization, especially in the industrial environment.

Reference

1) J.M. Alexander. A slip line field for the hot rolling process. Proc. Inst. Mech. Eng. 169 (1955) 1021-1030.
2) J. Alexis, X. Satheesh. An analysis on the parameter optimization in Ring rolling process. Kovarenstvi (A Czech Republic International Journal), Vol. 24, 2004, pp 11-17.
3) M.M. Al-Mohaileb. Computer modeling of the temperature profile during the ring rolling process. Ph.D. Dissertation, The Ohio State University, June 2000.
4) N. Anjami, A. Basti. Investigation of rolls size effects on hot ring rolling process by coupled thermo-mechanical 3D-FEA. J. Mat. Proc. Tech. 210 (2010), 1364-1377.
5) G.A. Berti, L. Quagliato, M. Monti. Set-up of radial–axial ring-rolling process: Process worksheet and ring geometry expansion prediction. Int. J. Mech. Sc. 99 (2015), 58-71.
6) I.F. Collins. Slipline field solution for compression and rolling with suppling friction. Int. J. Mech. Sc. 11 (1969), 971-978.
7) K. Davey, M.J. Ward. An ALE approach for finite element ring-rolling simulation of profiled rings. J. Mat. Proc. Tech. 139 (2003), 559-566.
8) P. Dewhurst, I.F. Collins, W. Johnson. A class of slipline field solutions for the hot rolling of strips. J. Mech. Eng. Sc. 15:6 (1973), 439-447.
9) M.R. Forouzan, M. Salimi, M.S. Gadala, A.A. Aljawi. Guide roll simulation in FE analysis of ring rolling. J. Mat. Proc. Tech. 142 (2003), 213-223.
10) L. Giorleo, E. Ceretti, C. Giardini. Energy consumption reduction in ring rolling processes: a FEM analysis. Int. J. Mech. Sc. 74 (2013), 55-64.
11) X. Gong, F. Yan. Research on PEEQ for conical ring with outer steps ring rolling. Phys. Proc. 25 (2012), 257-261.
12) L.G. Guo, H. Yang. Effect of sizes of forming rolls on cold ring rolling by 3D-FE numerical simulation. Trans. Nonfer. Met. Soc. China 16 (2006), s645-s651.
13) L. Guo, H. Yang. Towards a steady forming condition for radial–axial ring rolling. Int. J. Mech. Sc. 53 (2011), 286-299.
14) J.B. Hawkyard, J. Johnson, J. Kirkland, E. Appleton. Analysis of roll force and torque in ring rolling, with some supporting experiments. Int. J. Mech. Sc. 15 (1973), 873-893.
15) A. Hensel, T. Spittel, Kraft - und Arbeitsbedarf bildsamer Formgebungsverfahren, 1st edition, Deutscher Verlag für Grundstoffindustrie (1978), Leipzig.
16) R. Hill: The Mathematical Theory of Plasticity. Clarendon Press. 1950, Chapter VI and VII.

17) A. Kalyani, A. Mattikalli, A. Deshmukh. The effect of force parameter on profiled ring rolling process. Int. J. Eng. Res. & Tech. 4:5 (2015), 840-844.
18) C.R. Keeton: Ring rolling, in: ASM Metals handbook: forming and forging. Metals Park, OH: ASM International. 1988, pp 108-127.
19) T.D. Kil, J.M. Lee, Y.H. Moon. Formability estimation of ring rolling process by using deformation processing map. Proc. Eng. 81 (2014), 298-303.
20) T.D. Kil, J.M. Lee, Y.H. Moon. Quantitative formability estimation of ring rolling process by using deformation processing map. J. Mat. Proc. Tech. 220 (2015), 224-230.
21) N. Kim, H. Kim, K. Jin. Optimal design to reduce the maximum load in ring rolling process. Int. J. Prec. Eng. and Manuf. 13:10 (2012), 1821-1828.
22) K.H. Kim, H.G. Suk, M.Y. Huh. Development of the profile ring rolling process for large slewing rings of alloy steels. J. Mat. Proc. Tech. 187-188 (2007), 730-733.
23) B.S. Kim, H.K. Moon, E.Z. Kim, M.H. Choi, M.S. Joun. A dual-mesh approach to ring-rolling simulations with emphasis on remeshing. J. Manuf. Proc. 15 (2013), 635-643.
24) H. Lin, Z.Z. Zhi. The extremum parameters in ring rolling. J. Mat. Proc. Tech. 69 (1997), 273-276.
25) A.G. Mamalis, W. Johnson, J.B. Hawkyard. Pressure distribution, roll force and torque in cold ring rolling. J. Mech. Eng. Sc. 18:4 (1976), 196-209.
26) P. Opela, I. Schndler, P. Kawulok, F. Vancura, R. Kawulok, S. Rusz, T. Petrek. Hot flow stress models of the steel C45. Metalurgija 54 (2015), 469-472.
27) A. Parvizi, K. Abrinia, M. Salimi. SLAB analysis of ring rolling assuming constant shear friction. J. Mat. Eng. and Perf. 20:9 (2010), 1505-1511.
28) A. Parvizi, K. Abrinia. A two dimensional upper bound analysis of the ring rolling process with experimental and FEM verifications. Int. J. Mech. Sc. 79 (2014), 176-181.
29) D.S. Qian, G. Zhou, L. Hua, D.F. Shi, H.X. Li. 3D coupled thermomechanical FE analysis of blank size effects on radial-axial ring rolling. Ironmaking and Steelmaking 40:5 (2013), 360-368.
30) D.S. Qian, L. Hua, L.B. Pan. Research on gripping conditions in profile ring rolling of raceway groove. J. Mat. Proc. Tech. 209 (2009), 2794-2802.
31) D. Qian, Y. Pan. 3D coupled macro–micro finite element modelling and simulation for combined blank-forging and rolling process of alloy steel large ring. Comp. Mat. Sc. 70 (2013), 24-36.
32) L. Quagliato, G.A. Berti. The mathematical definition of the 3D strain field of the ring in the radial-axial ring rolling process. Int. J. Mech. Sc. 115-116 (2016), 746-759.
33) L. Quagliato, G.A. Berti. Temperature estimation and slip-line force analytical models for the estimation of the radial forming force in the RARR process of flat rings. Int. J. Mech. Sc. 123 (2017), 311-323.

34) J.S. Ryoo, D.Y. Yang. The influence of process parameters on torque and load in ring rolling. J. Mech. Work Tech. 12 (1986), 307-321.

35) J.L. Song, A.L. Dowson, M.H. Jacobs, J. Brooks, I. Beden. Coupled thermo-mechanical finite-element analysis of hot ring rolling process. J. Mat. Proc. Tech. 121 (2002), 332-340.

36) Z.C. Sun, H. Yang, X.Z. Ou. Thermo-mechanical coupled analysis of hot ring rolling process. Trans. Nonfer. Met. Soc. China 18 (2008), 1216-1222.

37) H. Utsunomiya, Y. Saito, T. Shinoda, I. Takasu. Elastic-plastic finite element analysis of cold ring rolling process. J. Mat. Proc. Tech. 125-126 (2003), 613-618.

38) M. Wang, H. Yang, Z.C. Sun, L.G. Guo, X.Z. Ou. Dynamic explicit FE modelling for hot ring rolling. Trans. Nonfer. Met. Soc. China 16 (2006), 1274-1280.

39) T. Wang, Q. Wang. Calculation of axial rolling force in radial-axial ring rolling process. Adv. Mat. Res. 1004-1005 (2014), 1344-1347.

40) Z.W. Wang, J.P. Fan, D.P. Hu, C.Y. Tang, C.P. Tsui. Complete modeling and parameter optimization for virtual ring rolling. Int. J. Mech. Sc. 52 (2010), 1325-1333.

41) Z.W. Wang, S.Q. Zeng, X.H. Yang, C. Cheng. The key technology and realization of virtual ring rolling. J. Mat. Proc. Tech. 182 (2007), 374-381.

42) F.L. Yan, L. Hua, Y.Q. Wu. Planning the feed speed in cold ring rolling. Int. J. Mach. Tools & Manuf. 47 (2007), 1695-1701.

43) Y. Yea, Y. Ko, N. Kim, J. Lee. Prediction of spread, pressure distribution and roll force in ring rolling process using rigid–plastic finite element method. J. Mat. Proc. Tech. 140 (2003), 478-486.

44) D.Y. Yang, J.S. Ryoo. An investigation into the relationship between torque and load in ring rolling. Trans. of ASME 109 (1987), 190-196.

45) H. Yang, M. Wang, L.G. Guo, Z.C. Sun. 3D coupled thermo-mechanical FE modeling of blank size effects on the uniformity of strain and temperature distributions during hot rolling of titanium alloy large rings. Comp. Mat. Sc. 44 (2008), 611-621.

46) G. Zhou, D.S. Qian. 3D coupled thermo-mechanical FE analysis of roll size effects on the radial–axial ring rolling process. Comp. Mat. Sc. 50 (2011), 911-924.

47) G. Zhou, L. Hua, J. Lan, D.S. Qian. FE analysis of coupled thermo-mechanical behaviors in radial–axial rolling of alloy steel large ring. Comp. Mat. Sc. 50 (2010), 65-76.

48) G. Zhou, L. Hua, D. Qian, D. Shi, H. Li. Effect of axial rolls motions on radial-axial rolling process for large-scale alloy steel ring with 3D coupled thermos-mechanical FEA. Int. J. Mech. Sc. 59 (2012), 1-7.